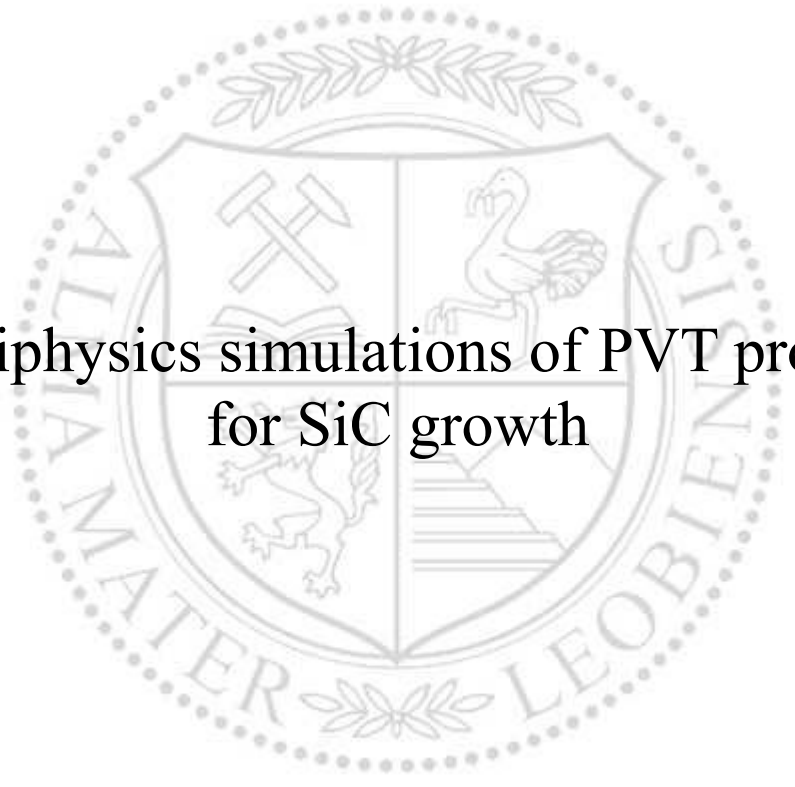Chair of Physical Metallurgy

Master's Thesis

Multiphysics simulations of PVT process for SiC growth

Carlos Moya Merino

February 2024

AFFIDAVIT

I declare on oath that I wrote this thesis independently, did not use any sources and aids other than those specified, have fully and truthfully reported the use of generative methods and models of artificial intelligence, and did not otherwise use any other unauthorized aids.

I declare that I have read, understood and complied with the "Good Scientific Practice" of the Montanuniversität Leoben.

Furthermore, I declare that the electronic and printed versions of the submitted thesis are identical in form and content.

Date 28.02.2024

_____
Signature Author
Carlos Moya Merino

Acknowledgements

First of all, I would like to thank the AMASE program. They gave me the opportunity to study in two universities abroad. I learnt a lot during this period and met incredible people. Surely this experience will have a big impact on my coming future.

I am also very grateful to Lorenz Romaner, who took me as student worker in the Computational Material Science group at the Montanuniversität Leoben since the very beginning. This allowed me to see from the inside how a research group works and also made me feel very comfortable during this time. He also introduced me into the computational material science field, which was a completely unknown topic for me and nowadays is something I am very interested in.

Next, I would like to thank Zaher Ramadan, postdoc at the Computational Material Science group, who help with all the doubts arisen during the realization of this master thesis. Moreover, he has helped me to make learning simulation with the finite element method much easier.

And most importantly, my family and my friends, both the ones I had and the ones I met during this period. Without them and their support I will probably not be here today.

Abstract

In the recent years, silicon carbide (SiC) has emerged as a main material in the semiconductor industry thanks to its outstanding properties. The production method of single-crystalline SiC boules is known as Physical Vapor Transport (PVT), nonetheless, the setup configuration does not allow to inspect the key physical parameters such as temperature and gas partial pressures in-situ. Therefore, computational simulations have become the main approach to control and predict the PVT parameters, especially using the Finite Element Method (FEM). The construction of a high-fidelity FEM model for the description of the growth process could be complex due to the physics involved.

This master thesis deals with the validation of different algorithms to account for heat transfer by radiation physics. COMSOL Multiphysics is a FEM software which has different algorithms (direct area integration, hemicube and ray shooting) to describe surface-to-surface radiation. These algorithms are tested and validated to determine their accuracy in a variety of different model geometries including also PVT furnace models, which could be the basis for more complex models.

Kurzfassung

In den letzten Jahren hat sich Siliziumkarbid (SiC) dank seiner hervorragenden Eigenschaften zu einem der wichtigsten Materialien in der Halbleiterindustrie entwickelt. Die Produktionsmethode ist als physikalischer Gasphasentransport (PVT) bekannt, doch die Aufbaukonfiguration erlaubt es nicht, Informationen in-situ zu erhalten. Daher wurden Computersimulationen zum wichtigsten Ansatz für die Kontrolle und Vorhersage der PVT-Parameter, insbesondere durch die Modellierung mit der Finite Elemente Methode (FEM). Die Konstruktion eines FEM-Modells für die Modellierung eines Wachstumsprozesses kann jedoch aufgrund der beteiligten Physik sehr komplex sein.

Diese Masterarbeit beschäftigt sich mit der Validierung verschiedener Algorithmen zur Berücksichtigung der Wärmeübertragung durch Strahlungsphysik. COMSOL Multiphysics ist eine FEM-Software, die über verschiedene Algorithmen (direkte Flächenintegration, Hemicube und Ray Shooting) zur Beschreibung der Strahlung von Oberfläche zu Oberfläche verfügt. Diese Algorithmen werden getestet und validiert, um ihre Genauigkeit in verschiedenen Modellgeometrien, inklusive solchen von PVT Reaktoren, zu bestimmen, was die Grundlage für komplexere Modelle sein könnte.

Contents

1 Introduction

Modern electronics is the base of developed societies, making it an ever-present field of research and engineering. The constant ambition to improve efficiency, reliability and performance has led to the search for new and better materials and production methods. So far, silicon (Si) has been the mainstay of electronic devices, but SiC is emerging as a leading candidate to replace thank to its amazing properties.

The main method of producing SiC wafers is the Physical Vapor Transport (PVT) method. This growth process is conducted at high temperatures and vacuum, therefore the parameters must be well controlled to secure proper growth conditions. Unfortunately, the process is performed in a quasi-closed crucible, which makes it impossible to predict these parameters without perturbation. To overcome this drawback, reactor modelling and simulation has arisen as the best option. In this case, the Finite Element Method (FEM) has been selected for modelling. For a suitable prediction, a realistic model must be constructed considering all the physics involved in the process such as heat transfer, induction heating, mass transport or sublimation, among others.

The aim of this thesis is to establish a basis for a more realistic PVT growth process model in the future. The used FEM software is COMSOL Multiphysics and the main idea is to determine which model or algorithm is the most accurate to represent surface-to-surface radiation physics. This is tested in a simple model just considering inductive heating and heat transfer by conduction and radiation.

Initially, simple geometries (toy models) are tested to check the impact of some parameters in the radiation models: mesh density, shadowing effect or tolerance. Furthermore, they are used in a simple version of the PVT geometry and in an actual PVT reactor geometry. In this case, the effect of geometry complexity is analysed. Moreover, it is determined which radiation model is more accurate by comparing them with experimental data, obtained from real PVT reactor thermal test. Finally, the importance of the induction coil for the heating process is investigated.

2 Theoretical background

2.1 Silicon carbide

Silicon carbide (SiC) is a potential replacement for Si substrates for electronic devices focused on high frequency, high power and high temperature applications due to its properties, in particular its wide bandgap [1].

SiC is a solid compound whose structure contains equal stoichiometric parts of Si and C. Each atom is surrounded by four atoms of the opposite element forming a tetrahedral configuration, as shown in *Figure 1*.
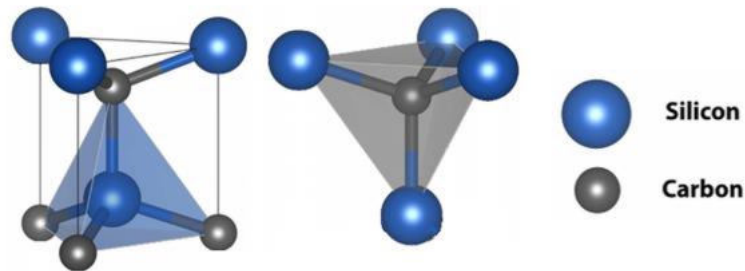

Figure 1. Tetrahedral building block of SiC [2].

This compound presents a special case of polymorphism called polytypism. While polymorphism establishes the existence of more than one crystal structure for the same compound, polytypism describes the existence of multiple stacking sequences for the same compound preserving the 2D translations within the layers [3].

More than 250 polytypes have been identified so far. Nevertheless, the most suitable ones for technological applications are 3C-SiC, 4H-SiC and 6H-SiC. They have ABC, ABAC and ABCACB stacking sequences, respectively. The different crystal structures are depicted in *Figure 2*.

SiC possesses favourable physical properties that it has an advantage over other semiconductors to operate at high temperatures, high voltages and high frequencies. *Table 1* reflects a comparison between the physical properties of Si and the mentioned three SiC polytypes. *a* and *c* correspond

to lattice parameters, E_g, n_i, ε_r, μ_n, E_c, v_{sat} and k represent the energy bandgap, intrinsic carrier concentration, relative permittivity, carrier mobility, electric breakdown field, saturated electron drift velocity and thermal conductivity, respectively.
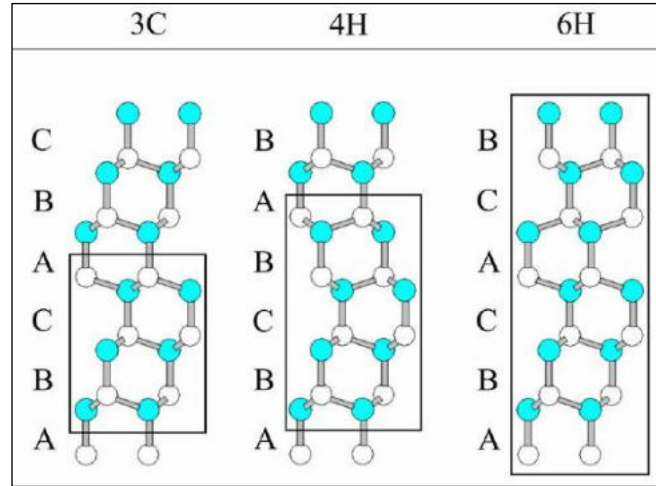

Figure 2. Stacking sequences of 3C-SiC, 4H-SiC and 6H-SiC [4].

Table 1. Physical properties of Si and the three major SiC polytypes at room temperature [5].

Polytype	a (Å)	c (Å)	E_g (eV)	n_i (cm^{-3})	ε_r	μ_n (cm^{-2}/V·s)	E_c (MV/cm)	V_{sat} (10^7 cm/s)	k (W/cm·K)
Si	5.4310	5.4310	1.1	$1.5 \cdot 10^{10}$	11.8	1350	0.3	1.0	1.5
3C-SiC	4.3596	4.3596	2.30	6.9	9.6	900	1.2	2.0	4.5
4H-SiC	3.0730	10.053	3.26	$8.2 \cdot 10^{-9}$	10.0	720^a/650^c	2.0	2.0	4.5
6H-SiC	3.0730	15.11	3.00	$2.3 \cdot 10^{-6}$	9.7	370^a/50^c	2.4	2.0	4.5

Its bandgap is in the range of 2.3-3 eV, being a wide bandgap semiconductor (WBG). It offers higher electrical breakdown field, larger saturated electron drift velocity and higher thermal conductivity compared to Si. These properties translate into high thermal stability, lower power losses and more efficient heat dissipation. In addition, some properties are anisotropic such as the carrier mobility. One reason of these outstanding properties is its smaller lattice parameter, which causes a large electronic bandgap E_g and higher breakdown field E_c. The large bandgap and the small lattice parameter give rise to a high effective electron mass in the reciprocal space, which leads to a smaller electron mobility μ_n. Nonetheless, combining the great breakdown field and the high saturated electron drift velocity v_{sat}, enables operation at higher frequency compared to Si [6].

2.2 Physical vapor transport process

The difficulty to produce SiC has been the main barrier for replacing Si in electronic applications. According to *Figure 3*, the liquid SiC theoretically exists up to 2830 °C at 10^5 bar. Those are challenging conditions for an engineering process. In addition, the stabilization of the desired polytype during the process is extremely troublesome, since the formation enthalpies of the different polytypes are in a very narrow range. Therefore, conventional methods which are based on solidification from melt, such as Czochralski method, cannot be used to produce highly pure bulk SiC [7].
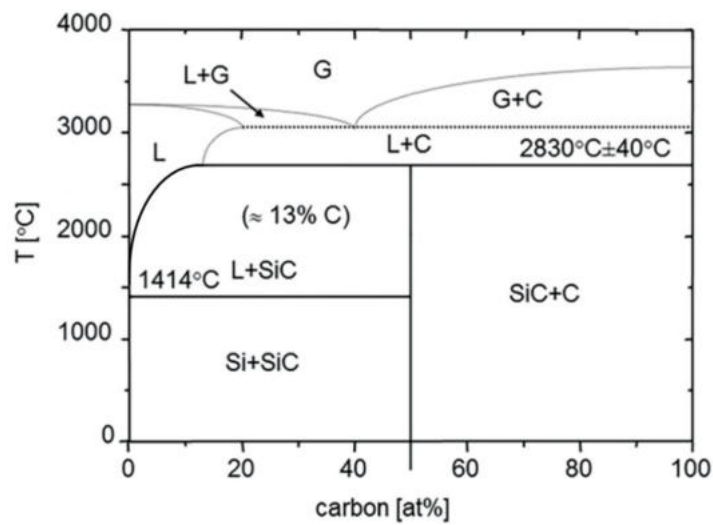
Figure 3. Phase diagram of the Si-C system [7].

Alternatives for producing bulk SiC are the so-called vapor phase route techniques. One of those techniques is known as Physical Vapor Transport (PVT). The method is based on the SiC sublimation at 2200-2400 °C at low pressures. A source powder of SiC is placed in a crucible while a SiC seed is at the top of the crucible as shown in *Figure 4*, this crucible is normally made of graphite due to the high temperature conditions.

The crucible is inductively heated up by means of a surrounding coil until the powder source sublimates. The resulting vapor flows upwards, depositing the Si and C onto the seed crystal. This is such a complex process whereby many parameters must be controlled, although the driving force of the growth process is the temperature gradient between the hot source powder and the colder seed crystal [8].
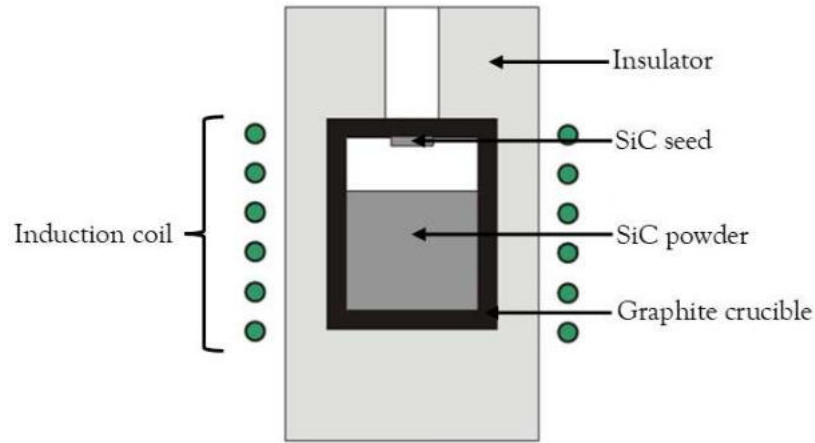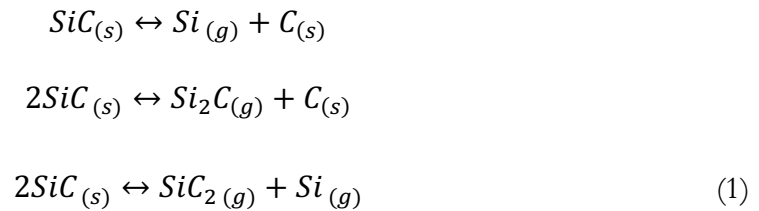
Figure 4. PVT setup [6].

The generated vapor contains predominantly species Si, SiC_2 and Si_2C. Some proposed sublimation reactions are [6]:

$$SiC_{(s)} \leftrightarrow Si_{(g)} + C_{(s)}$$

$$2SiC_{(s)} \leftrightarrow Si_2C_{(g)} + C_{(s)}$$

$$2SiC_{(s)} \leftrightarrow SiC_{2(g)} + Si_{(g)} \tag{1}$$

Sublimation and condensation are highly dependent on the thermal gradient $\Delta T = T_{source} - T_{seed}$. Growth rate is strongly influenced by T_{seed}, as this temperature decreases, the growth rate increases due to higher undercooling at the seed surface. Nevertheless, this increases the thermal gradient (normal values are 10-25 ºC/cm) triggering higher defect densities.

Large number of structural defects is another issue for SiC crystals. Micropipes are relevant defects during SiC growth. It consists of a screw dislocation with large Burgers vector which propagates through the bulk during the growth process. These defects are the major barriers in the production of high-performance SiC devices [9].

Therefore, many parameters must be controlled to predict and perform an efficient and feasible growth process. The PVT setup contains a quasi-closed graphite crucible, meaning there is no possibility to get information of the system without perturbating it. Consequently, experiments themselves are not enough to achieve a suitable process and high-quality SiC crystals. An alternative, which has been gaining great importance in the last years in material engineering, are the numerical modelling in order to predict thermal profiles and physico-chemical parameter.

In this thesis, an oversimplified PVT growth process is considered. In these assumptions, the SiC source is treated as a whole solid instead of a powder. Moreover, there is no mass transport or chemical reactions. Therefore, the crucible is only heated up inductively.

2.3 Finite element method

PVT is governed by various parameters and phenomena such as heat transfer or mass transport, translating the process into a system of partial differential equations (PDEs) in a continuous domain. These PDEs cannot be solved analytically in most cases. One approach to get true continuum solutions is numerical modelling, which encompasses methods like Finite Volume Method (FVM), Finite Difference Method (FDM) or Finite Element Method (FEM), all of them based on discretization.

FEM consists in dividing the continuous system domain into smaller finite subdomains, creating local approximations of the solution. Finally, these local approximations are combined to generate a global solution for the whole system. The discretization is performed by creating a mesh of elements covering the whole system [10]. These elements can have various forms depending on our system. All possibilities are shown in *Figure 5*.
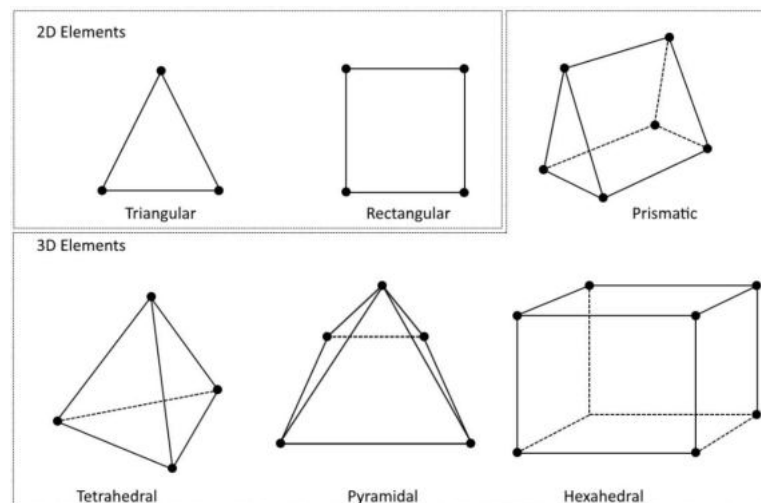

Figure 5. Different type of mesh elements in FEM [11].

The local approximations are entrenched at node positions. Mesh nodes are normally positioned at the vertex of the mesh elements, depicted as black dots in *Figure 5*. As an example, a function u can be the dependent variable of a PDE. This u function can be approximated by a function u_h by means of linear combination according to *Eq.(2)*, where u_i are function coefficients and Ψ_i are the basis functions which depend on node position [11]:

$$u_h = \sum_i u_i \Psi_i \qquad (2)$$

2.4 Heat transfer mechanisms

Driving force of PVT process is the thermal gradient in the reactor, therefore heat transfer must be modelled accurately. The three main heat transfer mechanisms are: conduction, convection and radiation.

In conduction, heat is transferred from hotter spots to colder ones within a material or between two different objects. At low scales, particles with higher kinetic energy (higher temperature) transfer their energy to particles with lower kinetic energy (lower temperature) by collisions. Moreover, in atomic lattices, conduction can occur due to lattice vibrational waves called phonons. The conduction heat flux is proportional to the temperature gradient:

$$q = -k\nabla T \tag{3}$$

In *Eq.(3)*, q is the heat flux (W/m^2), ∇T is the temperature gradient (K/m) and k corresponds to the thermal conductivity (W/(m·K)).

Thermal conductivity is the ability of a material to transfer heat through it. Solids have normally higher thermal conductivities compared to liquids and gases due to their tighter molecular spacing. According to *Eq.(3)*, conduction mechanism becomes more efficient with a larger temperature gradient or larger thermal conductivity [12].

Convection consists in heat transfer because of bulk movement of a fluid. Gases and liquids are not good thermal conductors, nevertheless they can transfer heat efficiently by convection. Therefore, convection involves mass movement, in contrast to conduction, which involves phonons or free particle migrations. Nevertheless, they have in common the necessity of a medium to flow and a temperature difference [13].

Nonetheless, since PVT is carried out under vacuum conditions, convection does not play an important role in the process.

The last mechanism is radiation. It consists of the generation of electromagnetic radiation due to thermal motion of matter particles. Therefore, any material whose temperature is greater than absolute zero emits thermal radiation.

The ideal case, known as black body, is a body which perfectly absorbs all electromagnetic radiation regardless the angle of incidence or frequency, while its emitted radiation follows the Planck's law, shown in *Eq. (4)*:

$$B_v(v,T) = \frac{2hv^3}{c^2}\frac{1}{e^{\frac{hv}{k_BT}} - 1} \tag{4}$$

B_v is the spectral radiance, the surface radiance per unit frequency, per unit surface and per solid angle, whose units are $W \cdot sr^{-1} \cdot m^{-2} \cdot Hz^{-1}$. h is the Planck constant, v is the frequency, c the speed of light, k_B the Boltzmann constant and T the temperature [14].

The law follows the behaviour of *Figure* 6. Thus, more radiation will be emitted when the body temperature is higher. In addition, radiation has a temperature dependent maximum. For instance, the Sun surface temperature is approximately 6000 K and emits both ultraviolet and infrared radiation. At room temperature, bodies emit mostly infrared radiation [15].
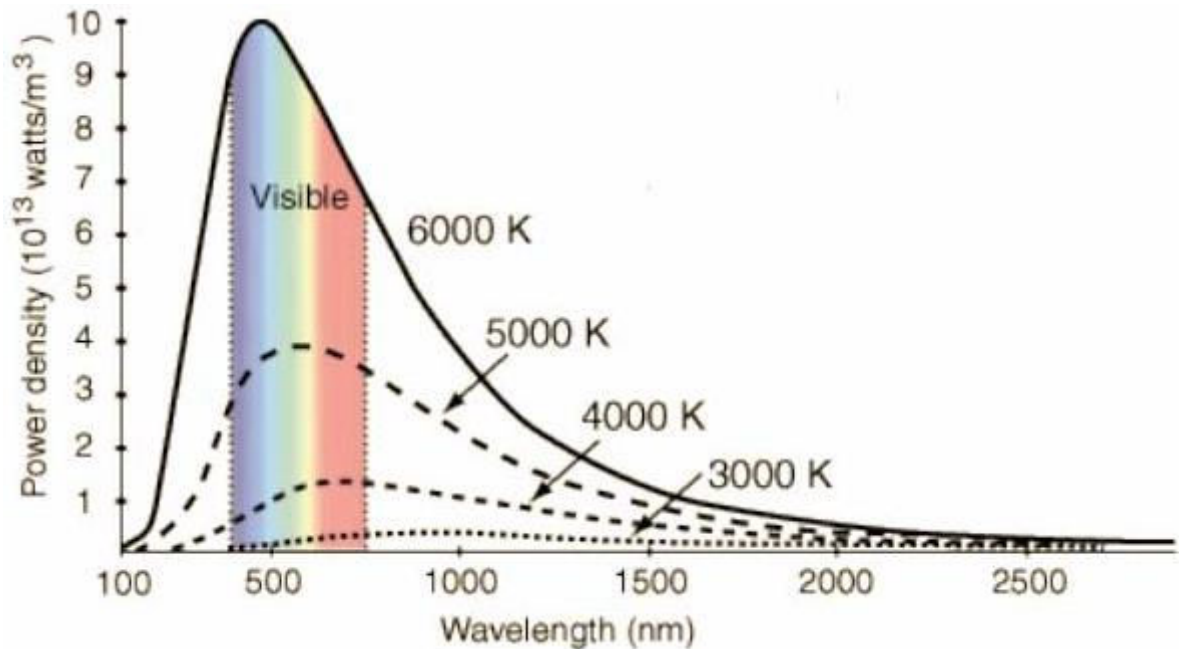

Figure 6. Planck's law behaviour [16].

If the Planck's law is integrated for all frequencies, Stefan-Boltzmann law is obtained. The law states the power of the emitted radiation of a surface area is proportional to the fourth power of its temperature [13]:

$$P = \sigma A T^4 \tag{5}$$

σ is the Stefan-Boltzmann constant (≈ 5.670 $W \cdot m^{-2} \cdot K^{-4}$), A is the surface area and T the surface temperature.

So far, black bodies were considered, but in reality most materials do not possess that behaviour. Those are called gray bodies, which are imperfect black bodies. They absorb partially the incoming radiation. The ratio the radiation emission between black body and gray body is called emissivity, denoted by ε. Emissivity of a black body is 1, therefore the emissivity of a gray body will always lie between 0 and 1. There are similar quantities, such as absorptivity (α), which is the amount of radiation absorbed compared to a black body. For this reason, these mentioned gray body properties must be included in Stefan-Boltzmann law as in *Eq. (6)*, whereby emissivity is included [17].

$$P = \sigma \varepsilon A T^4 \tag{6}$$

Understanding the mechanism, surfaces can exchange heat by having a temperature greater than absolute zero and necessity of a medium in between. According to energy conservation, absorptivity (α), transmissivity (τ) and reflectivity (ρ) must add up to 1. Nevertheless, since we are considering opaque surfaces, transmissivity is 0:

$$\alpha + \tau + \rho = 1 \rightarrow \alpha + \rho = 1 \tag{7}$$

The last law to consider in thermal radiation, is the so-called Kirchoff's law of thermal radiation. This law establishes "*for an arbitrary body emitting and absorbing thermal radiation in thermodynamic equilibrium, absorptivity is equal to emissivity*" *[12]*. Combining Kirchoff's law ($\alpha=\varepsilon$) and *Eq.* (7), a relation between reflectivity and emissivity is obtained as in *Eq. (8):*

$$\alpha + \rho = 1 \rightarrow \varepsilon + \rho = 1 \rightarrow \rho = 1 - \varepsilon \tag{8}$$

The heat flux of a surface k due to thermal radiation considers two contributions: emission and reflection. In *Eq. (9)*, the first term corresponds to thermal emission, while the second term represents the reflection in surface k.

$$q_{k,out} = \varepsilon_k \sigma T_k^{\,4} + \rho_k q_{k,in}$$

$$q_{k,out} = \varepsilon_k \sigma T_k^{\,4} + (1 - \varepsilon_k) q_{k,in} \tag{9}$$

The emission term is the Planck's law for gray bodies. Nonetheless, the reflection term depends on the system geometry. It is proportional to the incoming heat flux, which it is dependent on the view factor *(F)*. View factor is the radiation proportion which leaves a surface and strikes another surface. Thus, F_{jk} is the proportion of radiation that leaves surfaces *j* and strikes surface *k* [18].

$$q_{k,in} = F_{jk}q_{j,out} \tag{10}$$

$$\sum_{j=1}^{N} F_{jk} = 1 \tag{11}$$

Taking everything into account, the heat flux of a surface *k* is the emission of thermal radiation according to its temperature plus the reflection of the incoming radiation of the rest *j* surfaces. This behaviour is depicted in *Eq. (12)*.

$$q_{k,out} = \varepsilon_k \sigma T_k^{4} + (1 - \varepsilon_k) \sum_{j=1}^{N} F_{jk}q_{j,out} \tag{12}$$

The calculation of the view factor can be performed by doing the double integral between the two surfaces involved, shown in *Eq. (13)*. *r* is the distance between surfaces and θ_j and θ_k are the angles between respective surface normal and ray between the two surfaces [18].

$$F_{jk} = \frac{1}{A_j} \int_{A_1} \int_{A_2} \frac{cos\theta_j cos\theta_k}{\pi r^2} dA_k dA_j \tag{13}$$

2.5 Radiation modelling

In the PVT process, the temperature profile is a key parameter to predict accurately since the temperature gradient is the driving force of this growth process. According to *Eq. (6)*, the intensity of emitted radiation is proportional to the fourth power of the surface temperature (T^4). PVT process is performed at such high temperatures *(≈2000ºC)* that radiation becomes the main heat transfer mechanism.

In the present work, the used FEM software for the prediction of the parameters during the PVT process is COMSOL Multiphysics. Only surface-to-surface (S2S) radiation was considered. S2S radiation means heat transfer exclusively between surfaces in a transparent medium. COMSOL Multiphysics has three different model to include S2S radiation mechanism: direct area integration, hemicube and ray shooting.

2.5.1 Direct area integration

Direct area integration directly performs the double integral (*Eq.(13)*) over all pair of surfaces to calculate the view factor. Nevertheless, surface shadowing or obstruction are not considered in this model.

The reciprocity relationship states an equality between two surfaces and their view factor [13]:

$$A_A F_{AB} = A_B F_{BA} \tag{14}$$

This relationship is always fulfilled by the direct area integration method. Although ambient view factor could not be correct depending on the geometry and the generated mesh. Moreover, the method becomes computationally expensive if there are a great number of elements and surfaces. Thus, this model is useful under very specific conditions and circumstances, for this reason it is rarely used [19].

2.5.2 Hemicube

Nusselt analogy is a graphical method to obtain view factors. The hemicube model is based on this analogy. It establishes that the view factor between a differential surface dA_i and a surface A_j is obtained by projecting the surface A_j onto the surface of a unit hemisphere, and then projecting into the base, which is a unit circle. The resulting view factor is the differential surface dA_i times the unit circle proportion covered by the projected surface A_j [20].
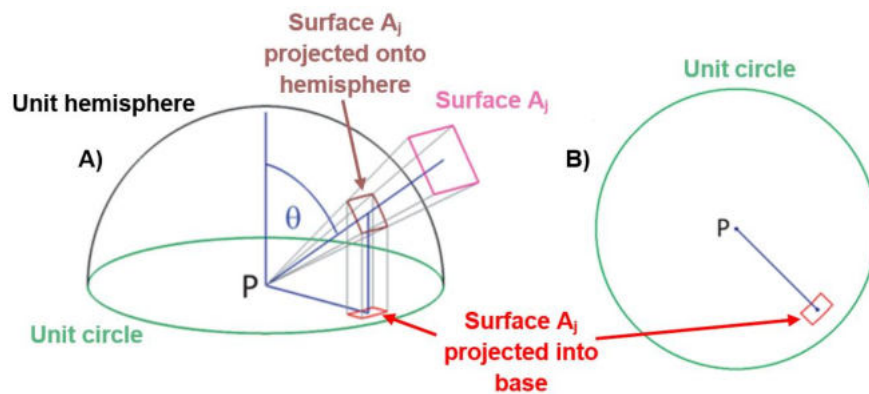

Figure 7. a) Nusselt analogy b) Nusselt analogy viewed from above [21].

In the hemicube model, instead of a hemisphere, a hemicube is projected onto the receiving surface. This theoretical hemicube is subdivided into smaller pixels. Finally, the incoming thermal radiation is projected into these discretized pixels and view factor is evaluated by counting the number of pixels whereby the incoming radiation was projected. The number of discretized pixels is controlled by the radiation resolution. Thanks to this parameter, the user can choose the number of discretizations or pixels in the hemicube. *Figure 8* exemplifies this by showing hemicubes whose radiation resolutions are 256 and 1024, respectively. By increasing the radiation resolution, the reciprocity relationship will be more accurate [19].
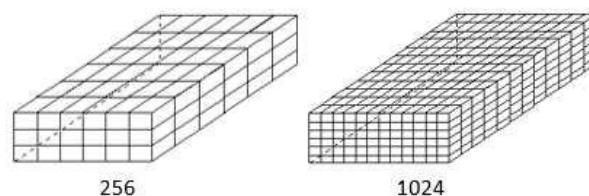

Figure 8. Hemicubes with radiation resolutions of 256 and 1024 [22].

Shadowing is treated by z-buffering, a technique to determine whether an element is obstructed. The depth coordinates (z-value) of the different surface are stored and compared to check if there is shadowing. This is an efficient way to consider surface shadowing [23].

2.5.3 Ray shooting

Ray shooting traces the trajectory of particles in the given geometry. Since thermal radiation is considered, the photon is the relevant particle. Each ray is shot in reverse way and can be reflected, absorbed or transmitted along that reverse path [24]. This method is suitable when angle-dependent emissivity, semitransparency or specular reflectivity are necessary. Thus, each ray represents a fraction of the irradiance from the surrounding surfaces.

The model starts shooting n_{res}^2+1 rays for 3D geometry and $n_{res}+1$ for 2D geometry. This n_{res} parameter is controlled by the radiation resolution. Trajectories are computed until the rays go away from the geometry or the intensity becomes too small, regulated by the tolerance. Along the trajectories, adjacent rays can detect differences in the radiosity or hit different features. In those cases, more rays are shot in between, up to the parameter maximum number of adaptations. When a ray hits a surface, an additional ray is shot from that surface, up to maximal number of reflections [19].

In order to gain a better understanding of the model, consider the case of the *Figure 9*. Rays are shot from the small spot in the centre of the semicircle, which represents a non-reflective, unit emissivity and fixed temperature surface. In *Figure 9a*, each ray sees the same thermal load when hitting the semicircle surface. Increasing the radiation resolution will not have any effect since there is no difference in the radiosity along the surface due to the constant temperature.

In the other case (*Figure 9b*), a small feature is added, represented by a red spot with also a unit emissivity, but different temperature. One of the rays will hit this different temperature feature, detecting something different to the adjacent rays. Thus, more rays will be shot in between to increase the accuracy in this area. In this case, modifying the maximal number of adaptions will increase the accuracy of the results.
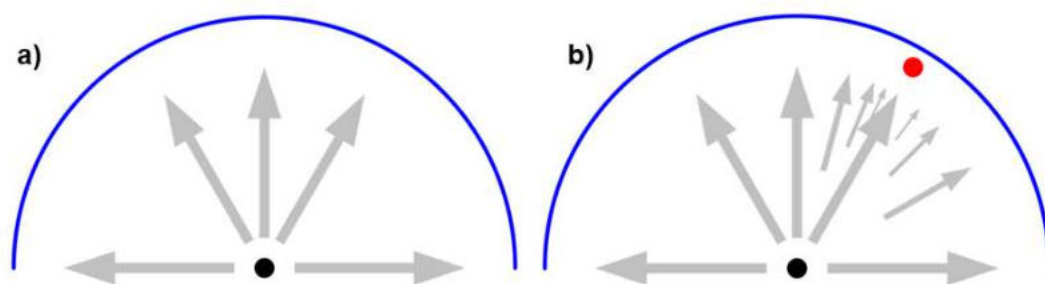
Figure 9. 2D simple scheme of ray shooting model [19]. a) Geometry with no small feature. b) Geometry with small feature.
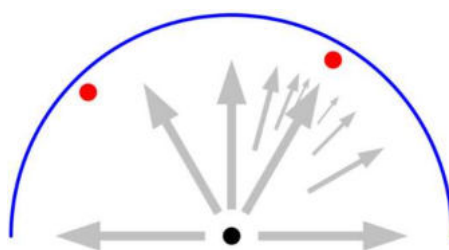

Figure 10. 2D simple ray shooting scheme with two small features [19].

Finally, considering the geometry shown in *Figure 10*, radiation resolution is a key factor in this case. Using the initial radiation resolution, the small feature in the right is already detected. Nonetheless, the left one is no hit by any ray, therefore it is not detected. By increasing the radiation resolution, more rays are shot from the central spot. Eventually, one of these new rays will detect this second small feature, starting the adaptation process.

Overall, every radiation model has its own advantages and disadvantages in terms of accuracy or computational cost. The usage of each of them will depend on the geometry complexity, needed accuracy and available computational resources. *Table 2* depicts the capabilities of each radiation model.

Table 2. Advantages and disadvantages of the different radiation models [25].

	Direct area integration	Hemicube	Ray shooting
Supported dimensions	3D, 2Daxi, 2D, 1Daxi, 1D	3D, 2Daxi, 2D, 1Daxi, 1D	3D, 2Daxi, 2D
Shadowing effects	No	Yes	Yes
Diffuse reflection	Yes	Yes	Yes
Specular reflection	No	No	Yes
Refraction	No	No	Yes
Directional properties	No	No	Yes
Wavelength-dependent properties	Yes	Yes	Yes
External radiation source	Yes	Yes	Yes
Symmetry	Yes	Yes	Yes
View factor update control	Yes	Yes	Yes

3 Methodology

3.1 COMSOL Multiphysics software

COMSOL Multiphysics is a finite element solver software used for analysing various physics and engineering applications. The name Multiphysics comes from the possibility of coupling different physical phenomena such as heat transfer and magnetic field coupling to analyse induction heating.

Figure 11 presents the graphical user interface (GUI) of COMSOL Multiphysics, which has four main areas: ribbon (1), model builder or model tree (2), settings window (3) and graphics window (4).

The ribbon is a section at the top which contains different tabs and buttons to perform most of the modelling tasks such as choosing materials, constructing the geometry or selecting a type of study, among others. Although this can also be done in the model builder, which is actually more intuitive, because it reflects the modelling workflow: set necessary definitions or parameters, construct geometry, choose the materials, set the physics of the geometry, construct the mesh, simulate or study the geometry and visualize the results. Then, the settings windows allow you to choose and modify the options of every model builder node. Finally, the graphics window displays the geometry, the mesh or the results depending on your choice.
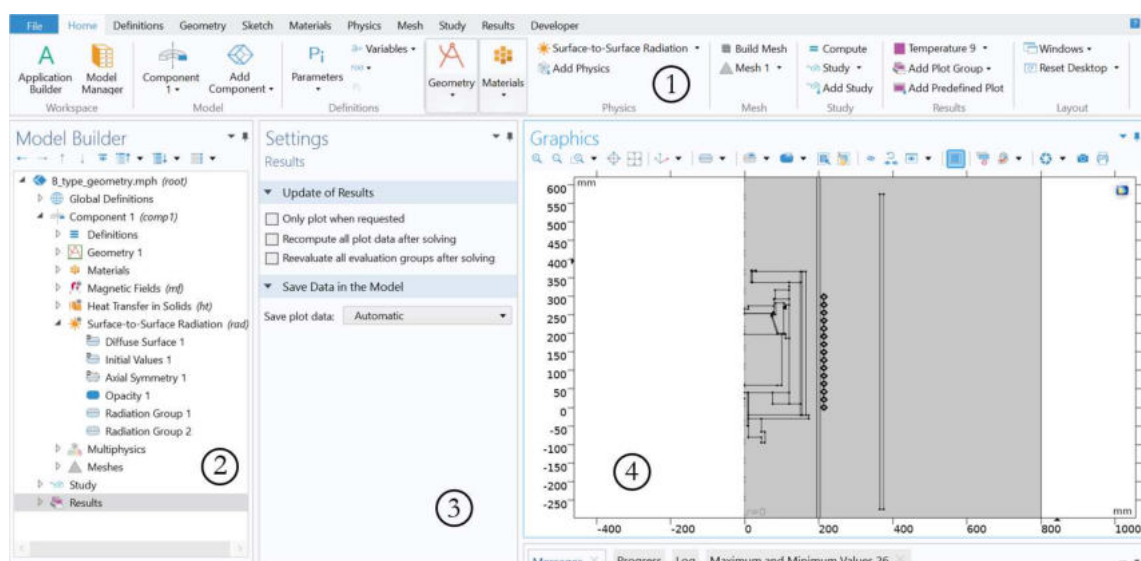
Figure 11. GUI of COMSOL Multiphysics

3.2 Reactor geometry

The PVT reactor has the geometry shown in *Figure 12*, there is also a zoom-in in its growth chamber where the SiC seed can be seen on top. The materials or domains are: air, copper, insulator, crucible, **SiC (seed and source)** and glass (denoted by a white domain). There are actually two insulators, the blocks closer to the crucible (called Insulator 1) and the block on the right (called Insulator 2). Considering the reactor geometry is cylindrical, symmetric around *z*-axis, a 2D axisymmetric geometry of the reactor is used for the simulations. This option reflects and simulates a slice of the actual 3D geometry and revolves the results around the symmetric axis [26].
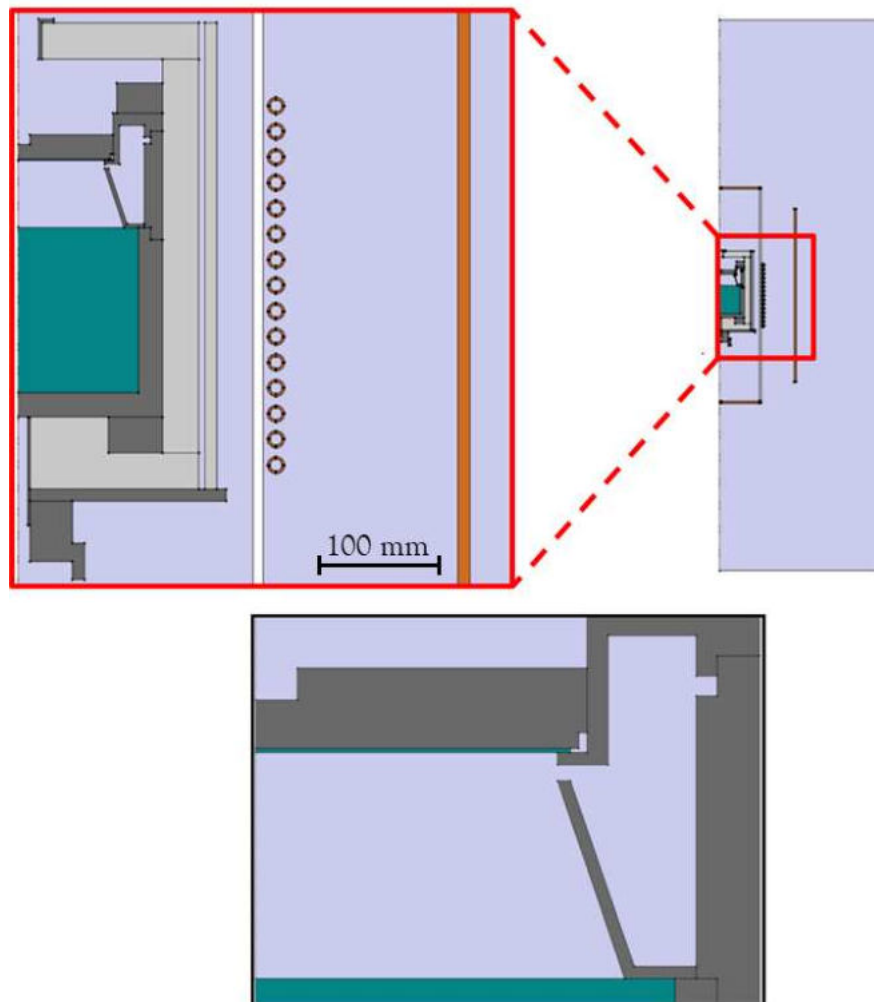
Figure 12. Geometry of the PVT reactor and its growth chamber.

3.3 Material properties

A material must be chosen for each geometry domain. For the PVT process without considering the source as a powder, mass transport and absorbing media, the necessary properties are: density (ρ), thermal conductivity (k), heat capacity (C_p), surface emissivity (ε), electrical conductivity (σ), relative permittivity (ε_r) and relative permeability (μ_r). These properties can be constant values, explicit functions or interpolation from known values. Below, the properties of the different materials can be found. It is important to note that thermal conductivity of insulators are temperature and pressure dependent. *Table 7* displays the temperature dependency and *Table 8* shows the pressure dependency including the temperature dependency.

Table 3. Properties of air (*T represents temperature and p the pressure*).

Air	
ρ [kg/m^3]	$\dfrac{0.02897p}{R}\dfrac{1}{T}$
σ [W/m·K]	0
$\varepsilon_r \,/\, \mu_r$	$1\,/\,1$
At $p = 1$ atm: $k(T) = -0.00228 + 1.15 \cdot 10^{-4} \cdot T - 7.90 \cdot 10^{-8} \cdot T^2 + 4.12 \cdot 10^{-11} \cdot T^3 - 7.44 \cdot 10^{-15} \cdot T^4 \left[\dfrac{W}{m \cdot K}\right]$	
At $p = 1$ atm: $C_p(T) = 1047.6366 - 0.3726T + 9.45 \cdot 10^{-4} \cdot T^2 - 6.02 \cdot 10^{-7} \cdot T^3 + 1.29 \cdot 10^{-10} \cdot T^4 \left[\dfrac{J}{kg \cdot K}\right]$	

Table 4. Properties of copper.

Coil (copper)	
ρ [kg/m^3]	8960
k [W/m·K]	400
Cp [J/kg·K]	385
σ [S/m]	6·10^7
ε_r / μ_r	1 / 1

Table 5. Properties of insulator 1 made of Mersen CBCF 18-2000.

Insulator 1 (Mersen CBCF 18-2000)	
ρ [kg/m^3]	150
k [W/m·K]	Interpolation (*Table 7* and *Table 8*)
Cp [J/kg·K]	1000
ε	0.8
σ [S/m]	200
ε_r / μ_r	1 / 1

Table 6. Properties of insulator 2 made of Felt Mersen Soft.

Insulator 2 (Felt Mersen Soft)	
ρ [kg/m^3]	75
k [W/m·K]	Interpolation (*Table 7* and *Table 8*)
Cp [J/kg·K]	1930
ε	0.8
σ [S/m]	200
ε_r / μ_r	1 / 1

Table 7. Thermal conductivity of insulators 1 and 2 depending on temperature.

T [K]	k [W/m·K]
273.15	0.25
673.15	0.25
1073.15	0.35
1473.15	0.48
1873.15	0.69
2273.15	1
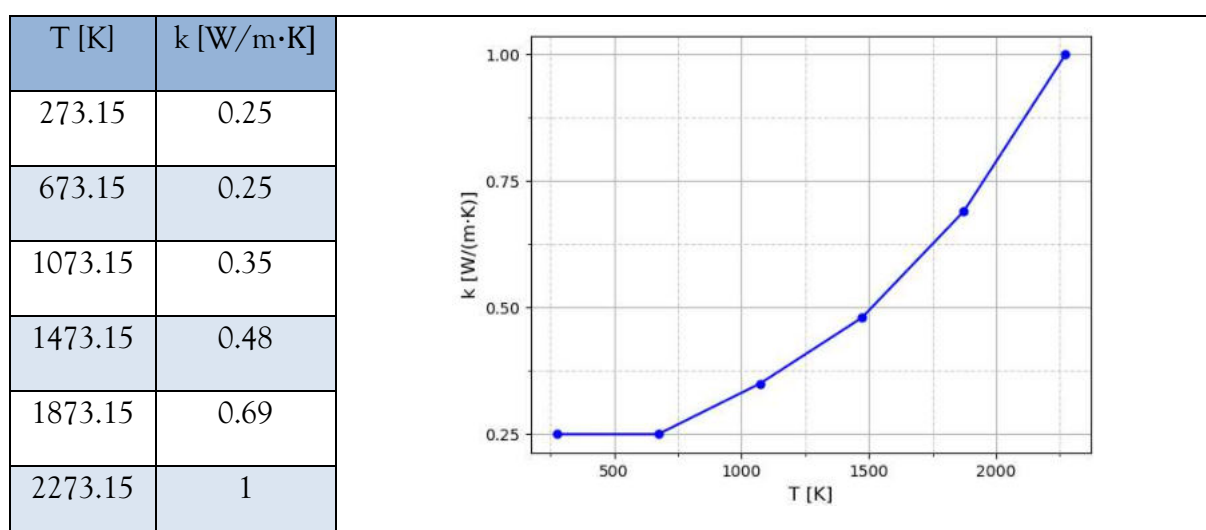
Table 8. Thermal conductivity of insulators depending on temperature and pressure and pressure-related coefficients [27].

$k(T, P) = \alpha \cdot k(T)$	P [mbar]	850	460	100	50	20	10	5
	α	0.65	0.60	0.55	0.53	0.51	0.49	0.47

Table 9. Properties of the crucible.

Crucible	
ρ [kg/m^3]	1770
k [W/m·K]	Interpolation (*Table 10*)
Cp [J/kg·K]	Interpolation (*Table 11*)
ε	0.8
σ [S/m]	Interpolation (*Table 12*)
ε_r / μ_r	1 / 1

Table 10. Thermal conductivity of the crucible.

T [K]	k [W/(m·K)]
273	119
353	96.175
508	72.7
825	52.13
1330	39.585
2259	31.151
2919	28.42
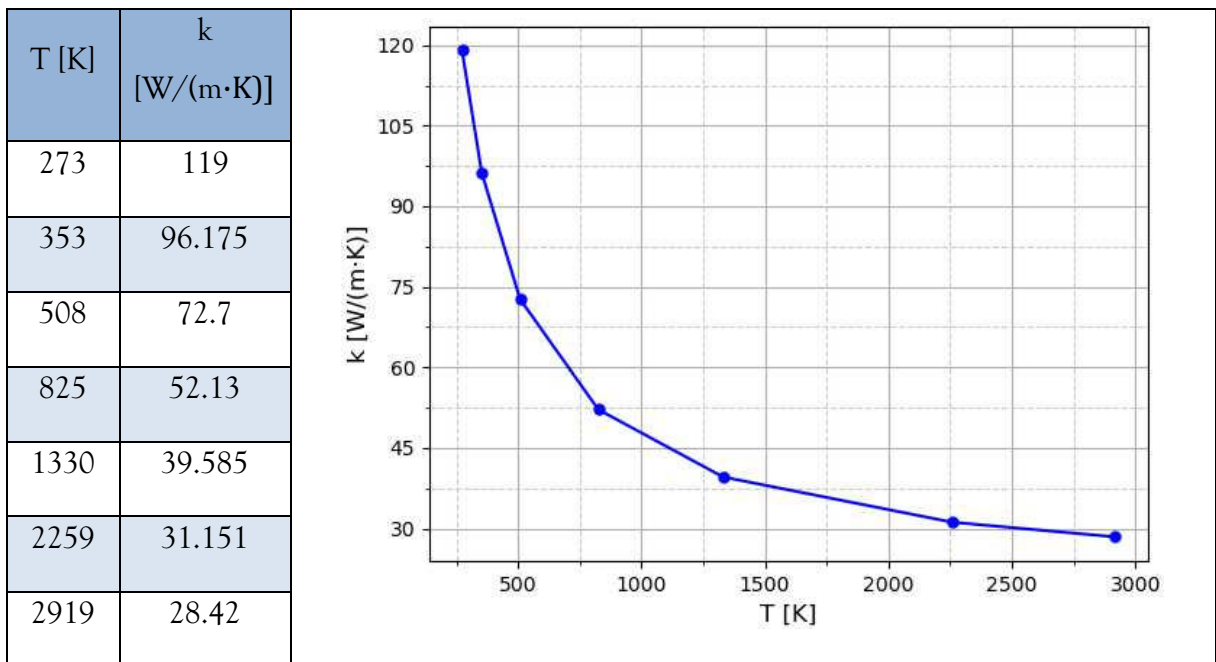
Table 11. Heat capacity of the crucible.

T [K]	C_p [J/(kg·K)]
300	510
400	850
500	1062.51
650	1275
850	1530
1000	1657.5
1200	1785
2000	1912.5
2973	1953.3
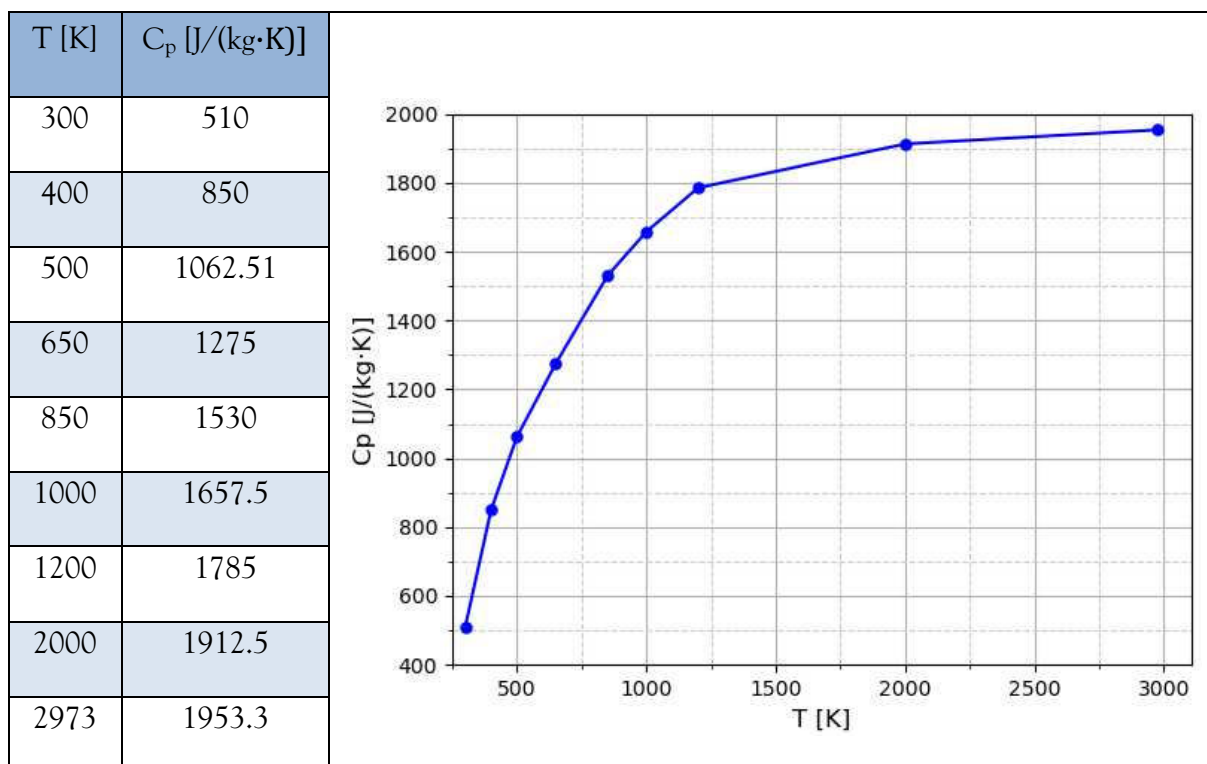
Table 12. Electrical conductivity of crucible.

T [K]	σ [S/m]
273	74700
461	86284.8
670	98100
932	109800
1343	118800
1545	119700
1902	117900
2663	110700
2973	108000
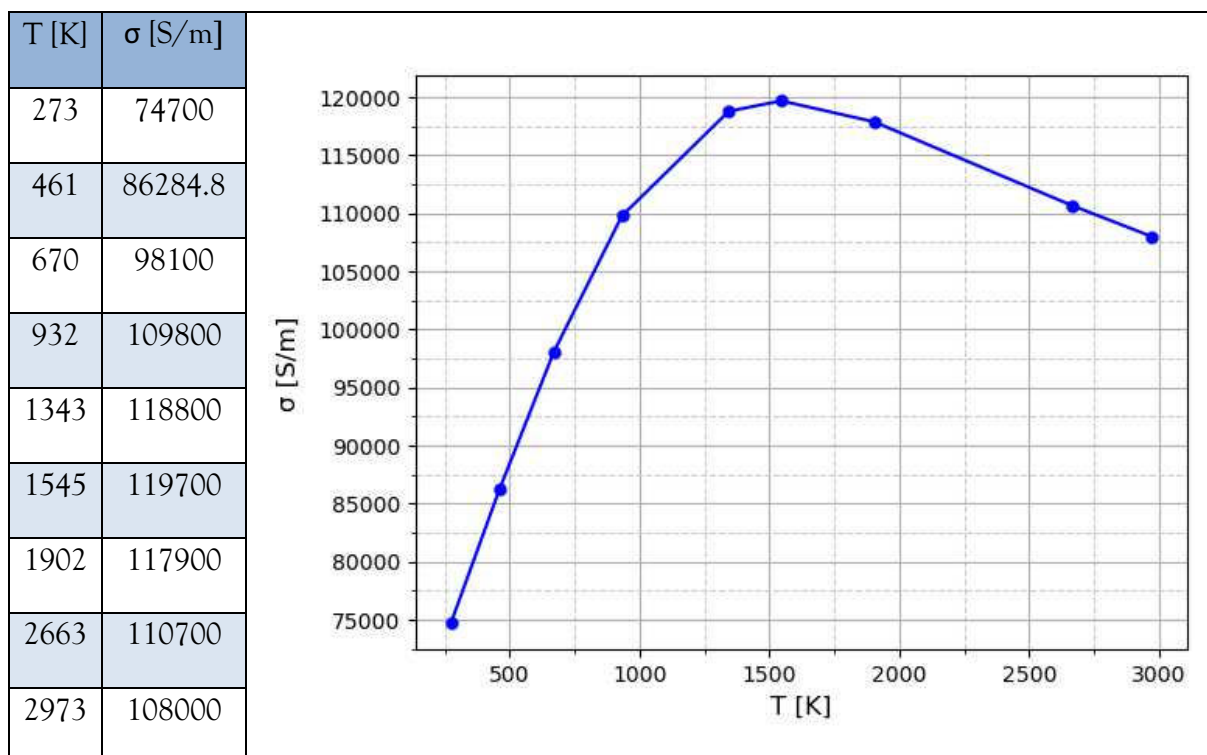
Table 13. Properties of SiC for both source and seed.

SiC		
	Source	Seed
ρ [kg/m³]	2000	3220
k [W/m·K]	10	$288 \cdot \left(\dfrac{300}{T}\right)^{1.29}$
Cp [J/kg·K]	1000	Interpolation (*Table 14*)
ε	0.8	0.8
σ [S/m]	0	1000
ε_r / μ_r	10 / 1	10 / 1

Table 14. Heat capacity of the SiC seed.

T [K]	C_p [J/kg·K]
300	670
400	855
600	1031
1000	1193
1500	1281
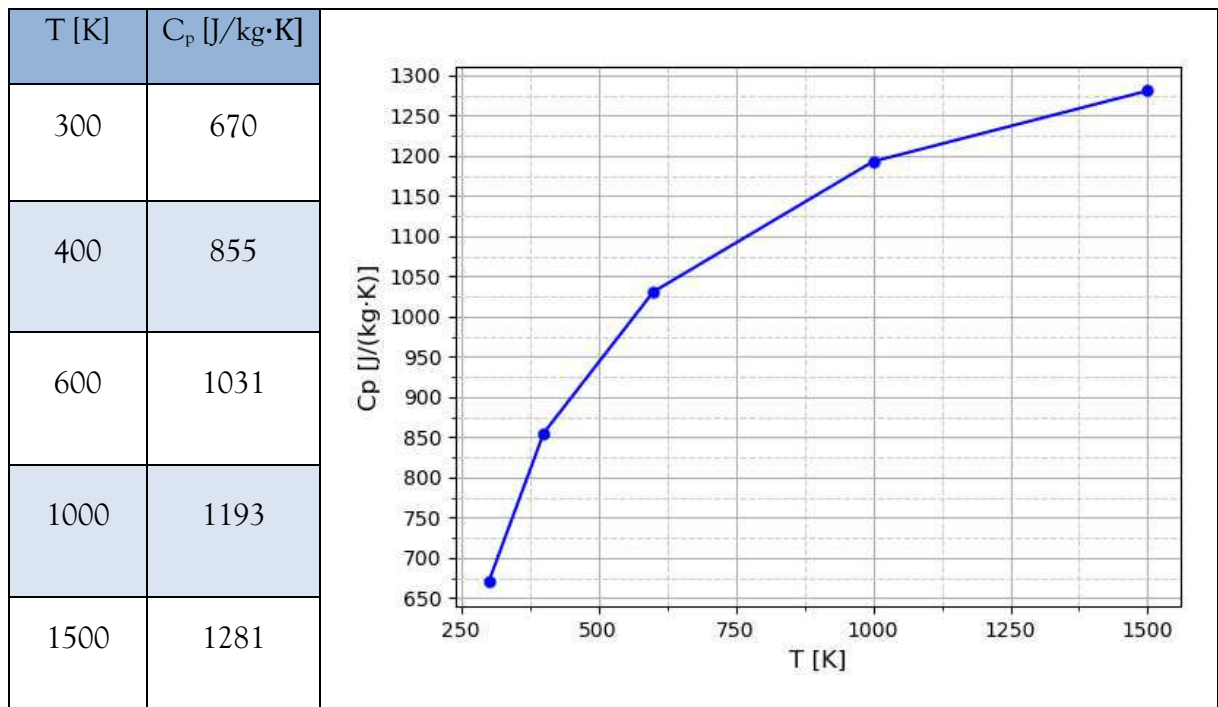
Table 15. Properties of glass.

Glass	
ρ [kg/m^3]	2210
k [W/m·K]	1.4
Cp [J/kg·K]	730
σ [S/m]	$1 \cdot 10^{-14}$
ε_r	4.2
μ_r	1

3.4 Physics, initial and boundary conditions

In COMSOL Multiphysics, the user must choose the physic equations that are going to be present during the simulation. In our already mentioned case, PVT process without mass transport, no absorbing media and treating the SiC as a solid instead as a powder (*See ending Chapter 2.2*), the necessary physics are: Magnetic fields, Heat transfer and S2S radiation. The physic equations have to be coupled to treat all phenomena correctly. Including the mentioned physics, two multiphysics phenomena will be obtained: induction heating and heat transfer with S2S radiation. The first one is the result of coupling Magnetic field and Heat transfer, while the second one is the coupling of Heat transfer with S2S radiation.

Table 16. Physics coupling of COMSOL Multiphysics.

Physics	Multiphysics
Magnetic fields	Induction heating
Heat transfer	
Heat transfer	Heat transfer with S2S radiation
S2S radiation	

Firstly, the Magnetic fields physics calculates the magnetic field and induced current around the coil, in our case. It solves the Maxwell's equation, being formulated with the magnetic vector potential [28].

$$\nabla \times H = J$$

$$B = \nabla \times A$$

$$J = \sigma E + j\omega D + \sigma(v \times B) + J_e$$

$$E = -j\omega A \tag{15}$$

where H is the magnetic field intensity (A/m), J is the current density (A/m²), B is the magnetic flux density (T), A corresponds to the magnetic vector potential (Wb/m), σ is the electrical conductivity (S/m), E corresponds to the electric field intensity (V/m), j represents the imaginary

unit, ω is the AC current angular frequency, D is the electric displacement field (C/m²), v is the conductor velocity (m/s) and J_e considers externally generated current density. Therefore, it is just necessary to set the conditions of the coil, which is a single conductor of 15 turns. The used power and frequency are 12 kW and 7 kHz, respectively, together with the properties in *Table 4*.

The Heat transfer module is used to include all necessary heat transfers mechanisms, in our case: conduction and radiation. In this module, S2S radiation is not included yet, but only surface-to-ambient. The module solves the Fourier's law (conduction) and any additional contribution (radiation in this case) [29]. These both mechanisms are reflected in *Eq.*(16) and *Eq.*(17), respectively.

$$q = -k\nabla T$$

$$\rho C_p u \cdot \nabla T + \nabla \cdot q = Q + Q_{ted} \tag{16}$$

$$-n \cdot q = \varepsilon\sigma(T_{amb}{}^4 - T^4) \tag{17}$$

First equation is already shown in *Chapter 2.4*. As regards second equation, ρ is the density (kg/m³), C_p is the specific heat capacity at constant pressure (J/(kg·K), u is the translational motion velocity vector (m/s), Q corresponds to additional heat sources (W/m³) and Q_{ted} includes thermoelastic effects in solids. In *Eq.* (17), n is the surface vector, ε the emissivity, σ is the Stefan-Boltzmann constant, T_{amb} is the temperature of the surrounding ambient (K) and T corresponds to the surface temperature (K).

Since conduction is automatically included in the module, only surface-to-ambient radiation conditions should be included. Surface-to-ambient radiation is set to the outer surface of the reactor chamber, using a surface emissivity (ε) of 0.8 for the whole surface and an ambient temperature (T_{amb}) of 323.15 K representing the cooling system.

Finally, the S2S radiation module is used to consider the heat transfer due to radiation between surfaces. The thermal radiation is treated as energy transfer between boundaries with non-participating media [30]. The equations that include this phenomenon are detailed in *Chapter 2.4*. All surfaces of the reactor are included for S2S radiation and are treated as diffuse surfaces. Moreover, it is set the air domains as transparent media.

Figure 13 details these reactor surfaces included in the module.
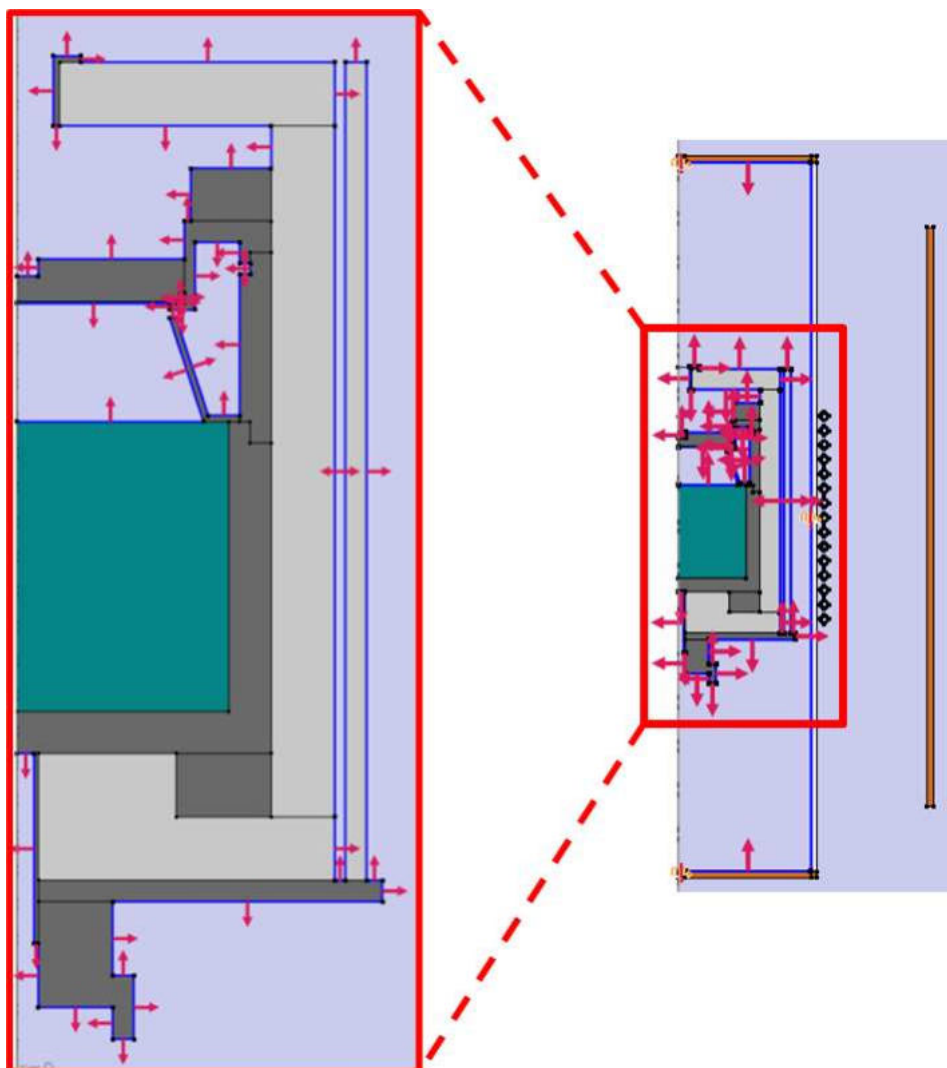
Figure 13. Boundaries considered for S2S radiation.

3.5 Solver settings

COMSOL Multiphysics allows the user to choose how to perform the simulation and how the PDEs are solved.

To simulate the PVT reactor with the physics mentioned in the *Chapter 3.4* a two-step study is conducted. Initially a *Frequency domain* study is conducted to solve the Magnetic fields physics. Thereupon a *Stationary* step is done to solve the rest of the physics, including the multiphysics.

Table 17. Simulation steps for the PVT reactor.

	Step 1: Frequency domain study (nonlinear solver)	Step 2: Stationary study (nonlinear solver)
Physics and Multiphysics solved	Magnetic fields	Heat transfer S2S radiation Induction heating Heat transfer with S2S radiation

Nonlinear solver is based on the damped Newton method by computing iterations in the form:

$$U_{n+1} = U_0 + \lambda \delta U \tag{18}$$

 where U is the solution vector, λ a damping factor between 0 and 1 and δU is the Newton step. The equations are transformed into a discrete form and the software constructs a linearized model from an initial guess U_0 and it is solved by means of $f(U_0)\, \delta U = - f(U_0)$, where $f(U_0)$ is the Jacobian matrix at point U_0. Then, the iteration is done and the error E is estimated by calculating $f(U_0)E = - f(U_1)$. If the error E is larger than error of the previous iteration, the software reduces the value of λ and recalculates U_1 until the error of the new iteration is smaller than the one from the previous iteration [31, 32].

There are two criterions for stopping the iteration: solution or residual. Both relies on error comparison between iterations. In the first case, the iterations stops when the estimated error of the current U solution approximation is less than a predefined tolerance. This relative error is estimated by:

$$err = \sqrt{\frac{1}{M}} \sqrt{\sum_{j=1}^{M} \frac{1}{N_j} \sum_{i=1}^{N_j} \left(\frac{|E_{i,j}|}{W_{i,j}}\right)^2} \qquad (19)$$

where M is the number of fields, N_j is the number of degrees of freedom in the field j. While j denotes the field, i denotes the degree of freedom index. Degrees of freedom concern the independent parameters to define a mesh node in the system (position, temperature, magnetic field strength, etc.) The more mesh nodes or more involved physics the system has, the more degrees of freedom there will be. Meanwhile, $W_{i,j}=max(|U_{ij}|S_j)$, being S_j the scale factor predefined [33]. Scaling is done to have the different dependent variables at similar scales and avoid problems due to ill-conditioned matrix [34].

In the other case, the algorithm stops the iteration when the relative error is smaller than the predefined tolerance. This relative error is computed by *Eq. (20)*, where F is the current step [33]:

$$err = \sqrt{\frac{1}{M}} \sqrt{\sum_{j=1}^{M} \frac{1}{N_j \widetilde{W}_j^{\,2}} \sum_{i=1}^{N_j} |F_{i,j}|^2} \qquad (20)$$

For the first study step (*Frequency domain*), considering just one physics are being solved (*Magnetic fields*) a Fully coupled solution approach is chosen. This approach performs the damped Newton method on the physics to be solved [35]. An automatic damped Newton method is selected. Thanks to this option, the software adjusts automatically the damping factor in each iteration. An initial damping factor of 1 is chosen, setting also a minimum value of 10^{-4}. A restriction of the damping factor value change per iteration is set to 10. Finally, as Termination criterion "Solution or residual" is chosen, meaning that the software stops the convergence process if the error estimated by either *Eq.*(19*)* or Eq.(20) is lower than the tolerance, which is set to 10^{-3}.

For the second study step (*Stationary step*), a segregated solution approach is chosen. This allows to perform the solution process by splitting it in substeps [36], in our case Temperature and Radiosity converge separately. As a method, *Automatic highly nonlinear (Newton)* is selected, performing automatically (similarly than in the previous step) the damped Newton method more carefully to achieve proper convergence. For both substeps, the initial, minimum and restriction change of damping factor values are $10^{-4}, 10^{-8}$ and 10, respectively. Again, "Solution or residual" is selected as termination criterion.

4 Results and discussion

4.1 Radiation models comparison

As mentioned in *Chapter 2*, temperature gradient is the driving force for the PVT growth process. Since the process is carried out at hight temperatures, radiative heat transfer is the predominant mechanism among the three mechanisms explained in *Chapter 2.4*. Modelling of the radiation during the process is a key factor to get accurate results, thus, the very first step is to verify which of the three radiations models, mentioned in *Chapter 2.5*, is the most suitable for our geometry.

Firstly, the radiation models will be tested in "toy models", geometries which are idealized and simple, to study their behaviour. Thereupon, a simple reactor geometry will be used to visualize the difference between the models. Finally, the actual geometry reactor will be used to test these models in a more realistic system.

It is important to mention that direct area integration model is not used due to its simplicity. It is not possible to get a solution for the reactor geometries using this model owing to its simplicity and limitation. Only hemicube and ray shooting models will be tested.

4.1.1 Toy models

The first "toy model" is just used to ensure both models converge to a similar result for basic geometries without shadowing or other small features. This geometry is shown in *Figure 14*, which consists of an inner and outer cylinder (dark gray domains) made of graphite and the space in between is filled with air (blue domain). The red arrows depict the thermal radiating surfaces of the geometry and air domains are always considered as transparent for thermal radiation.
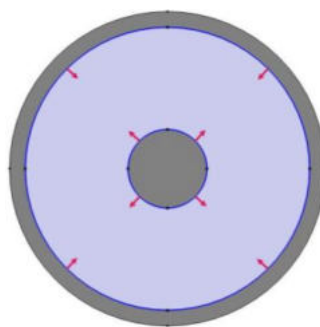
Figure 14. Geometry of the simplest toy model.

Table 18. Properties of graphite.

Graphite	
Density, ρ [kg/m^3]	1950
Thermal conductivity, k [W/m·K]	0.1
Heat capacity at constant pressure, Cp [J/kg·K]	710
Surface emissivity, ε	0.8

Table 18 states the properties of the graphite material. It is important to note that its thermal conductivity has been set so low to make the system less conducive dominant and to emphasize the effect of thermal radiation. If not, the temperature rise at the inner surface of the outer cylinder caused by radiation would be fastly released. In this case, the effect of radiation would not be noticeable. Whereas the air properties for these toy models are the same as indicated in *Table 3* from *Chapter 3.3*.

The used mesh consists of an extremely fine mesh of 24434 elements shown in *Figure 15*. Every domain is made of triangles and it is generated automatically by COMSOL Multiphysics software. The simulation has been carried out three times: just considering conduction, considering conduction and thermal radiation using hemicube model and considering conduction and thermal radiation using ray shooting. All of them are steady state simulation, therefore the results show the equilibrium state of the system. For both radiation models, the radiation resolution is set to 4096. Additionally for ray shooting settings, Tolerance is set to 10^{-4}, maximum number of adaptations is 15 and maximal number of reflections is set to 1000. The simulations took 7, 12 and 17 seconds, respectively.
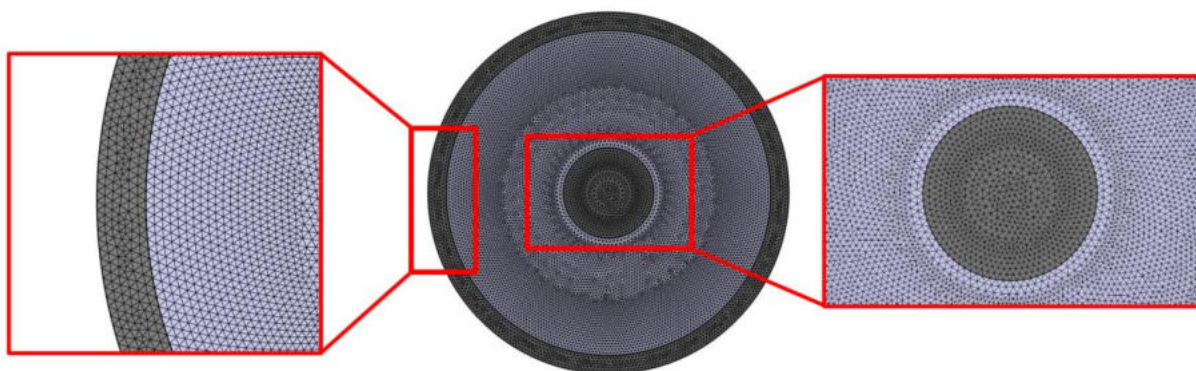
Figure 15. Used mesh for simplest toy model simulation.

The results of these simulations are depicted in *Figure 16*. As it can be seen, including only conduction, the equilibrium state is a temperature gradient from the inner circle at 2200K to room temperature at the outer circle by means of thermal conduction of the air between both cylinders. Meanwhile considering also thermal radiation, it shows the temperature between both cylinders is 2200K. This is because the central cylinder emits thermal radiation which is absorbed by the inner surface of the outer cylinder, while part of this absorbed radiation is also emitted. This increases the temperature of the outer cylinder, leading to a constant temperature of 2200K between both cylinders owing to thermal radiation absorption.
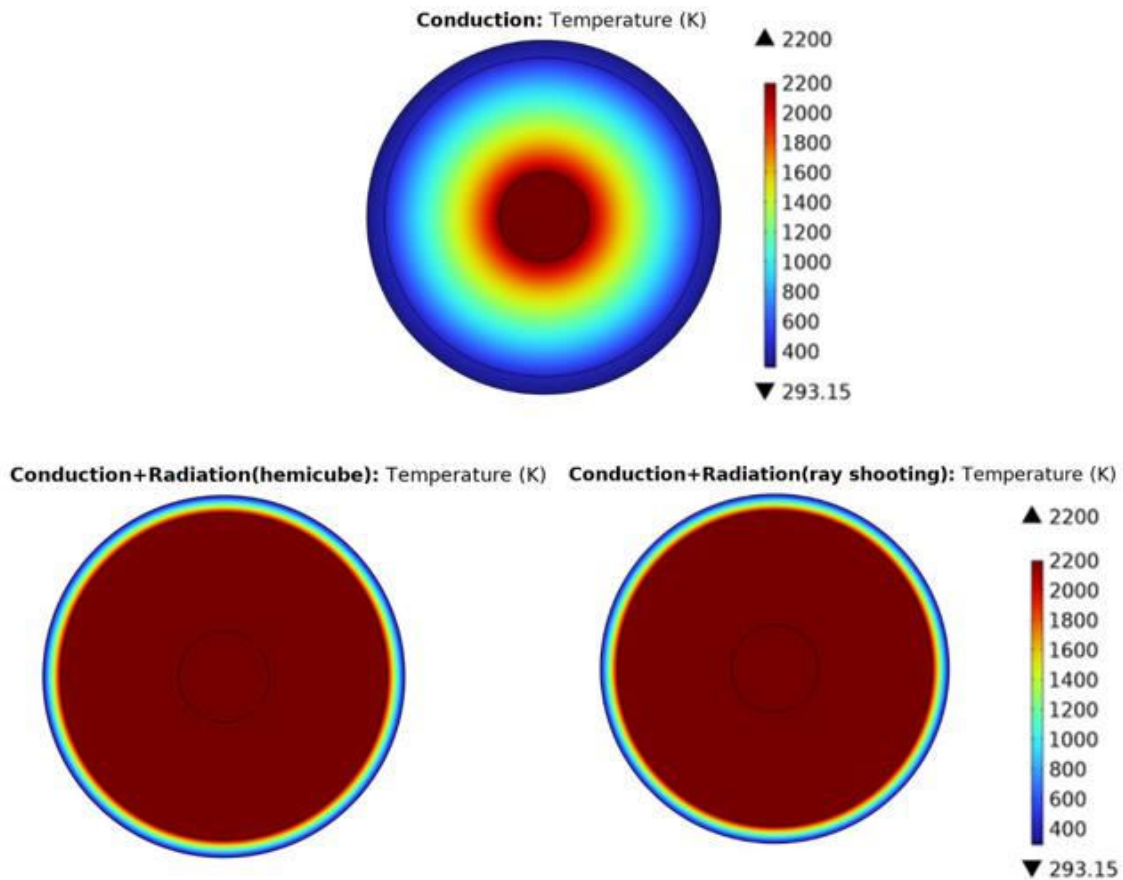
Figure 16. Thermal simulation results from the simplest toy model.

It seems that both radiation models lead to the same result. *Figure 17* shows the temperature difference between the results using hemicube and ray shooting. This difference is small ($\Delta T \approx 0.02K$), reaching its maximum at the inner surface of the outer cylinder, boundary where the S2S radiation plays an important role. In this case, hemicube is the model which converges to higher temperature.
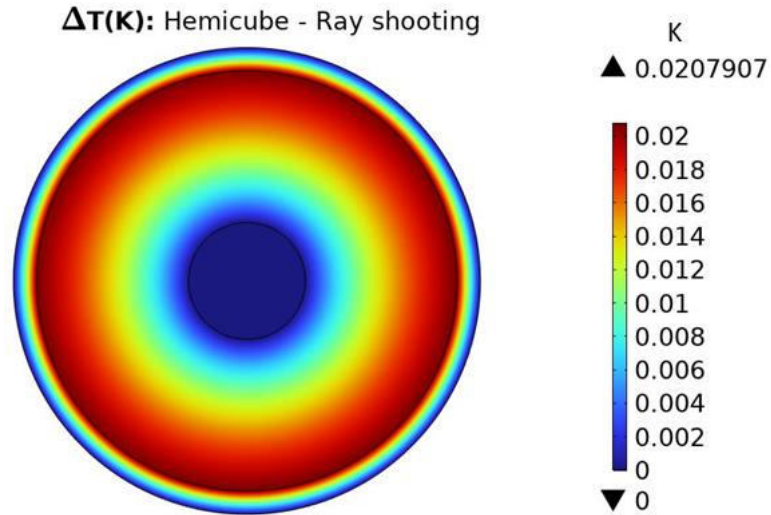
Figure 17. Temperature difference between hemicube and ray shooting results from the simplest toy model simulation.

Hereafter, the shadowing effect is included and tested. The used geometry is the same as depicted in *Figure 14*, but a graphite block between the two cylinders is added. The temperature of the added graphite block is set to 1250K when testing the radiation models. The four block walls are added as additional radiating surfaces. The rest of the boundary conditions are the same as for the previous geometry. This new geometry is depicted in *Figure 18*.
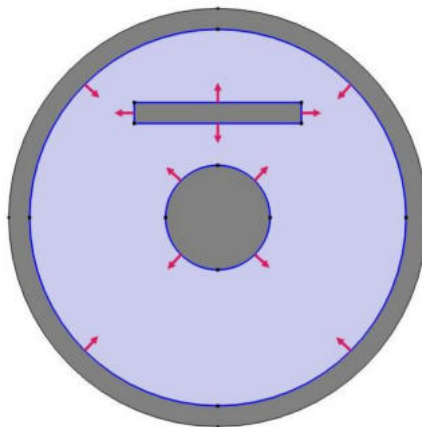
Figure 18. Geometry of the system with a graphite block added.
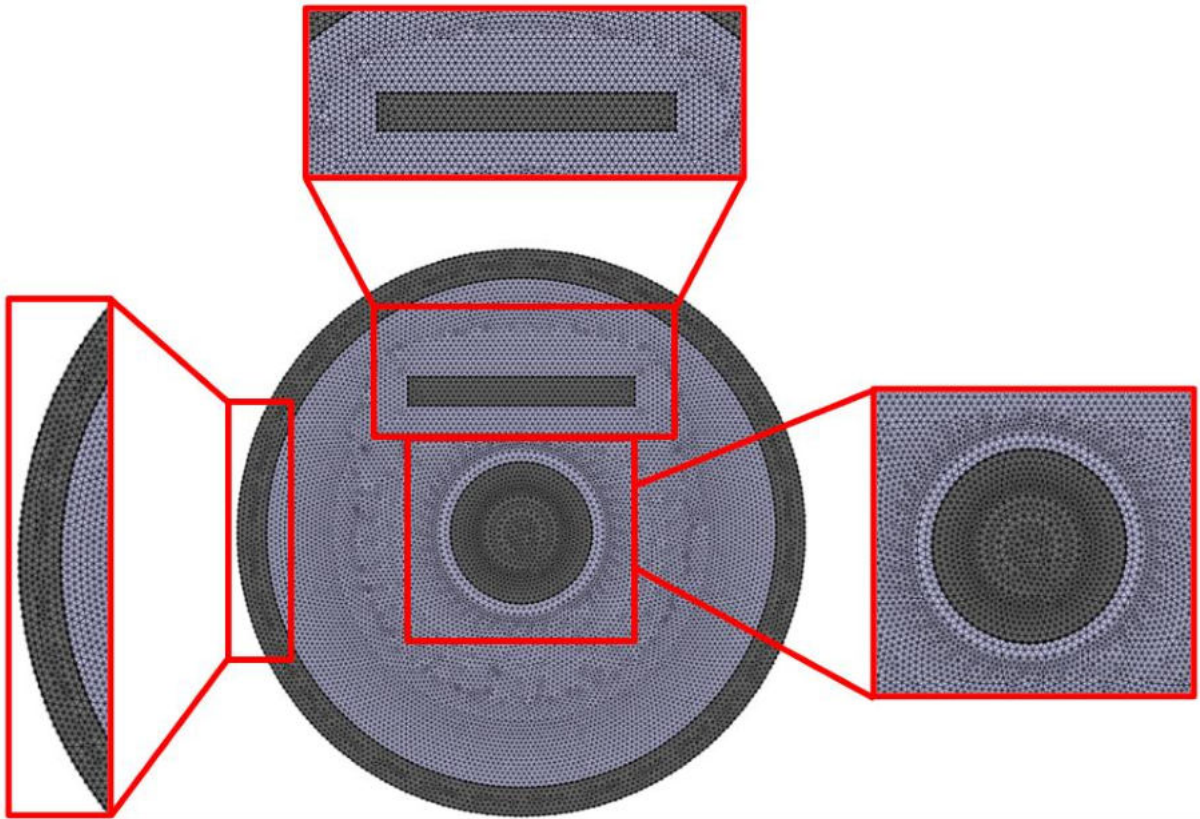
Figure 19. Used mesh for the geometry with block.

As in the previous geometry, the fine mesh was generated automatically by the software. It is shown in *Figure 19* and it consists of 23352 elements. The reduction of the element numbers compared to the previous geometry is due to the block. In this domain, the mesh is made of larger free triangle elements in comparison to the equivalent air domain area in the other geometry. The procedure is the same as before, doing three simulations considering just conduction and including radiation either using hemicube or ray shooting. Their computational times are 3s, 17s and 22, respectively. The slight reduction of computational time for the conduction result is because of the mentioned mesh element number reduction. Nevertheless, the computational time including radiation increased. This time increment is due to the addition of new radiating surfaces. In the simplest case, there was just two radiating surfaces: the inner circle surface and the inner surface of the outer cylinder, while in this case there are six. Having more radiating surfaces makes the view factor calculation more complex.
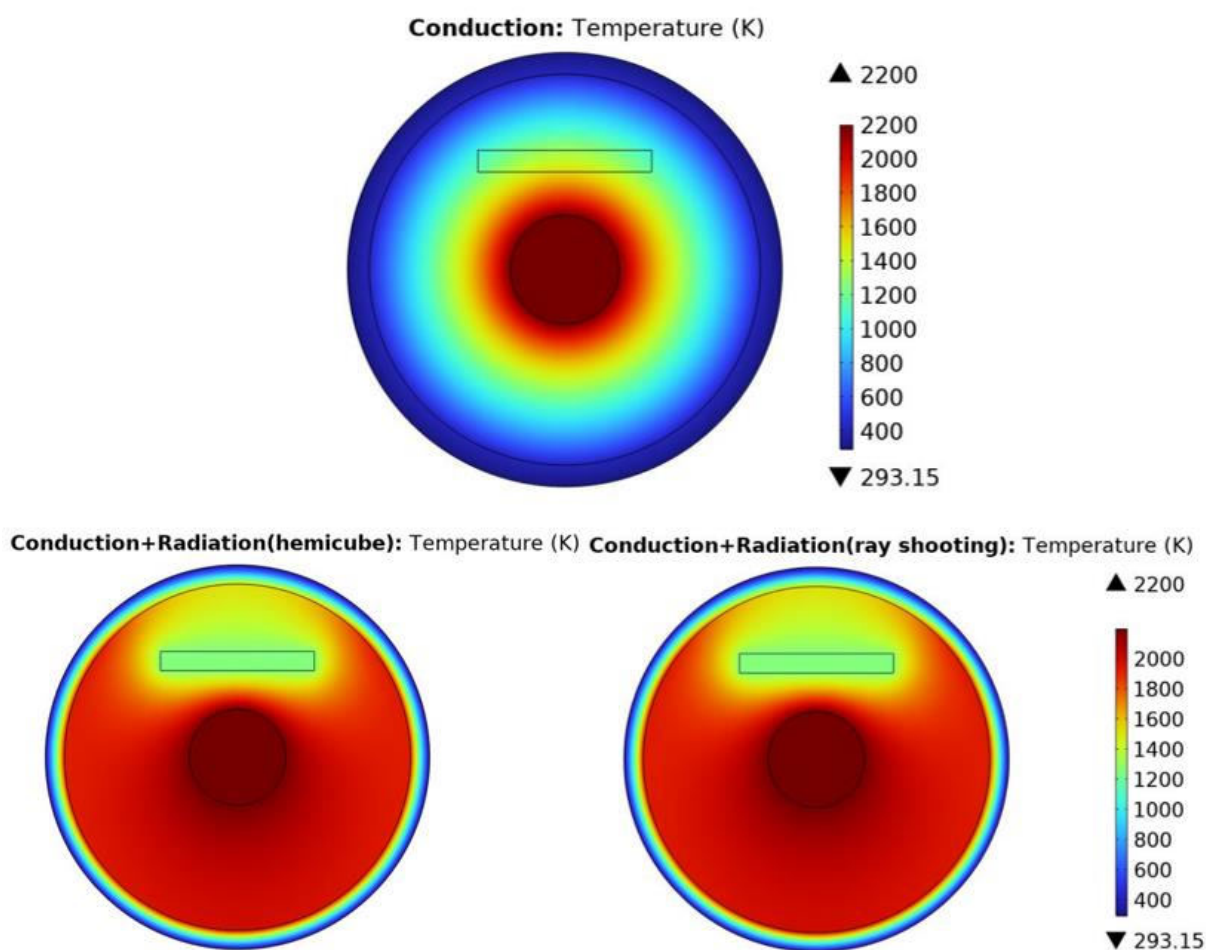
Figure 20. Thermal simulation results adding a block.

Figure 20 reflects the result of these simulations. In the conduction case, the equilibrium state is again a temperature gradient from the inner circle to the outer cylinder. Comparing it to the previous result, the temperature is a bit higher in the block domain. This is due to the different thermal conductivity. The block is made of graphite, whose thermal conductivity was set to 0.1 W/(m·K), which is slightly higher than the thermal conductivity of air at that temperature, being around 0.09-0.07 W/m·K in the surrounding as shown in *Figure 21*. This small difference is what makes the temperature difference between both cases not so high.

Comparing radiation simulations, the shadowing effect seems to be handled correctly. The temperature in the air domain is around 2000K everywhere except behind the block, where it is approximately 1500K.
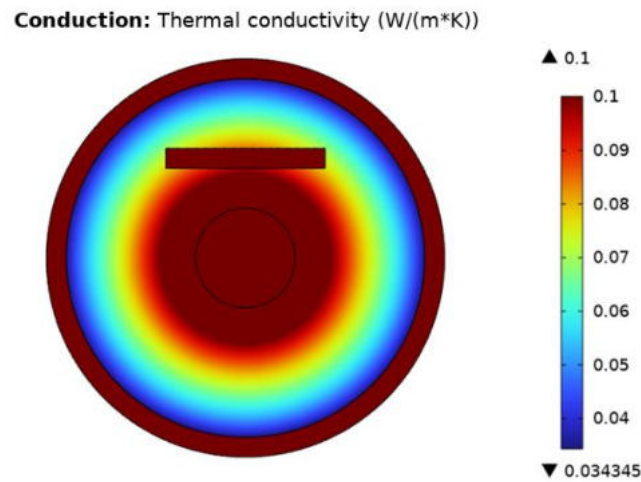
Figure 21. Thermal conductivity just considering conduction.

To check the difference between radiation simulations, the temperature difference between them is checked by subtracting the ray shooting result to the hemicube result. *Figure 22* shows this difference. Generally, there is no noticeable temperature differences, except in specific spots behind the block. In this case, there are some locations where the ray shooting result has higher temperature (negative ΔT), in contrast to the previous geometry whereby hemicube model has always higher temperature along the air domain.
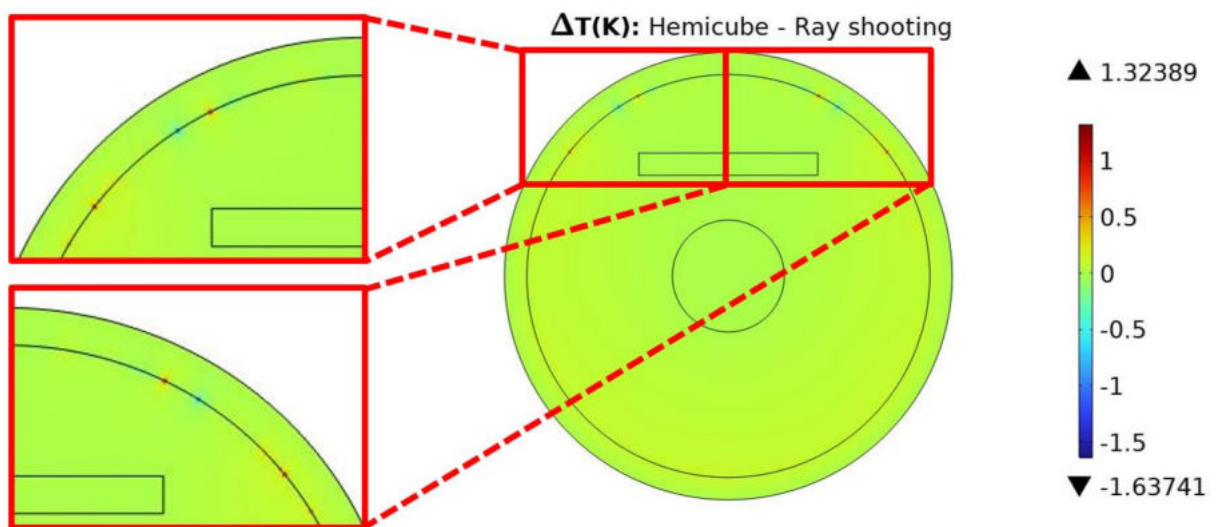
Figure 22. Temperature difference between radiation models when adding a graphite block.

The temperature profile along the arc marked by a red line in *Figure 23* is plotted to check this temperature difference along this boundary.
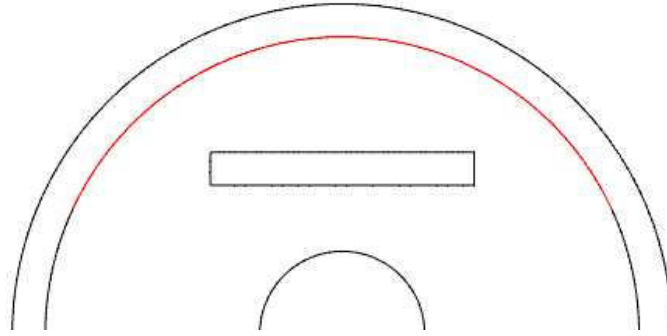
Figure 23. Selected arc portion to check temperatures in red.

In *Figure 24* both temperature profiles are plotted with some zoom-in at different parts. The temperature lowering is very noticeable owing to the shadowing, decreasing around 400K at the middle of the arc. Nevertheless, in a detailed way, these profiles are not completely smooth, especially in both extremes. This might be one of the reasons of the temperature difference at specific locations. Due to these non-smooth results, the temperatures can be different because of fluctuations at different points.

The spots where the curve slope changes abruptly correspond to mesh node positions. This could indicate this mesh does not possess such a good resolution to correctly represent the radiation contribution in this geometry. Possible solutions would be reducing the tolerance to get less-error convergences or increasing the number of mesh elements, thus increasing the node number, to get smoother temperatures profiles.
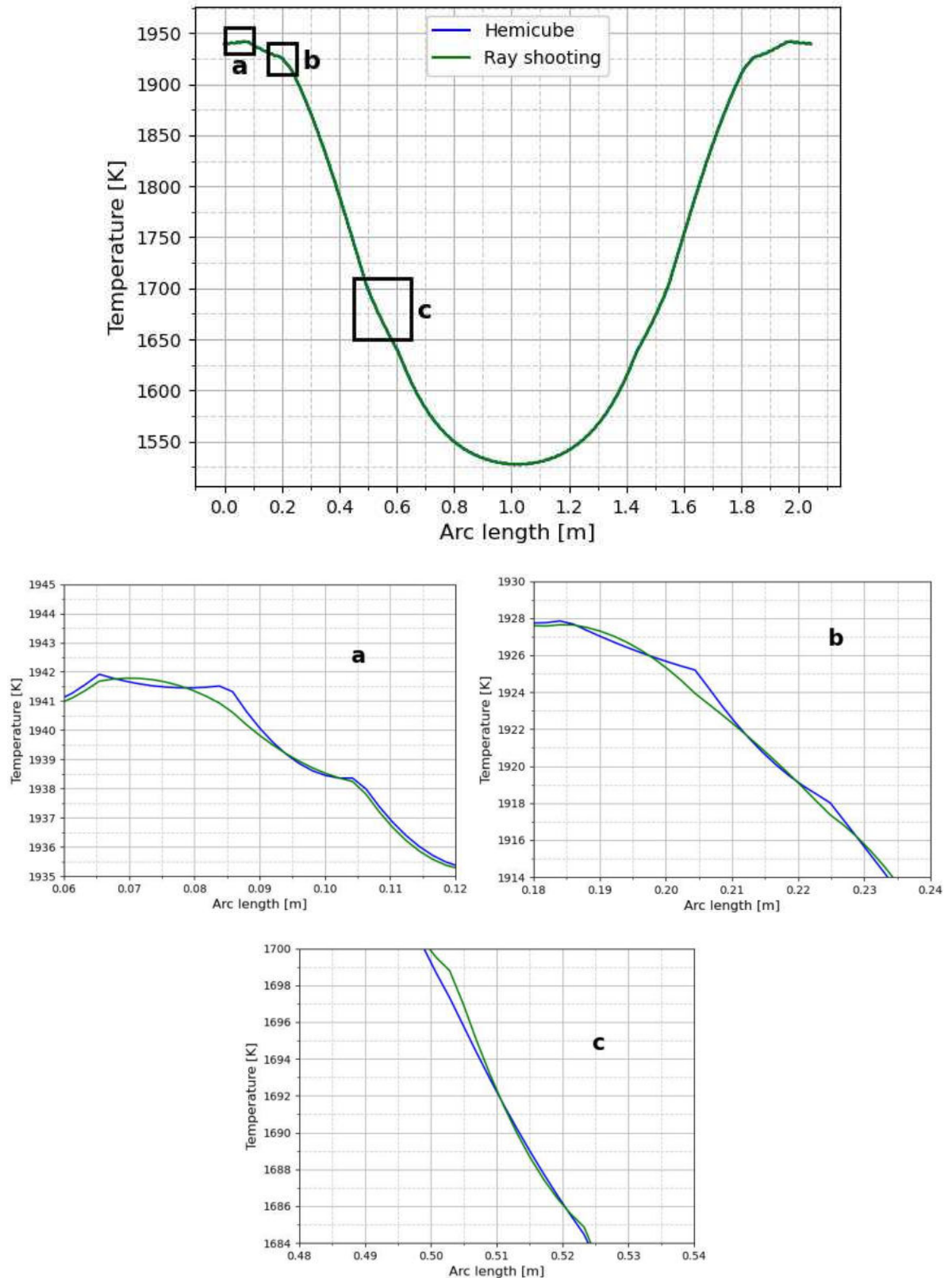
Figure 24. Temperature profile behind the block with some zoom-in for both radiation models.

Thereupon, the shadowing effect is still tested, but now in a different way. Instead of constructing a block and check the temperature decrease behind it, a cavity will be established to check the temperature rise in that open surface. In *Figure 25.a*, the geometry, whose cavity is 7 cm, can be seen. The outer and inner radii of the middle circular domain are 0.5 and 0.45 m, respectively. Thus, the width of this domain is 0.05 m. The conditions are the same as before: the inner circle temperature is set to 2200K, the middle domain with the cavity is set to temperature of 1250K and the outer surface temperature of the outer cylinder is set to room temperature. Simulations just considering conduction and using the radiation models will be again conducted. The used mesh is shown in *Figure 25.b*, which is formed by 23612 elements. All the elements are free triangles. Again, this is a fine mesh generated automatically by the software.
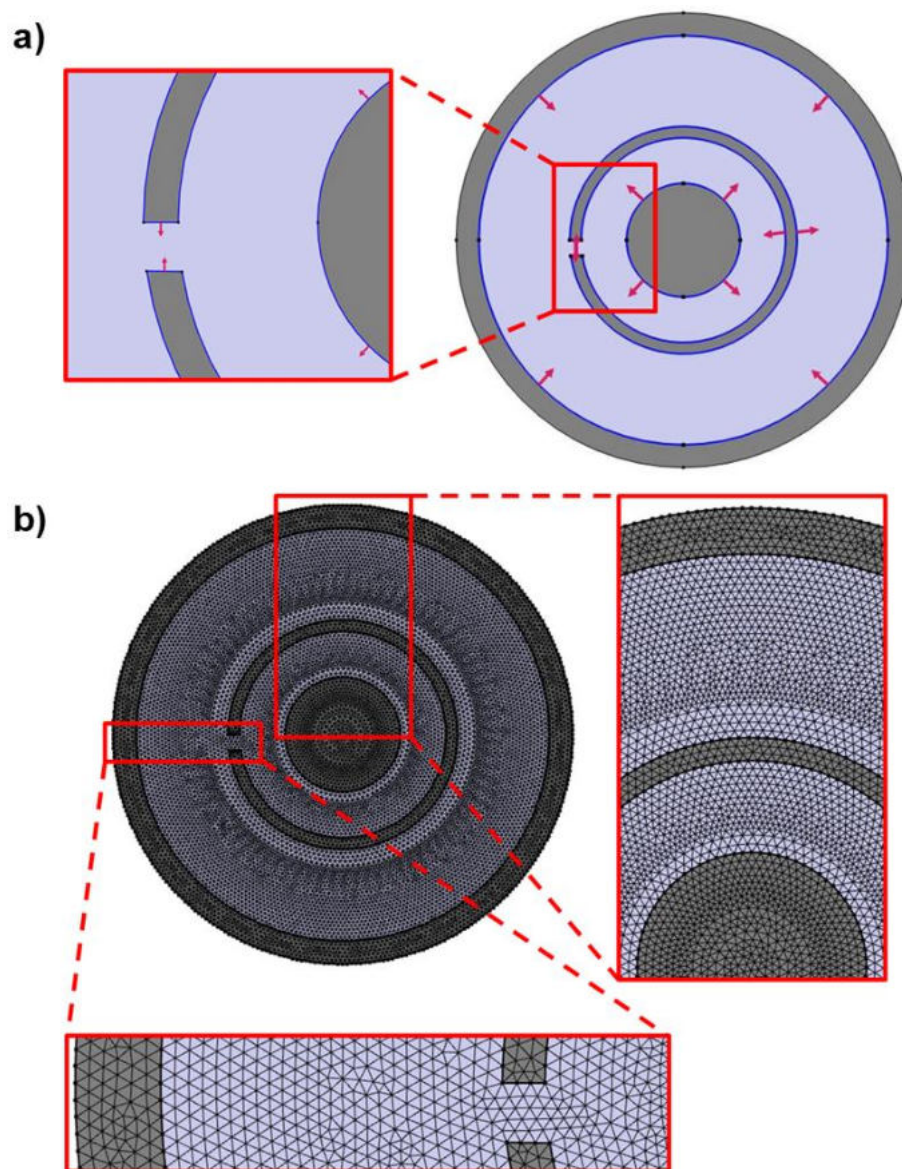
Figure 25. a) Geometry of the system with a 7 cm cavity. b) Mesh used in the geometry with 7 cm cavity.

The computational time for the simulation considering conduction and adding either hemicube or ray shooting are 4s, 7s and 18s, respectively. Although the radiating surfaces are larger, increasing the radiating mesh nodes, the total number of geometry mesh nodes has been reduced sufficiently to have a faster computational time compared to the previous case.

Figure 26 shows the thermal results of this cavity geometry. Considering just conduction, as in the previous geometries, there is a temperature gradient from the central circle to the inner surface of the outer cylinder. Comparing the middle semiarch domain with the cavity region itself, there is no remarkable difference. This might because, as seen in *Figure 21*, the reduced graphite thermal conductivity (0.1 W/m·K) is not so different to air thermal conductivity at these temperatures. Regarding the radiation models, their temperature profiles are very similar, having a temperature of around 1300K in the air domain beyond the semiarch domain. Nevertheless, it seems that there is a temperature rise in the inner surface of the outer cylinder when looking to the cavity direction. In this area, the temperature increases up to 1400K. This is also checked by plotting the temperature profile along two different directions in the geometry.
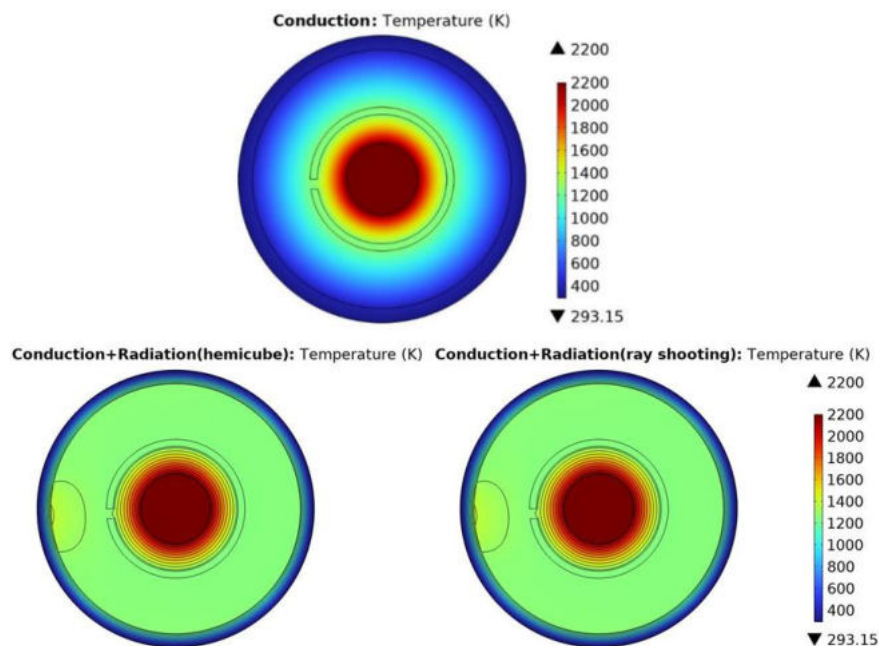
Figure 26. Thermal simulation results for cavity geometry adding isothermal lines in the radiation results.

These two directions are shown in *Figure 27*: cavity direction and upwards direction. The cavity direction goes from the center to left, going through the cavity, passing on the higher temperature region and the outer cylinder. The upwards direction goes from the center to upward, passing through the semiarch domain and the outer cylinder.
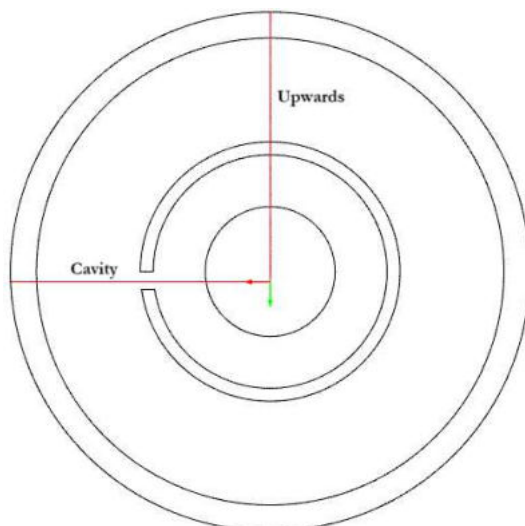
Figure 27. Temperature profile check directions: cavity direction and upwards direction.

Figure 28 is the result of plotting temperature along both directions using the hemicube model. The area of interest is near the interface between the air domain and the outer cylinder. It is clear that in the cavity direction the temperature is higher, reaching 1400K, compared to the upward direction, which is close to be constant at around 1275K. The cavity reduces the shadowing effect, thus, the surface can absorb more radiation (emitted by the inner circle and semiarch domain) and the temperature rise is larger. Meanwhile, the rest of this inner surface just absorbs radiation from the semiarch domain, having a smaller temperature increment and seeming almost as constant temperature along the semiarch and air domains.
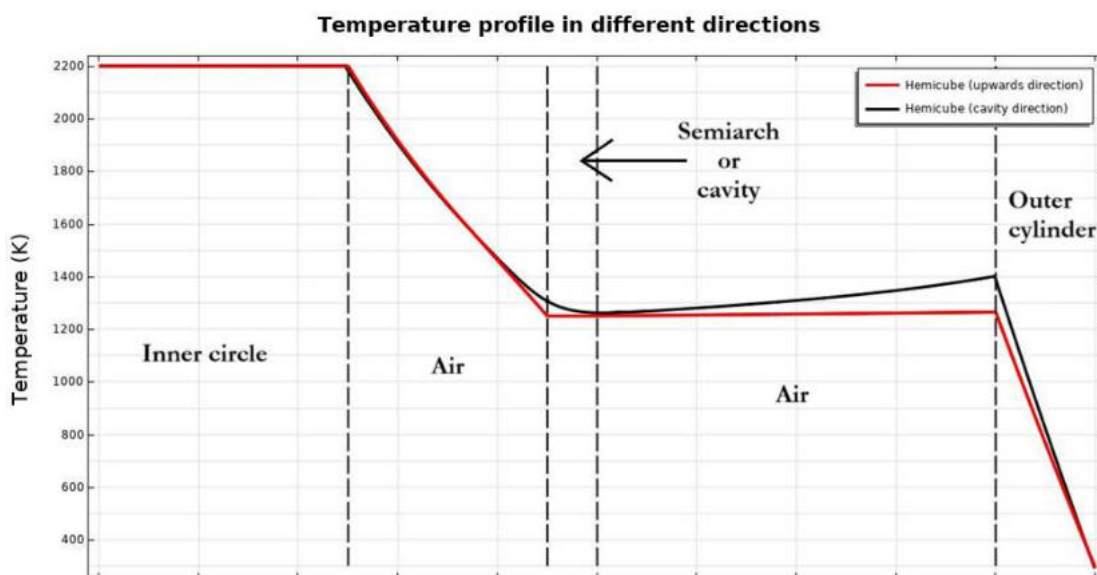
Figure 28. Temperature profile in different directions along the cavity geometry.

The temperature difference between the radiation models is shown in *Figure 29*. As in the previous geometry (*Figure 22*), the temperature difference is prominent at specific spots in the inner surface. Again, in some spots the hemicube's temperature is higher, while in others it is the opposite.
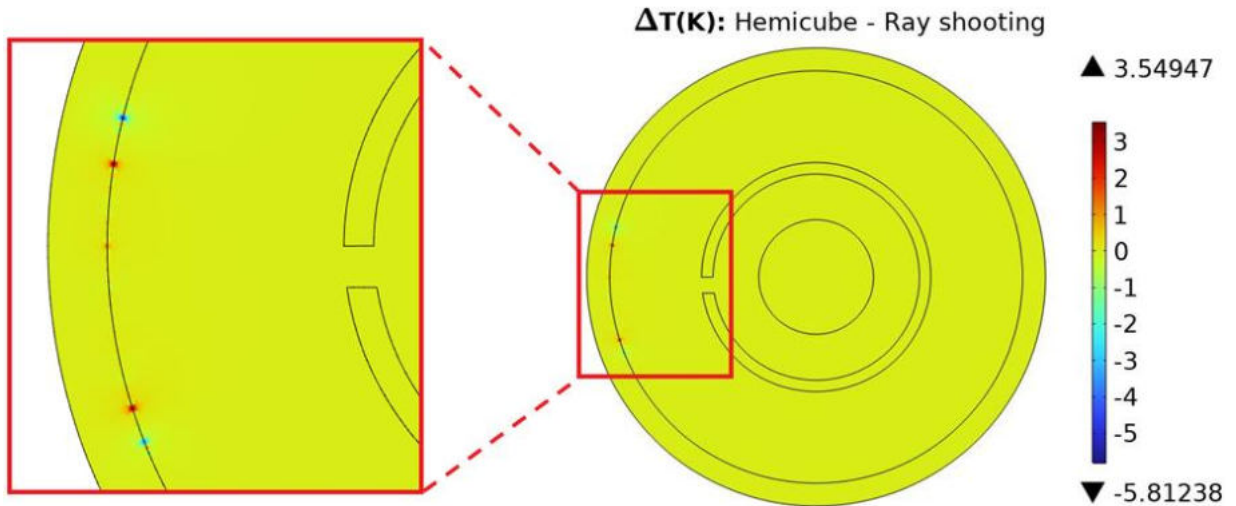
Figure 29. Temperature difference between radiation models in the cavity geometry.

As in *Figure 24*, the temperature profile of the inner surface along the higher temperature region is plotted for the cavity geometry, zoom-ing at different parts. *Figure 30.a* and *Figure 30.b* expose the extrems of this region, where the temperature rise starts abruptly due to the increased incoming thermal radiation because of the cavity. The ray shooting profile is more jagged compared to the hemicube. This uncontinous temperature profile in these areas might be caused, as explained in *Chapter 2.5.3*, by the ray shooting algorithm. It compares the radiosity or other thermal features between adjacent rays and adapts itself by shooting more rays up to a maximum number of times or until reaching a pre-set difference between adjacent rays (tolerance). Potential causes of this rough profile are: mesh element size, ray shooting tolerance or maximal number of adaptations parameter.

Mesh element size could not be small enough to achieve a correct temperature transition from the low incoming radiation to the high incoming radiation regions. The size might be so large that temperature changes too abruptly and ray shooting cannot resolve this change with the set parameters. The easiest solution would be to reduce the mesh element size, thus increasing the mesh node number. Thanks to this node increment, more points along the surface would be considered and the temperature profile better resolved. Moreover, increasing the maximal

number of adaptations parameters and lowering the ray shooting tolerance would also help, given that the model would perform more adaptations between adjacent rays and would lead to more accurate results because of the reduced tolerance.
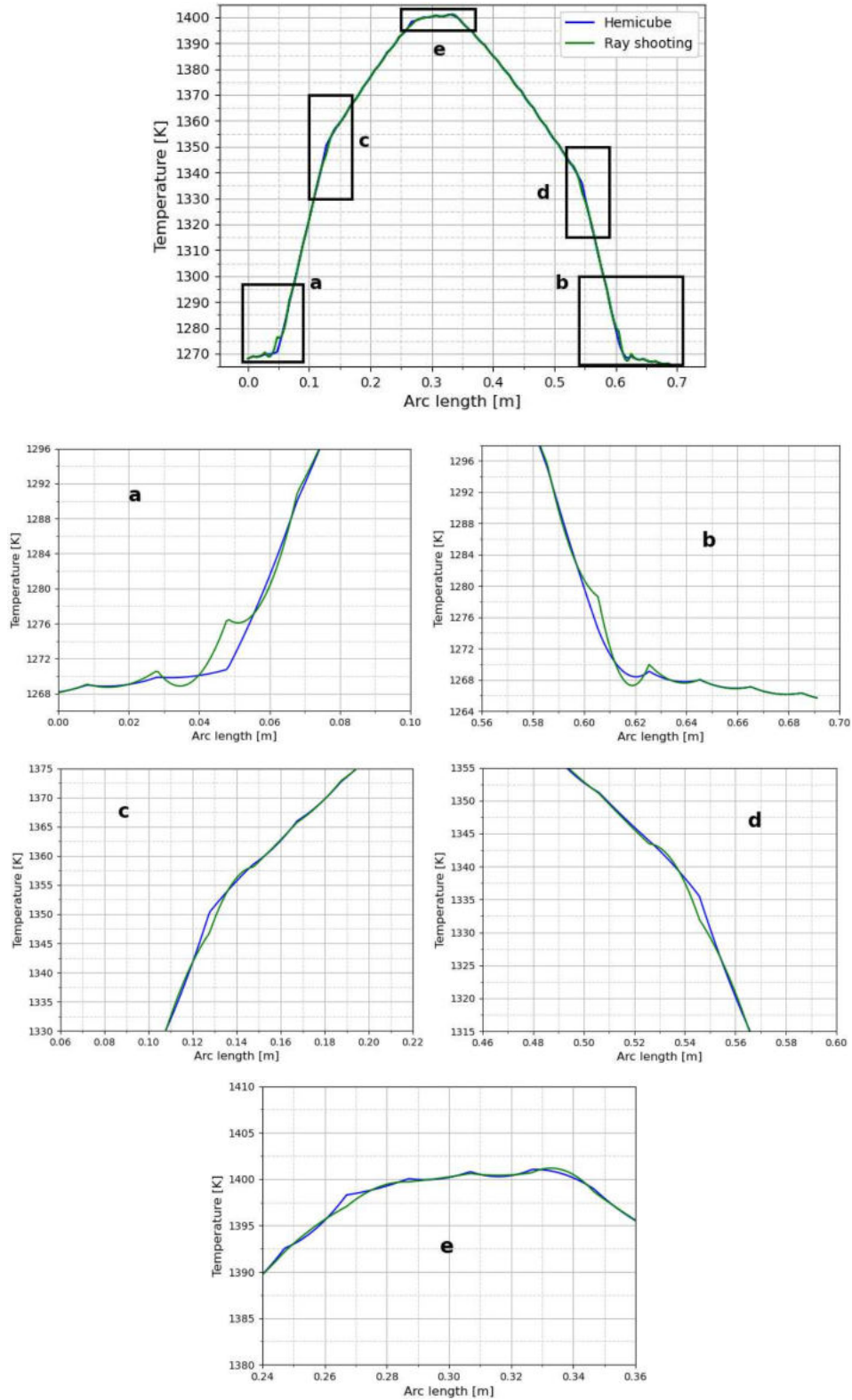
Figure 30. Zoom-in of temperature profile in the higher temperature region of cavity geometry.

The rest of the profile has no such significant differences between the models because the temperature does not change as fast as in the extrems. Therefore again, model differences might be caused by too coarsed mesh or insufficient convergence.

Now the influence of the cavity size will be tested. A cavity of 10mm is used, as shown in *Figure 31*. All the conditions are exactly the same as in the previous geometry, the only difference is the mesh in the smaller cavity. This mesh is depicted in *Figure 32*, which has 32618 elements.
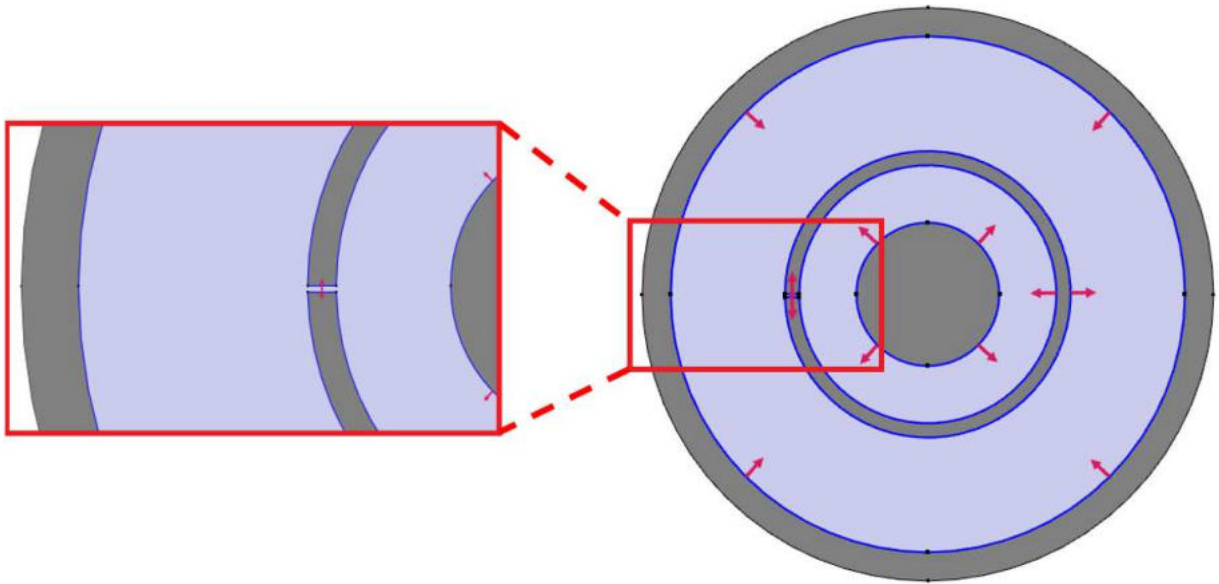
Figure 31. Geometry with 10mm cavity.

In this case, the simulation just considering conduction is skipped. Since the materials are the same and the geometry is almost identical to the previous one, the result does not change. The computational time for hemicube and ray shooting are 7s and 18s, respectively. These computational times are the same as in the previous geometry because both meshes have practically equal number of elements.
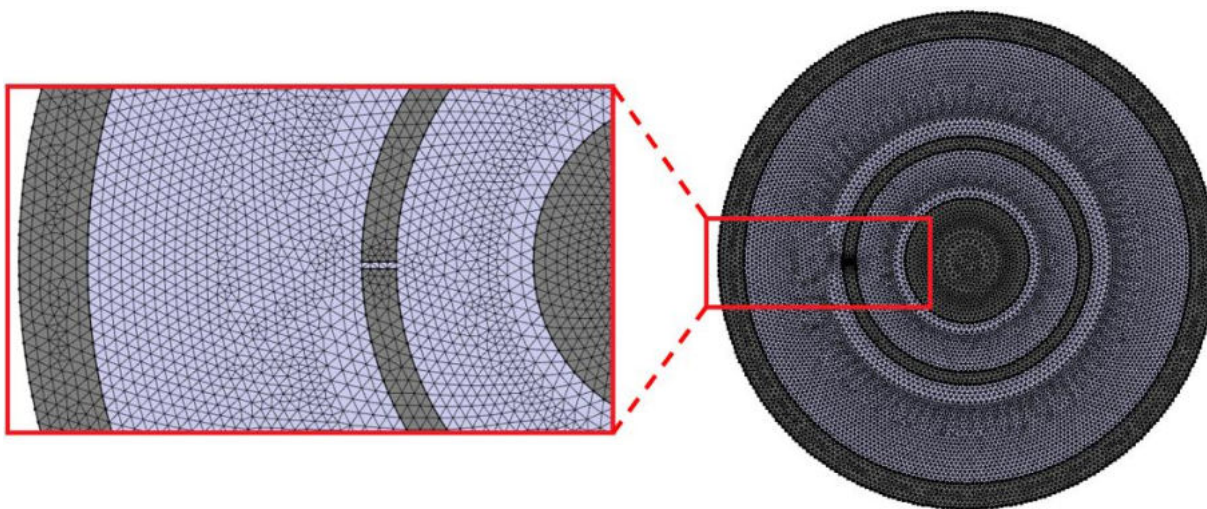
Figure 32. Mesh of the 10mm cavity geometry.

As seen in *Figure 33*, there are again temperature differences at specific spots in the cavity direction. Nonetheless, there are less difference spots and the difference is smaller than in the previous cavity geometry.

Similarly to the previous geometries, *Figure 34* shows the temperature profile considering 10mm cavity. As already mentioned, the temperature scale is lower. In this case, the highest temperature is around 1270K compared to 1400K for the previous larger cavity. Moreover, ray shooting is rougher than hemicube.
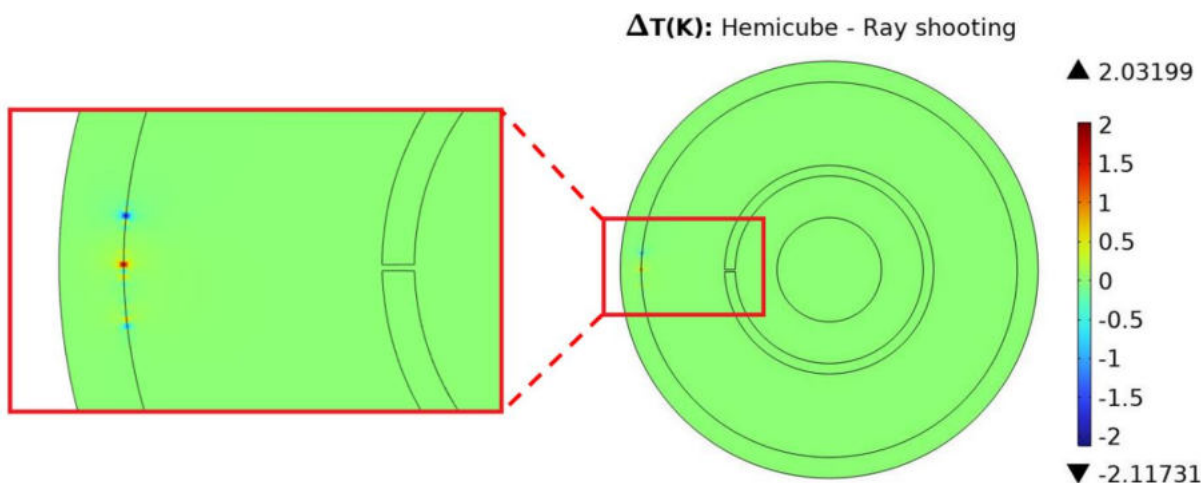
Figure 33. Temperature difference between radiation models for 10mm cavity.
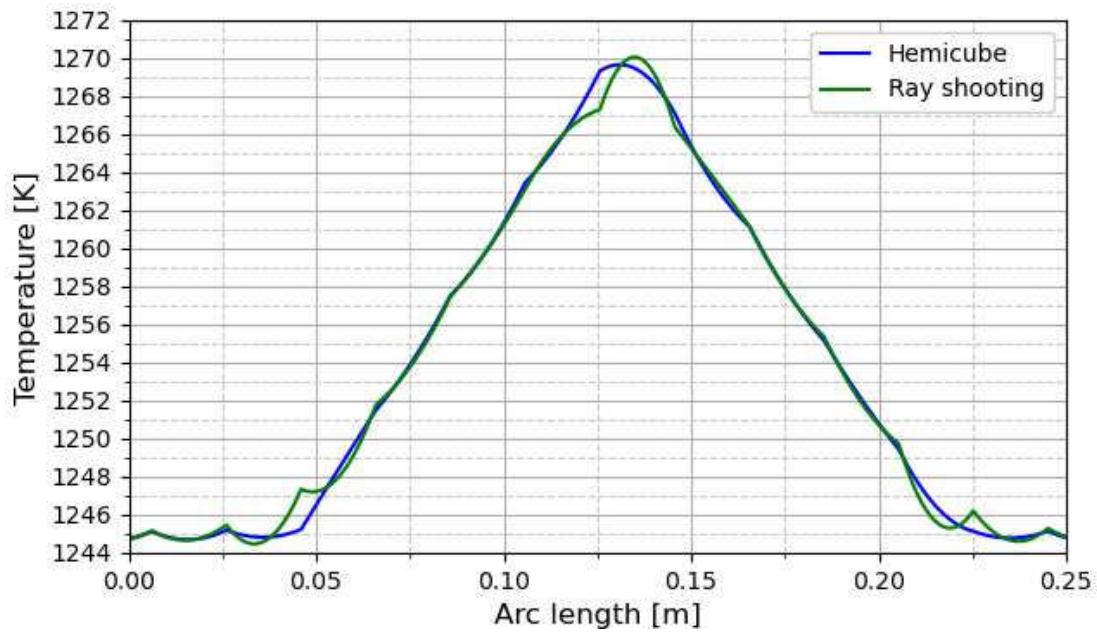
Figure 34. Temperature profile of the higher temperature region for 10mm cavity.

Considering block and cavity geometries, both models can resolve or take shadowing effect into account to a relative similar results. The main issue is the accuracy, specially when directionality or shadowing effect are more predominant (as in the cavity geometries). In such cases, temperature profiles are much rougher than simpler cases (as the block geometry), specially using ray shooting model. Hereafter, some parameters will be tested to check which one has stronger impact when getting accurate temperature profiles. The last geometry (10mm cavity) will be used to test these parameters.

Since the only hemicube parameter is the radiation resolution, only ray shooting parameters will be tested: maximum number of adaptations and tolerance. So far, the used maximum number of adaptations and Tolerance are 15 and 10^{-4}, respectively.

To test their influence, two more simulations are conducted: one using 20 as maximum number of adaptation and another using a tolerance of 10^{-8}. The new temperatures profiles will be compared to the original.

As seen in *Figure 35*, the impact of changing these parameters is minor. The difference between the original profile and those with the modified parameters is less than 0.1K. Furthermore, the temperature profile is still rough even with the modified parameters. Thus, these parameters are more focused on fine accuracy when having already a good solution. In this state, to get smooth profiles, changing the mesh might be a good solution.
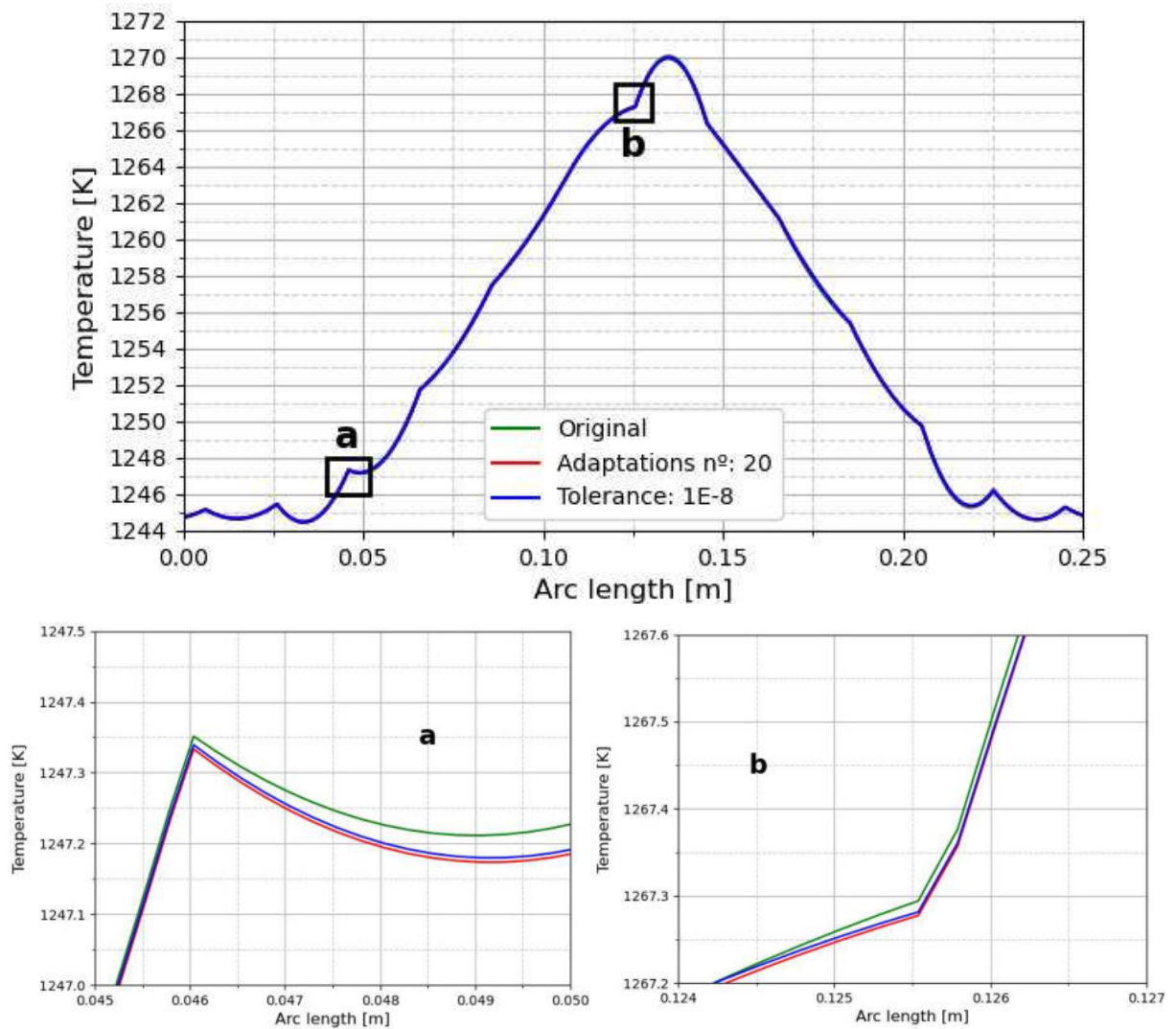
Figure 35. Temperature profile comparison when testing ray shooting parameters.

A new mesh is tested by increasing explicitly the number of nodes at the boundaries of the central circle (more radiating nodes) and at the boundaries of the inner surface of the outer cylinder (more and closer nodes for the incoming radiation). The described mesh is shown in *Figure 36* and it has 379382 elements, more than eleven times the number of elements of the original mesh. The computational time for hemicube and ray shooting are 1min 46s and 3min 34s, respectively.
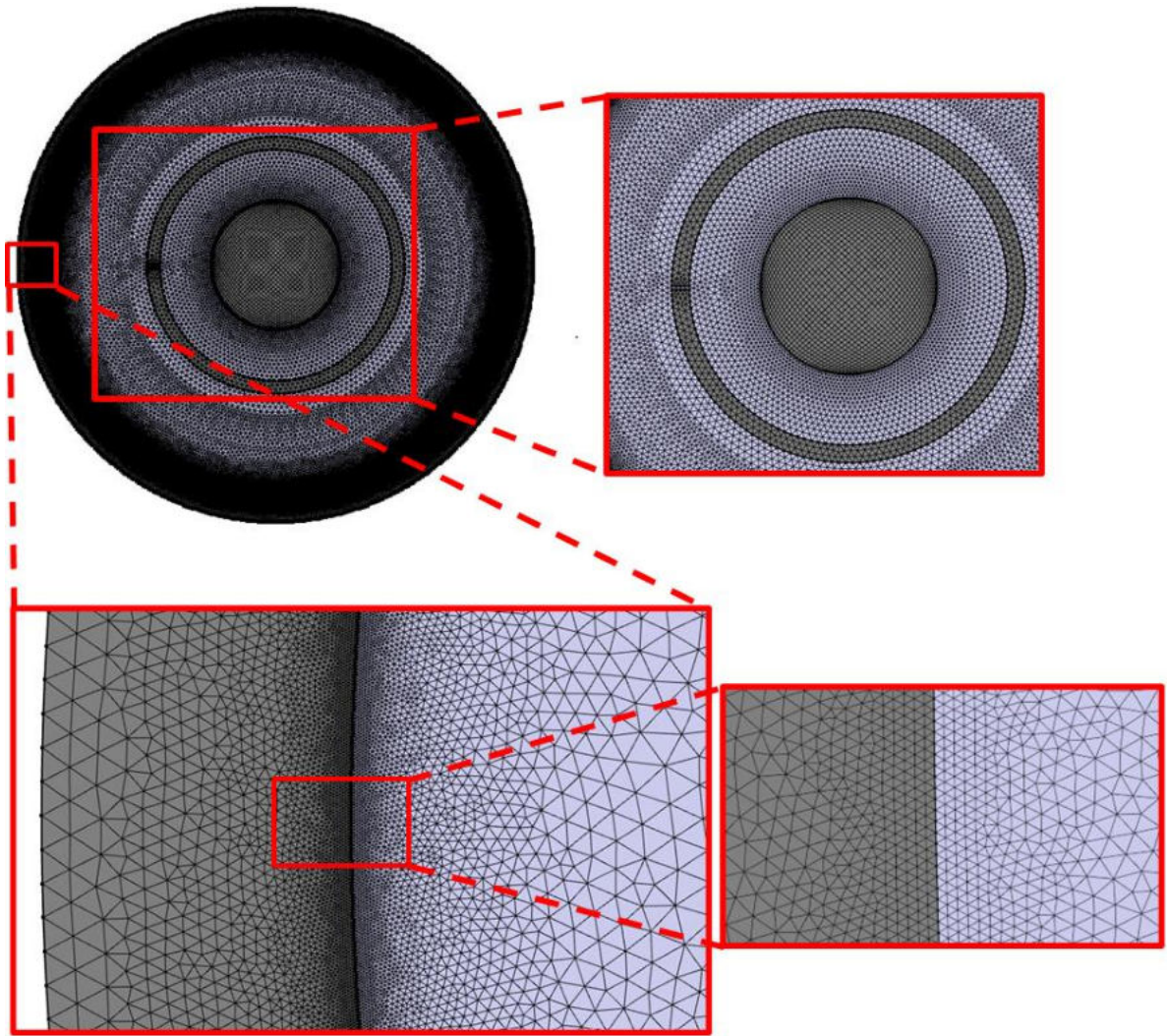
Figure 36. Denser mesh for the 10mm cavity geometry.

If temperature difference between radiation models is checked, depicted in *Figure 37*, it reduces by an order of magnitude compared to *Figure 33*. The number of specific spots where the temperature differs increased, having many more than in the original mesh, although temperature difference scale diminished by an order of magnitude. It went from approximately 2 K with the original mesh to 0.2 K with this denser mesh.

Checking the temperature profile of both radiation models using the denser mesh, which are in *Figure 39*, is very noticeable its smoothness compared to the previous mesh (*Figure 34*). Even in the extremes the temperature change is smooth. In this case, looking at the zoom-ins, the ray shooting has no appreciable fluctuations. Meanwhile, the hemicube profile fluctuates around the value of the ray shooting profile. These fluctuations are the reason for the many difference temperature spots in *Figure 37*.
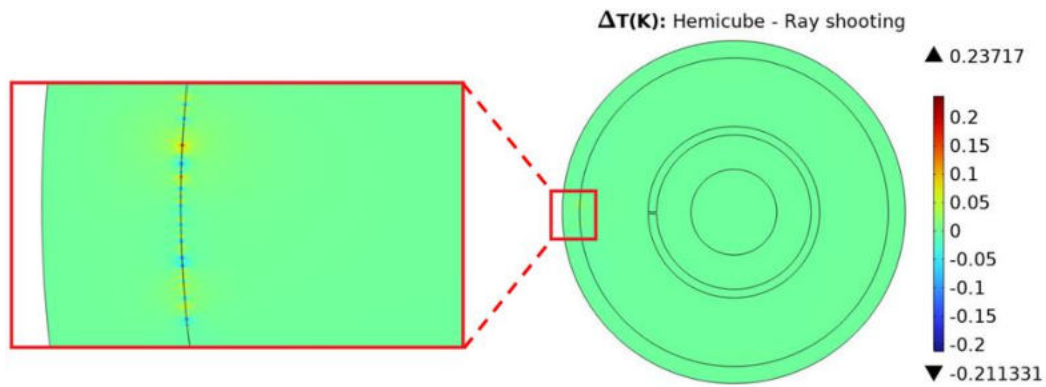
Figure 37. Temperature difference using the denser mesh in the 10mm cavity geometry.

Thus, the key factor to achieve reasonable temperature profiles considering S2S radiation is the mesh, specifically the number of nodes. For the hemicube method, having more nodes means there will be more subdivisions to account incoming radiation. Whereas for ray shooting, which resolves radiosity by comparing adjacent rays and adapting the number of rays shot, having more nodes means they are closer to each other. Thanks to that, the temperature or radiosity is not too different between adjacent nodes and the adaptation can be perform successfully. On the contrary, if the mesh is not dense enough, as in *Figure 25.b* and *Figure 32*, these properties are so different between adjacent nodes that adaptation cannot be fully performed by the given parameters. Thus, increasing the number of mesh nodes leads to a convergence. This is displayed in *Figure 38*, which shows the temperature difference between block and unblock surfaces for block and 10 mm cavity geometries (*Figure 18* and *Figure 31*). As mesh node number increases, the temperature difference value stabilizes and tends to a convergent value.
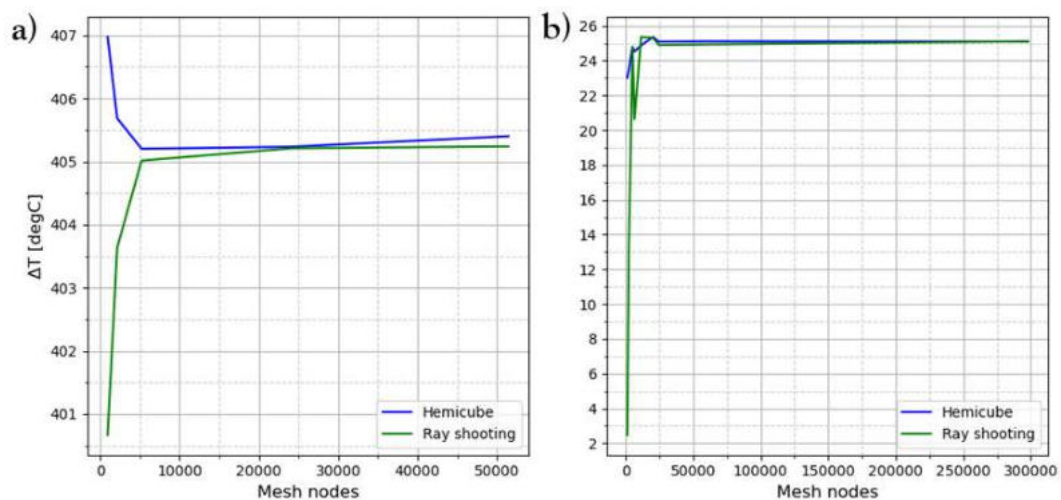
Figure 38. a) Temperature difference between unblock and block surfaces for block geometry. b) Temperature difference between cavity and upward directions for 10mm cavity geometry.
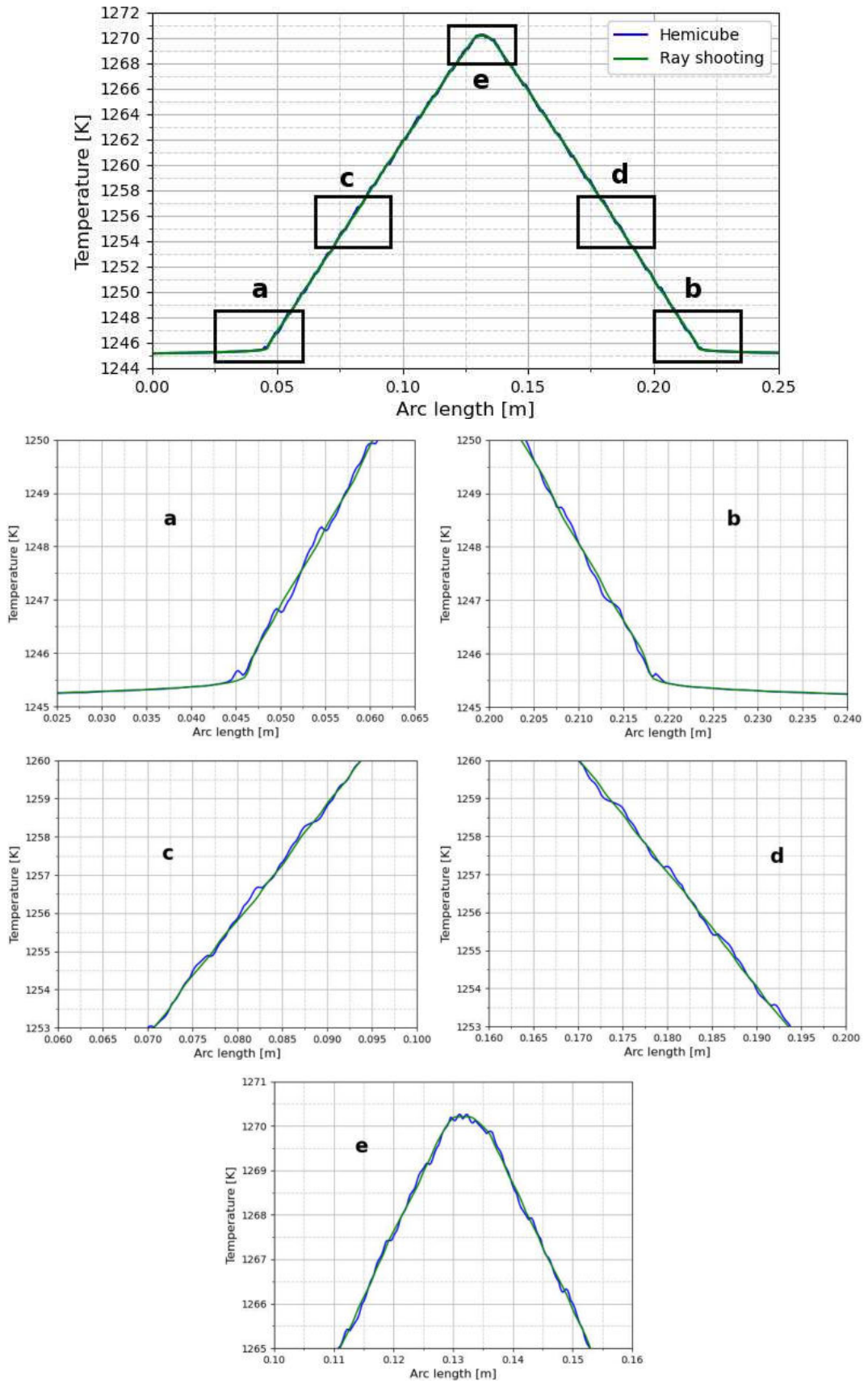
Figure 39. Zoom-in at the 10mm cavity temperature profiles with the denser mesh.

As first insight, both models include correctly shadowing effect as can be seen in the block and cavities examples, whereby there are a temperature decrease and a temperature increment, respectively. Nevertheless, there are discrepancies when comparing the models. They converge to fluctuating and non-smooth profiles, especially ray shooting model. It is necessary to use a dense mesh to get accurate and smooth temperature profiles, particularly where the temperature changes abruptly. Moreover, according to *Figure 39* ray shooting allegedly leads to more accurate results if the mesh nodes are enough. The rest of its parameters (tolerance and maximum number of adaptations) could be used to get finer accurate results once the first smooth result is reached.

4.1.2 Simple model of PVT reactor

A simple model of the PVT reactor is firstly used to test the radiation models in a more complex geometry than the previous toy models. *Figure 40a* reflects this simple geometry and the domains/materials are: silicon carbide (SiC), crucible, insulator, pedestal, coil (copper) and air. *Figure 40b* depicts the surfaces involve in the S2S radiation physics with red arrows. Their properties are listed in *Table 19*. SiC source and seed have both the same properties and the source is treated as a solid instead of a powder. The properties of the air domain are the same as *Table 3*. This model is a 2D axisymmetric geometry since the reactor has a cylindric geometry.
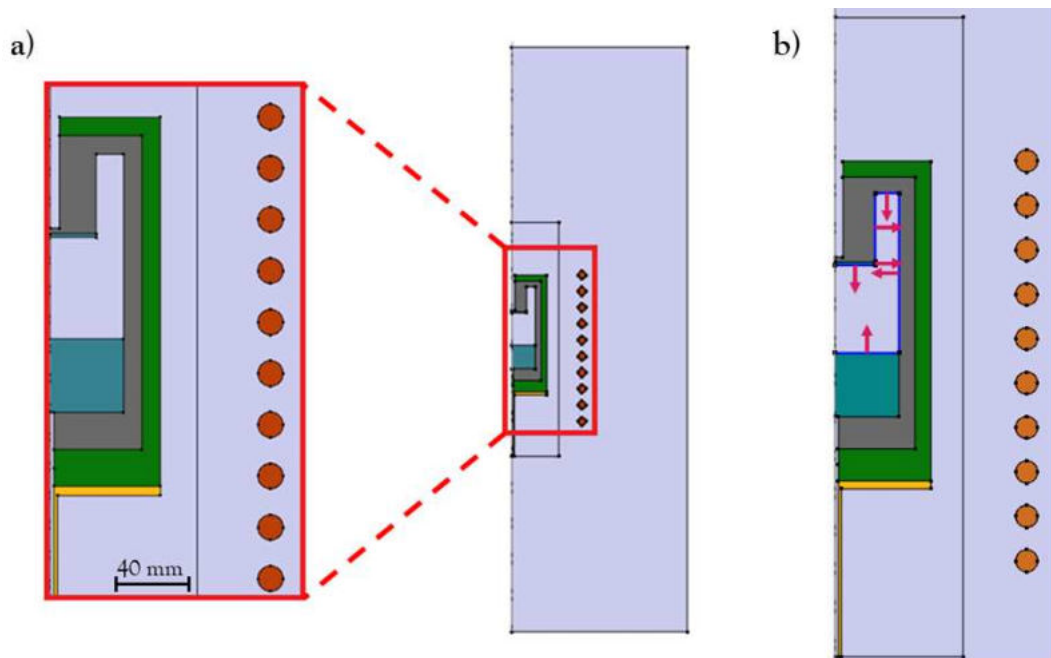
Figure 40. Geometry of a simple model of the PVT reactor [37].

Table 19. Material properties of the simple model reactor [37].

	SiC	Insulator	Pedestal
Density, ρ [kg/m^3]	3100	160	2260
Thermal conductivity, k [W/m·K]	$\dfrac{75000}{T}$	0.38	42
Heat capacity at constant pressure, Cp [J/kg·K]	1000	100	2050
Surface emissivity, ε	0.8	0.35	0.8
Electrical conductivity, σ [S/m]	1000	800	1
Relative permittivity, ε_r	1	3	1
Relative permeability, μ_r	1	1	1
Crucible			
Density, ρ [kg/m^3]	1820		
Thermal conductivity, k [W/m·K]	$-1.46\cdot10^{-8} T^3 + 7.97\cdot10^{-5} T^2 - 0.151T + 151$		
Heat capacity at constant pressure, Cp [J/kg·K]	$-5.72\cdot10^{-4}T^2 + 2.07T - 242$		
Surface emissivity, ε	0.8		
Electrical conductivity, σ [S/m]	3000		
Relative permittivity, ε_r	53		
Relative permeability, μ_r	3		
Coil (copper)			
See *Table 4*			

Figure 41 presents the mesh used for this simple geometry. It is constituted by 19290 elements, of which 12910 are forming the structured mesh in the reactor domains. As seen in the image, the surrounding is made of large elements to reduce computational time.
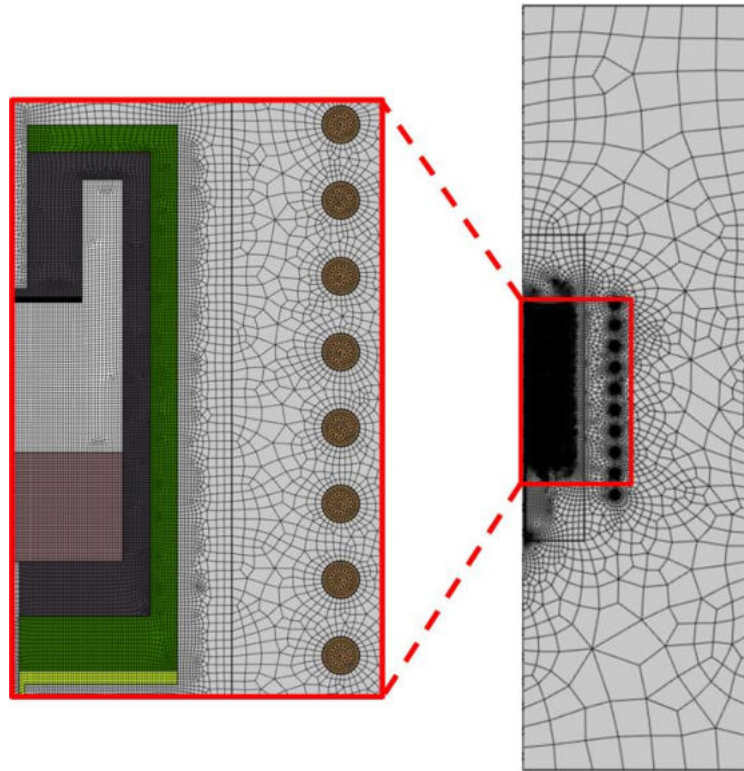
Figure 41. Mesh of the simple model reactor.

Simulations using both radiation models are conducted for different radiation resolutions: 32, 64, 128, 256, 512, 1024 and 2048. Their temperature values and temperature differences will be checked to see the effect of the radiation resolution. The coil current and frequency are set to 5100 A and 20 kHz, respectively. The temperature of the reactor chamber (boundaries between the reactor and the coil) is fixed at 300 K to simulate the cooling system.

Figure 42 depicts the temperature profiles for both radiation models using a radiation resolution of 2048 and the temperature difference. As seen, the profiles are slightly different, just a difference of 1.27 ºC. This difference is only present in the reactor, where the S2S radiation happens. Outside the reactor chamber, the difference is null, thus only the temperature profiles in the reactor itself are considered.

In addition, the temperature profile of the boundary marked in *Figure 43a* is plotted for both radiation models. In its zoom-in, these profiles are smooth and not rough as in the previous toy models examples. This is a possible indication that the mesh shown in *Figure 41* is good enough to solve correctly the S2S radiation physics.
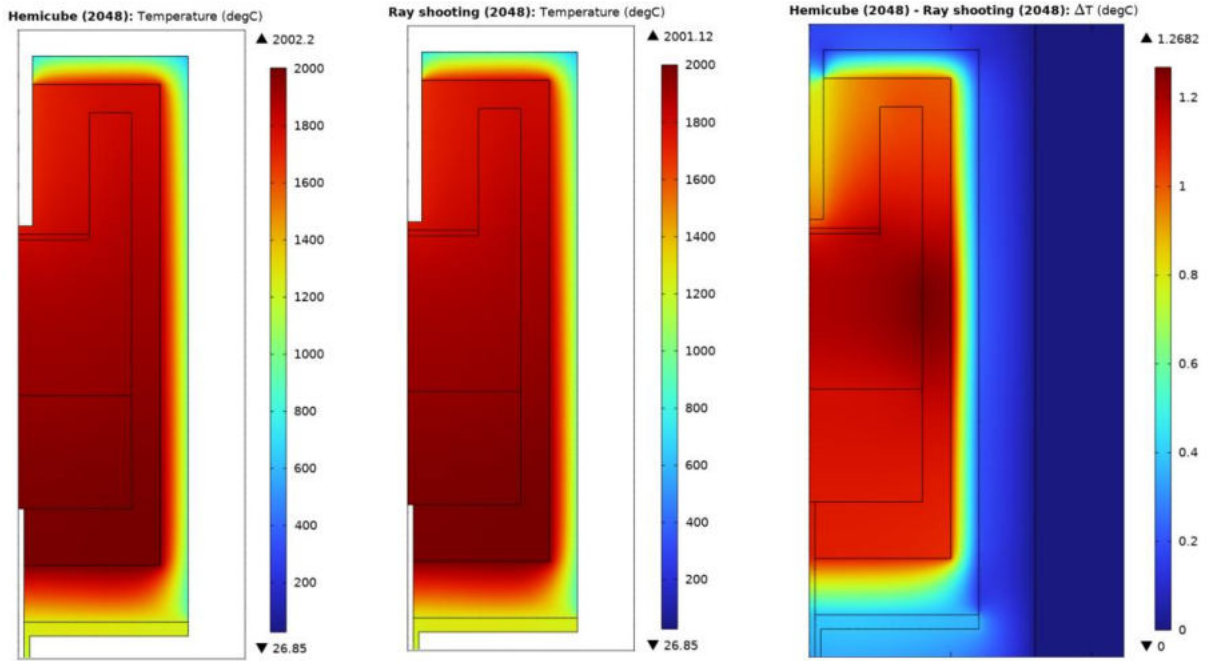
Figure 42. Temperature profiles of both radiation models and difference temperature.
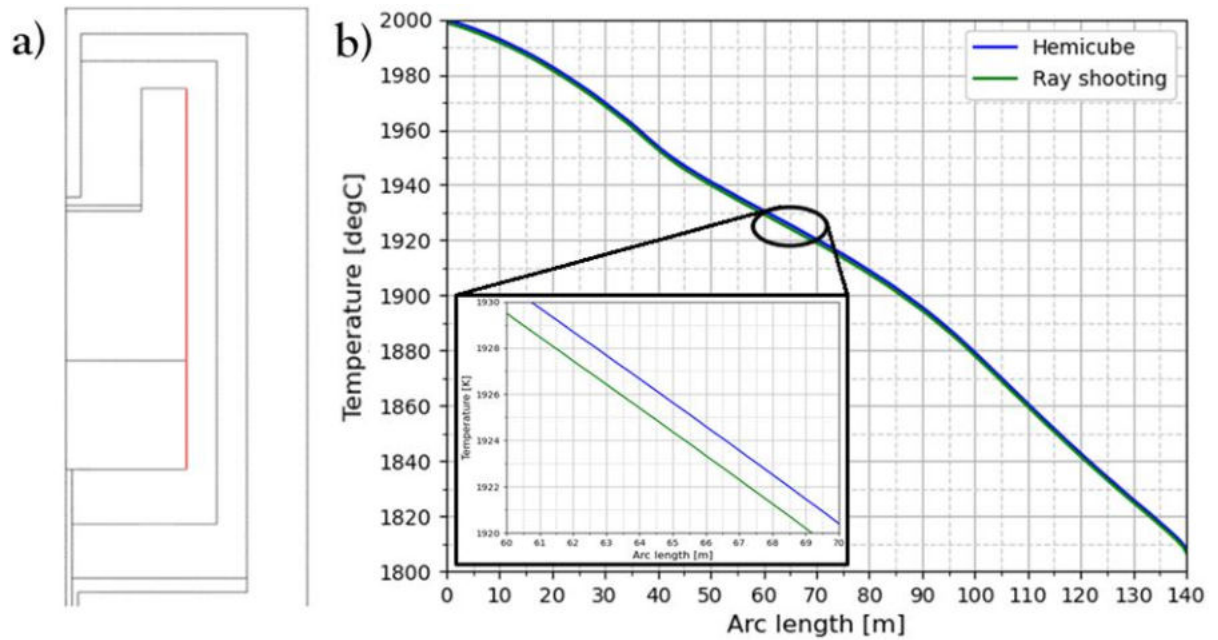
Figure 43. a) Boundary to be checked. b) Temperature profiles for hemicube and ray shooting.

Since the reactor chamber temperature is fixed at 300 K, the minimum temperature value for both models is the same. Nevertheless, the maximum temperature values are different, as can be seen for instance in *Figure 42* for a radiation resolution of 2048.
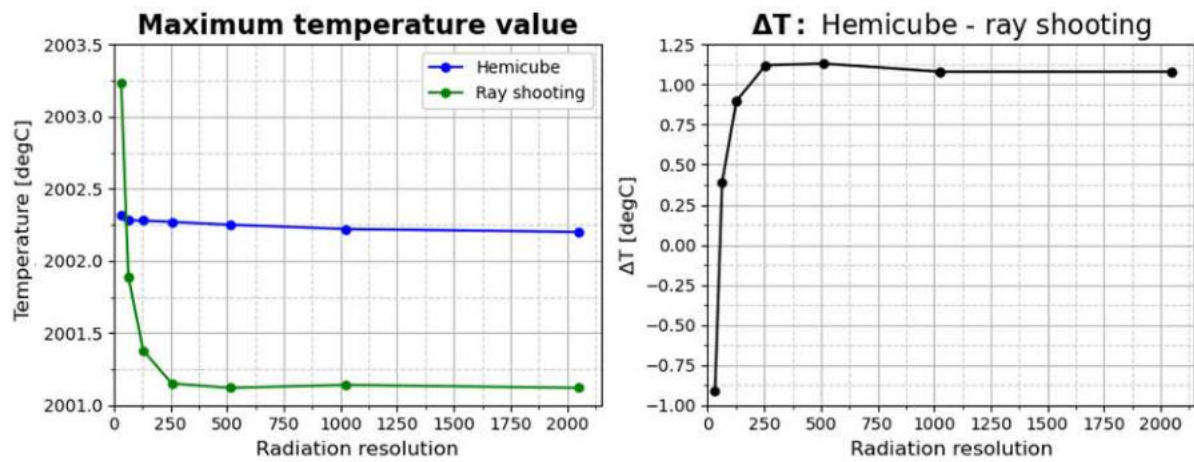
Figure 44. Maximum temperature values for both radiation models and their difference.

Figure 44 exposes these maximum temperature values and the difference for the radiation resolutions mentioned above. For hemicube, this value is approximately constant for all resolutions, being around 2002.3 ℃. On the other hand, for ray shooting it starts at higher values (2003.23 ℃) for a radiation resolution of 32 and as it increases it goes to a constant value, which is lower (2001.12 ℃) than the hemicube value.

Additionally, the mesh size effect is analysed in this simple model reactor. The temperature difference between hemicube results and ray shooting results using a radiation resolution of 512 is checked for different mesh node numbers. The impact of mesh size is displayed in *Figure 45*.
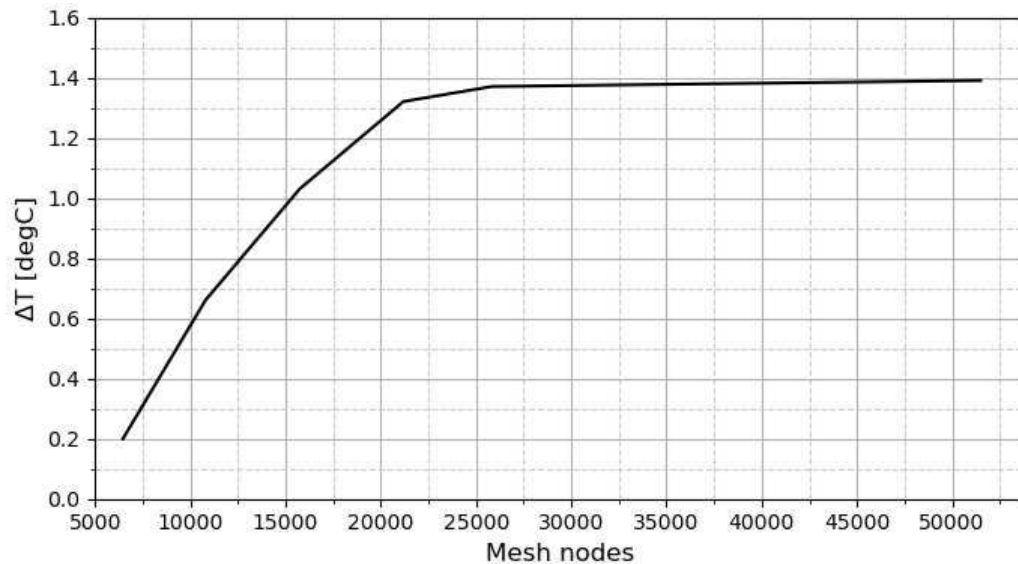
Figure 45. Temperature difference between radiation models using a radiation resolution of 512 in the simple reactor model for various mesh node numbers.

The chart shows the temperature difference $\Delta T = T(Hemicube) - T(Ray\ shooting)$. The difference is small for coarser meshes (low number of mesh nodes). But as the mesh gets denser, the difference becomes larger. Thus, apart from the radiation resolution, the mesh size also affects the temperature results.

As mentioned, in this geometry the S2S radiation is only present in the growth chamber and, due to its geometry, the shadowing effect is not very strong. But still, the radiation models lead to slightly different results. Firstly, the radiation resolution is tested. It exhibits more influence on the ray shooting model. In hemicube, the model simplifies the geometry into smaller surfaces and the resolution controls the number of these subdivisions. Having such a simple geometry, with almost no shadowing, a high resolution might not lead to a further convergence since the geometry is simple. Nevertheless, ray shooting accounts for the direct line-of-sight radiation between surfaces, considers the actual paths that radiation takes and it is based on adaptation between adjacent rays. The complex consideration of the geometry by reconstruction radiation path and the adaptation controlled by different parameters might allow achieving finer convergences or solutions. Therefore, it seems that owing to the apparently geometry oversimplification of the hemicube and the geometry complexity consideration of the ray shooting, they lead to different results even for such simple geometries.

The effect of the mesh size is briefly investigated. It also has an impact in the results as they start to differ more significantly as the mesh is finer. It seems this deviation tends to a constant value, meaning that regardless the mesh size, both models might never converge to the same result even for a simple model. This is further investigated in the following chapter using a more complex geometry.

4.1.3 PVT reactor

The radiation models are going to be tested in the actual reactor geometry shown in *Chapter 3.2*. Furthermore, the material properties, geometry conditions and solver settings from *Chapters 3.3, 3.4 and 3.5* are used. Regarding the mesh, firstly a mesh focused on the growth chamber and the SiC domains (source and seed) is tested. This means that it has more elements in those domains and it is structured as far as possible. This is shown in *Figure 46*, where the surrounding has a coarse mesh because there is no interest in this area (just heat conduction through air) and to reduce computational time. In contrast, the SiC source mesh is formed by a structured quadrilateral mesh and there are plenty of mesh elements around the SiC seed to solve finely the S2S radiation on this thin domain.
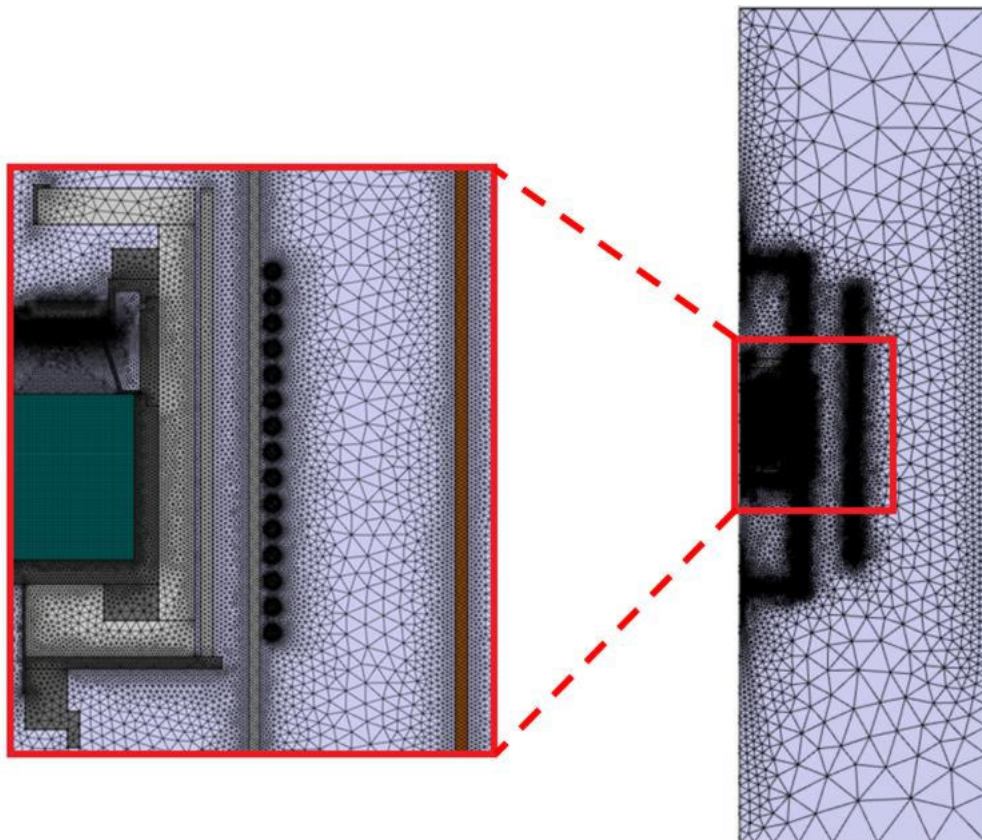
Figure 46. First mesh used in the PVT reactor.

In case of hemicube model, all its possible radiation resolutions are tested: 32, 64, 128, 256, 512, 1024, 2048 and 4096. For ray shooting, also all its possible radiation resolutions, except the highest one (4096), are tested: 4, 8, 16, 32, 64, 128, 256, 512, 1024 and 2048. The highest one is not included owing to its extremely large computational time. Related to the other parameters

of the ray shooting model: tolerance, maximum number of adaptations and maximal number of reflections are set to 10^{-4}, 15 and 1000, respectively. It is important to note that for the maximum temperature value only the reactor will be considered because this is where the highest temperatures occur, while for the temperature differences the whole geometry will be considered due to the impossibility of COMSOL Multiphysics to select specific domains when doing comparisons and additionally because for some cases the highest difference are not within the reactor itself. This is demonstrated for instance in *Figure 47*, showing the temperature in the reactor for both radiation models and its temperature difference, where the highest differences are outside the reactor, in this case, in the upper air domain between the crucible and the isolation and below the crucible as well.
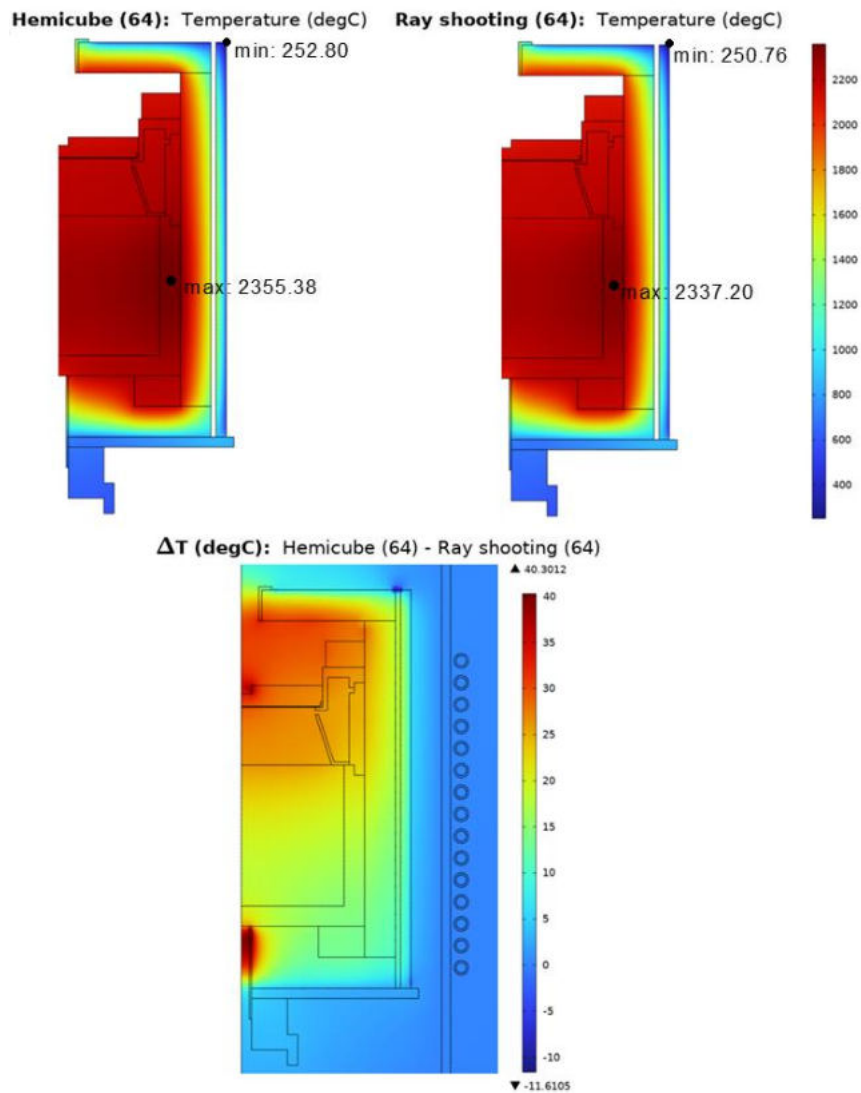
Figure 47. Temperatures in the reactor for both radiation models with a radiation resolution of 64 and the difference in the whole geometry.

Checking the highest temperature values for the radiation resolutions mentioned above, the behaviour reflected in *Figure 48.a* is obtained. Regarding hemicube, it has a highest temperature value of 2353.28 °C for a radiation resolution of 32 and it grows up to 2364.33 °C for a resolution of 4096. The temperature change seems to be constant, increasing around 2 °C as radiation resolution increments. In relation to ray shooting, it starts with a value of 2302.60 °C for a resolution of 4 and goes to 2299.47 °C for a resolution of 2048. It leads to a constant value as the radiation resolution increases, for instance the values for resolutions of 256, 512 and 1024 are 2299.43 °C, 2299.47 °C and 2299.46 °C, respectively. Nonetheless, there is a strong fluctuation in low resolutions, ranging from 2300.61 °C to 2349.68 °C between resolutions from 4 to 128.
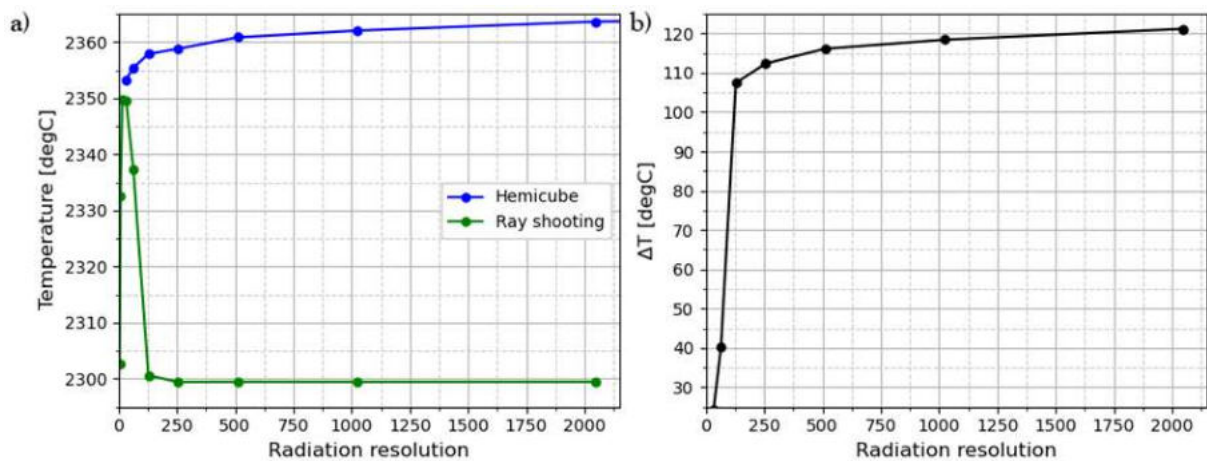
Figure 48. a) Highest temperature values for both radiation models in the PVT reactor. b) Temperature difference between radiation models in the PVT reactor.

Regarding temperature difference between the radiation models, it is demonstrated that it is noticeably high as in *Figure 48b*. The tested radiation resolutions for these differences are 32, 64, 128, 256, 1024 and 2048. They go from 24.29 °C to 121.16 °C, meaning that the temperature using hemicube is significantly higher with the respect to ray shooting. This is also depicted in *Figure 48a*, where hemicube highest temperature value rise does not stop, while ray shooting model decreases and tends to a constant value.

As mentioned in *Chapter 2.2*, the gradient temperature between the source and the seed is the driving force for the PVT growth process. In addition, temperature difference along the seed is also a key factor to control the surface profile of the growing boule and the density of defects. *Figure 49* shows both temperature differences for both models using various resolutions:

Figure 49.a depicts the difference between the highest temperature in the source and the lowest temperature at surface seed, *Figure 49b* reflects the temperature difference between the highest temperature point at seed surface (extreme) and the lowest temperature point (center). Both cases follow the same tendency, hemicube changes slowly apparently leading to a constant value as radiation increases. Meanwhile, ray shooting starts at a lower value than hemicube, but it grows abruptly up to a constant value reached at a resolution of 256.
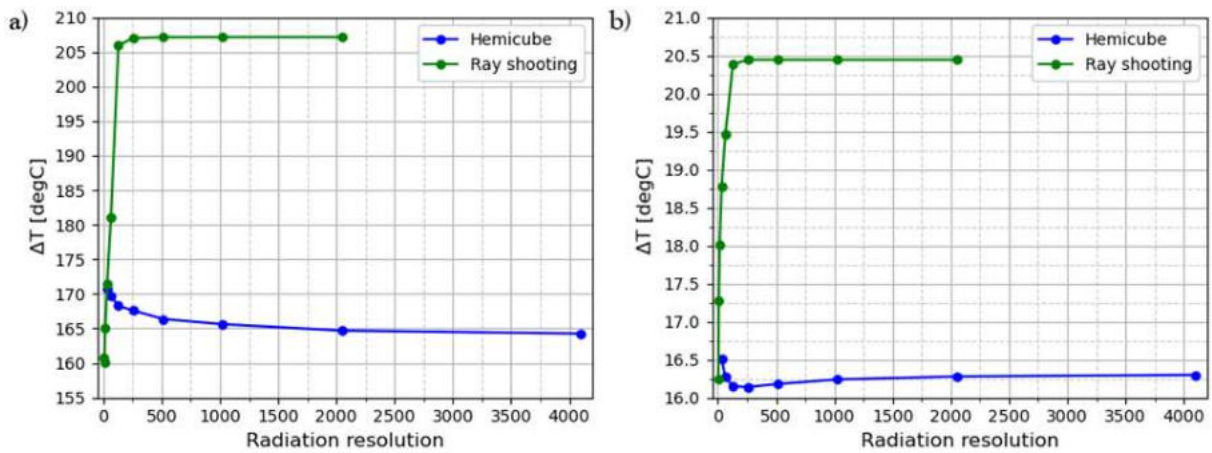
Figure 49. a) Temperature difference between hot source and colder seed. b) Temperature difference at the seed surface.

The effect of the radiation resolution is similar to *Figure 48a*. For hemicube case, as radiation resolution increases, the temperature changes slowly. In contrast, ray shooting is strongly affected by this change at low resolution, but from 256 onwards it stabilizes at a constant value.

Therefore, according to *Figure 48*, both models are affected by the resolution. If hemicube is used, it is affected regardless of the resolution. The temperature constantly increases or decreases leading apparently to a constant value, but it seems this is not reached. At the same time, ray shooting is greatly affected by the change at low resolutions. As this resolution grows, the temperature reaches a constant value normally at a radiation resolution of 256. Thus, increasing the resolution beyond 256 has no significant effect for this model. Moreover, hemicube results converge to higher temperatures than ray shooting.

The further surface discretization done by hemicube model due to radiation resolution increment helps capturing finer details of thermal radiation, leading to the slight changes in temperature when radiation resolution is modified. Ray shooting relies on ray tracing and its adaptation, which greatly considers the geometry complexity and shadowing effect. For low resolution, the low quantity of shot rays might oversimplify the radiative heat transfer, causing temperature

fluctuations. Despite this, increasing the resolution, and thus the number of shot rays, is enough to successfully converge the solution even for the complex geometry and the shadowing effect. Therefore, a radiation resolution of 256 may be a threshold for proper results for ray shooting case. This could be one of the reasons why this model gives higher temperature differences in *Figure 49*. Ray shooting would be able to capture finer details in the temperature profile and in temperature differences, resulting into higher differences than hemicube. An additional important factor to take into account is the computational time, which is shown in *Figure 50*. As seen, ray shooting is much more demanding than hemicube, especially for high resolutions. This may be caused by the geometry complexity and shadowing effect consideration and because of the ray tracing process. Thus, instead of choosing the highest resolution for any model, an intermediate resolution could be selected trying to find an equilibrium between accuracy and computational effort. Additionally, *Figure 51* shows the profiles of the temperature difference between radiation models for different resolutions. These profiles are the ones used for representing *Figure 48b*. It depicts the largest temperature deviation is in the air domain between the upper crucible part and the insulation. Hence, a denser mesh will be tested to check if this difference becomes greater or reduces.
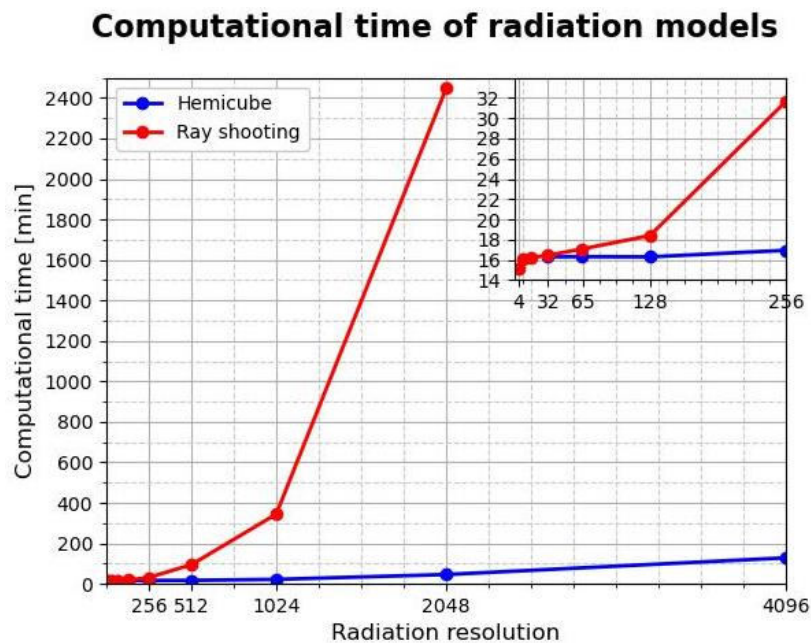
Figure 50. Computational time of radiation models for different resolutions.
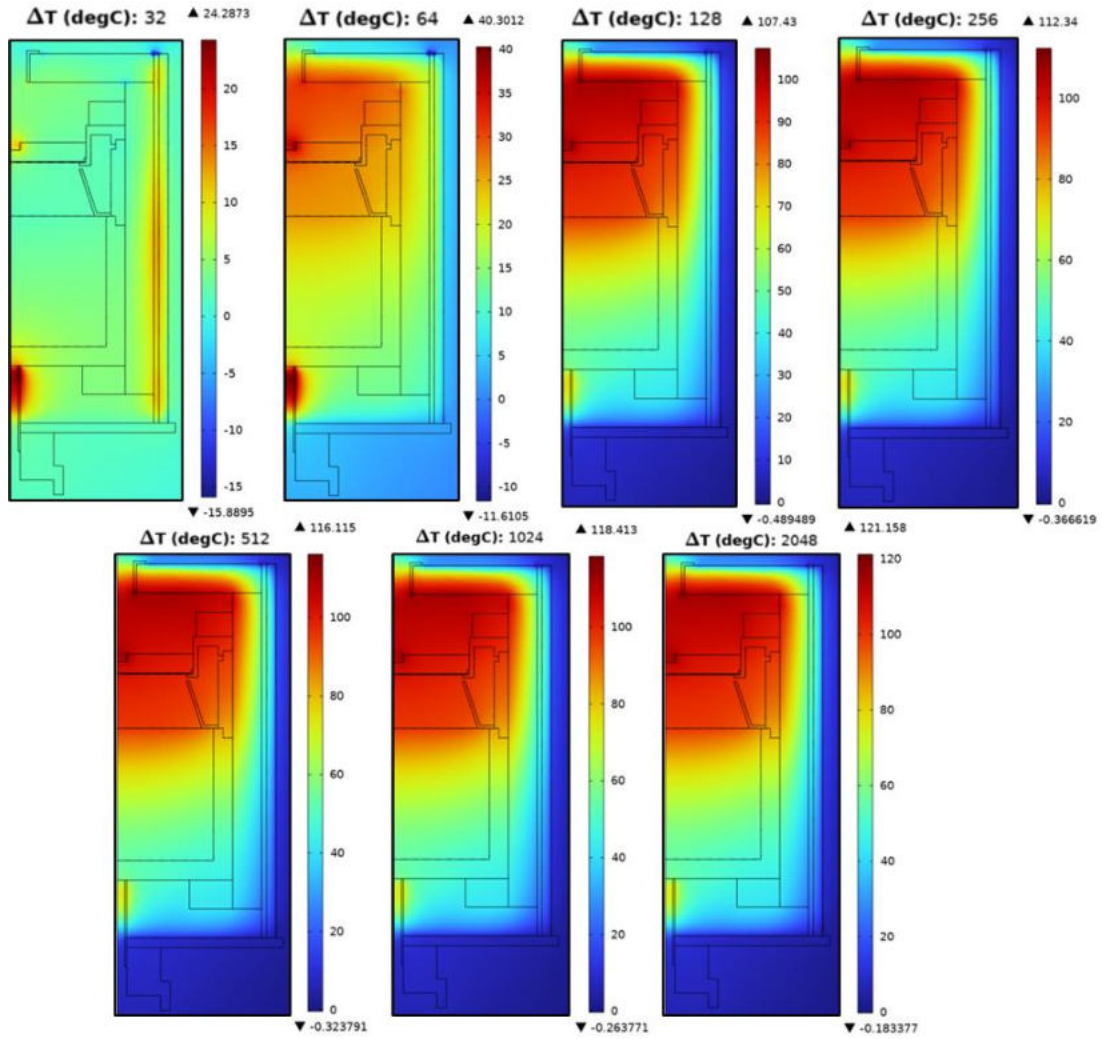
Figure 51. Temperature difference profiles for different resolutions.

The new mesh is based on modifications in the reactor domains, specially where the temperature difference depicted in *Figure 51* is the highest. This denser mesh is shown in *Figure 52*: the mesh element number in the reactor domains was increased, trying to get a structured mesh as long as possible. The mesh in the air domain of the growth chamber is reduced in order to reduce some computational effort, although the edge elements at the surfaces increased to resolve better S2S physics. Additionally, the mesh elements were greatly increased in the air domain above crucible and below insulation, where the temperature difference was the largest. Mesh element number went from 25505 elements in the initial mesh (*Figure 46*) to 48989 elements for this new denser mesh.
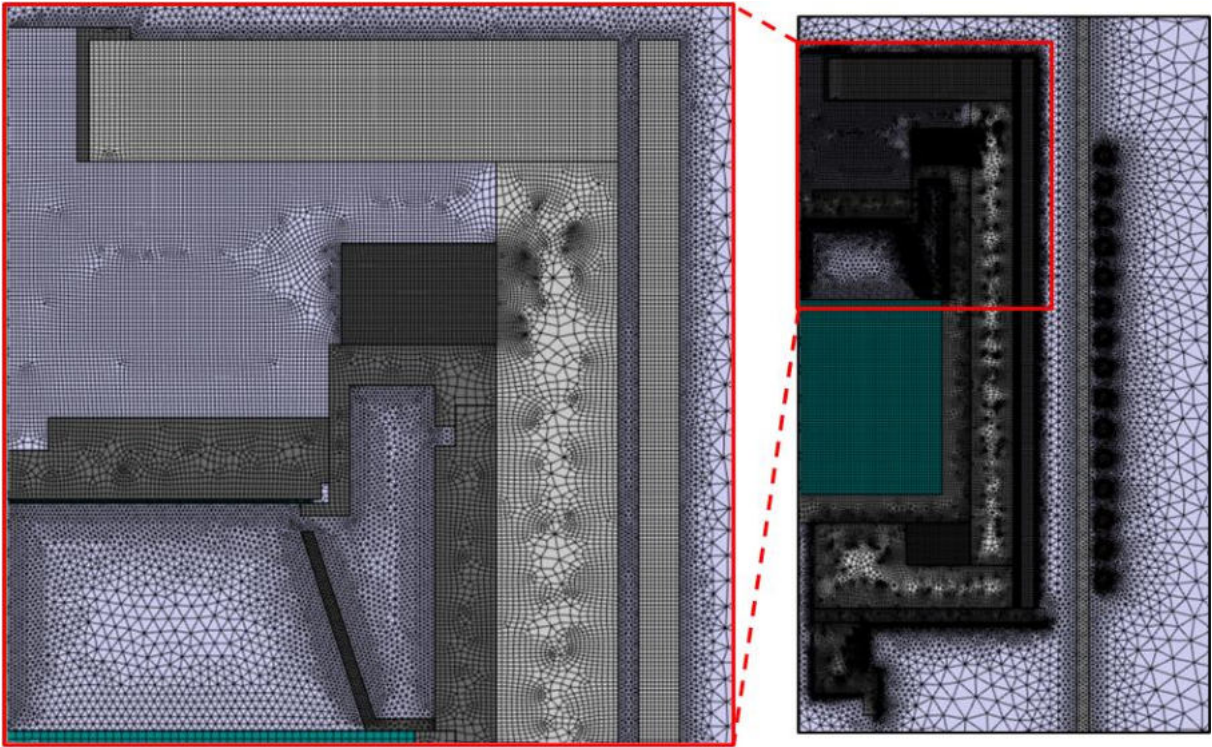
Figure 52. Denser mesh for the B-geometry reactor.

Using this new mesh, the same temperature profiles and differences for the same radiation resolutions as previously are checked. *Figure 53a* reflects the highest temperature value behaviour. The tendency is the same as using the previous mesh (*Figure 48a*): for hemicube, it increases slowly, while for ray shooting, it decreases abruptly, reaching a constant value. Nevertheless, using a denser mesh, the absolute values changed: hemicube goes from a range of 2353-2364 ℃ to a range of 2373-2380 ℃, ray shooting goes from 2350-2300 ℃ to 2325-2240 ℃. Thus, hemicube tends to higher temperatures and ray shooting to lower ones.
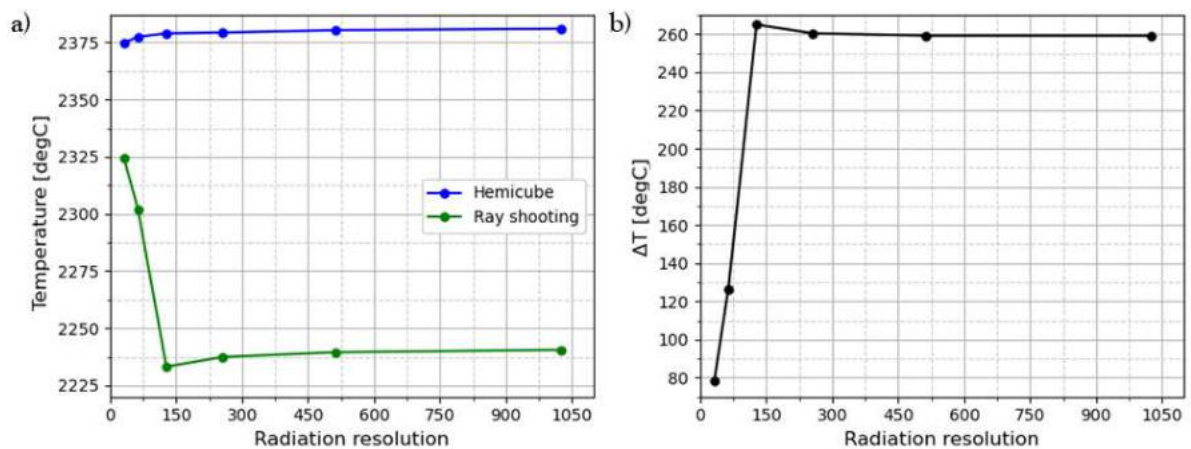
Figure 53. a) Highest temperature values for PVT reactor geometry using a denser mesh. b) Temperature difference between radiation models using a denser mesh.

This is supported by the temperature difference considering the whole geometry, shown in *Figure 53b*. In this case, it is much more significant when using the coarser mesh (*Figure 48b*), rising to 260 °C. These values are doubled compared to the previous case. As in *Figure 49*, temperature difference between source and seed and the temperature difference along the seed surface are depicted in *Figure 54* for this denser mesh. Once more, they behave as in the previous case (*Figure 49*), but the values are different. For hemicube case, it results in lower gradients, while for ray shooting it leads to higher values.
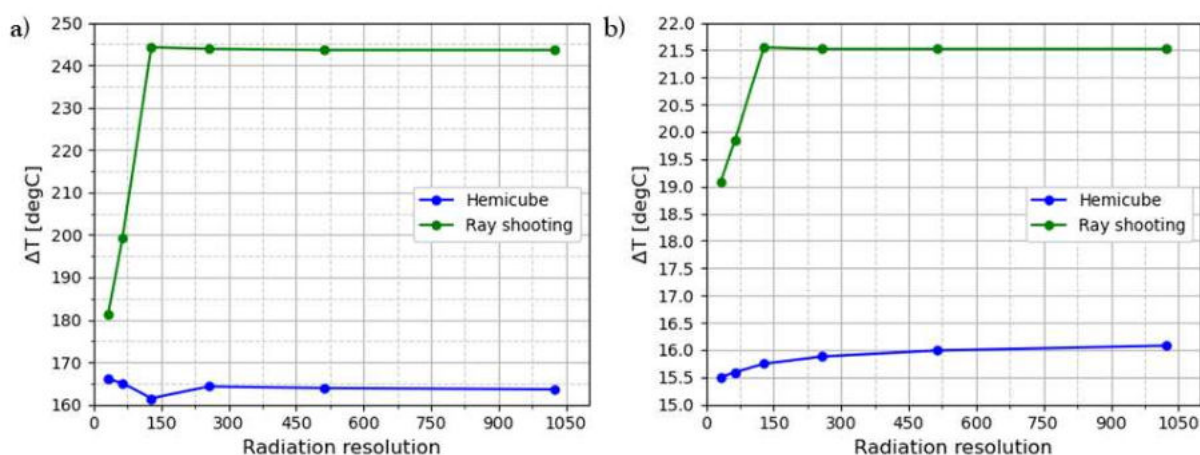
Figure 54. Dense mesh: a) Temperature difference between hot source and colder seed. b) Temperature difference at the seed surface.

Hence, mesh properties have a strong impact in the resulting temperature profiles and gradients. As the mesh becomes denser in the areas where S2S radiation is important, the results change significantly. These changes are not in the behaviour, but in the numerical values. Hemicube moves towards higher temperatures, while ray shooting does the opposite. Regarding temperature difference, ray shooting results into higher temperature differences than hemicube. Nonetheless, the numerical value change is significantly higher for ray shooting than hemicube, which just differs in some degree. For that reason, the temperature difference depends sensitively on mesh size.

These outcomes might be due to the apparent oversimplification of the hemicube model and the adaptation and ray tracing of ray shooting. Hemicube overestimates the values because of the lack of geometry complexity considerations and treating the shadowing effect by means of *z*-buffering. On the other hand, ray shooting can take all of this into account through ray tracing, which produces lower temperatures. This fact also affects the gradients. All the considerations of ray

shooting help to encompass finer details and changes in the temperature profile, resulting in higher temperature differences than using hemicube.

In conclusion, direct area integration model is directly discarded as a consequence of its simplicity. Considering hemicube and ray shooting, the mesh density is the most important point to get proper temperature profiles, especially when shadowing effect has a strong influence, as in the toy models. The other key factor is the radiation resolution, which allows better convergences. As a result, the numerical value of the temperature profile change depending on this resolution. While for hemicube it grows constantly to a constant value, ray shooting decreases and reaches a constant value at medium resolutions. One of the potential reasons for that is the oversimplification of the hemicube model, causing an overprediction of the temperature value. At the same time, ray shooting considers geometry complexity, thermal path and shadowing effect by ray tracing, which allows finer details and accuracy at expense of higher computational times. This fact leads more accurate temperature gradients.

According to *Steiner, Tyler R. [24]*, hemicube and ray shooting were compared to experimental results. Ray shooting results were closer to the experimental four out of five times. This is an additional indication that ray shooting is a more accurate model than hemicube. This is investigated in *Chapter 4.2* by comparing FEM simulations with experimental data.

Additionally, another potential reason for the discrepancy between radiation models might be the treatment of the outermost surfaces of the reactor. In *Chapter 4.1.2*, in the simple model of PVT reactor, these outermost surfaces are not included in the S2S physics, but as surface-to-ambient (*Figure 40b*). In this case, the difference between radiation models is small ($\approx$1.26 ºC). On the other hand, in the realistic model, the outermost surfaces are included in the S2S physics (*Figure 13*). In this case, some outermost surfaces are involved in the S2S radiation (such as the surfaces in the gap between the upper part of the crucible and the insulator), but other might be treated as surface-to-ambient. Thus, it may be necessary to modify which surfaces are included in the S2S physics. For this reason, further investigations would be useful to check which surfaces are truly participating in S2S physics and see the effect on the radiation model discrepancy.

4.2 Validation

To fully check which radiation model is more suitable to consider radiative heat transfer during PVT growth process, FEM simulations are compared to experimental measurements of an actual PVT reactor. The measurements are conducted with an empty crucible, neither source nor seed were in the reactor during the thermal testing in order to avoid inaccuracies owing to the porosity of the SiC powder and mass transport. So far, no mass transport was considered and the source was treated as a solid (*See ending of Chapter 2.2*).

For thermal testing, two pyrometers are used on the crucible. One is set to quantify the temperature on crucible top, while the other is for the bottom part as reflected in *Figure 55* where the red arrows expose the pyrometers pointing.
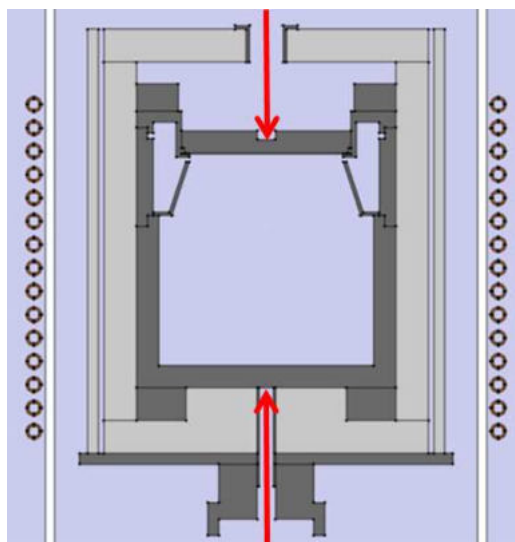
Figure 55. Pyrometer configuration for thermal testing of the B-geometry reactor.

Two experimental tests are conducted: in the first run (*ID: F_G8_B_1_2*) the power is increased until a constant temperature of 1900 ℃ is reached. Hereafter, the power is changed to maintain this temperature while the pressure is reduced to vacuum. Finally, the temperature is measured at different coil positions. Regarding the other run (*ID: FaV1_G8_B_1*), again the power is modified to maintain the temperature constant while the pressure decreases. Once the vacuum is reached, power is increased in steps until the temperature reaches 2000 ℃. Then, this gradual power increment is done for another coil position. As seen in *Figure 56*, the dots marked in the charts are the states used for the validation. They were selected after the power and the pressure stabilizes. Therefore, they are treated as steady states.
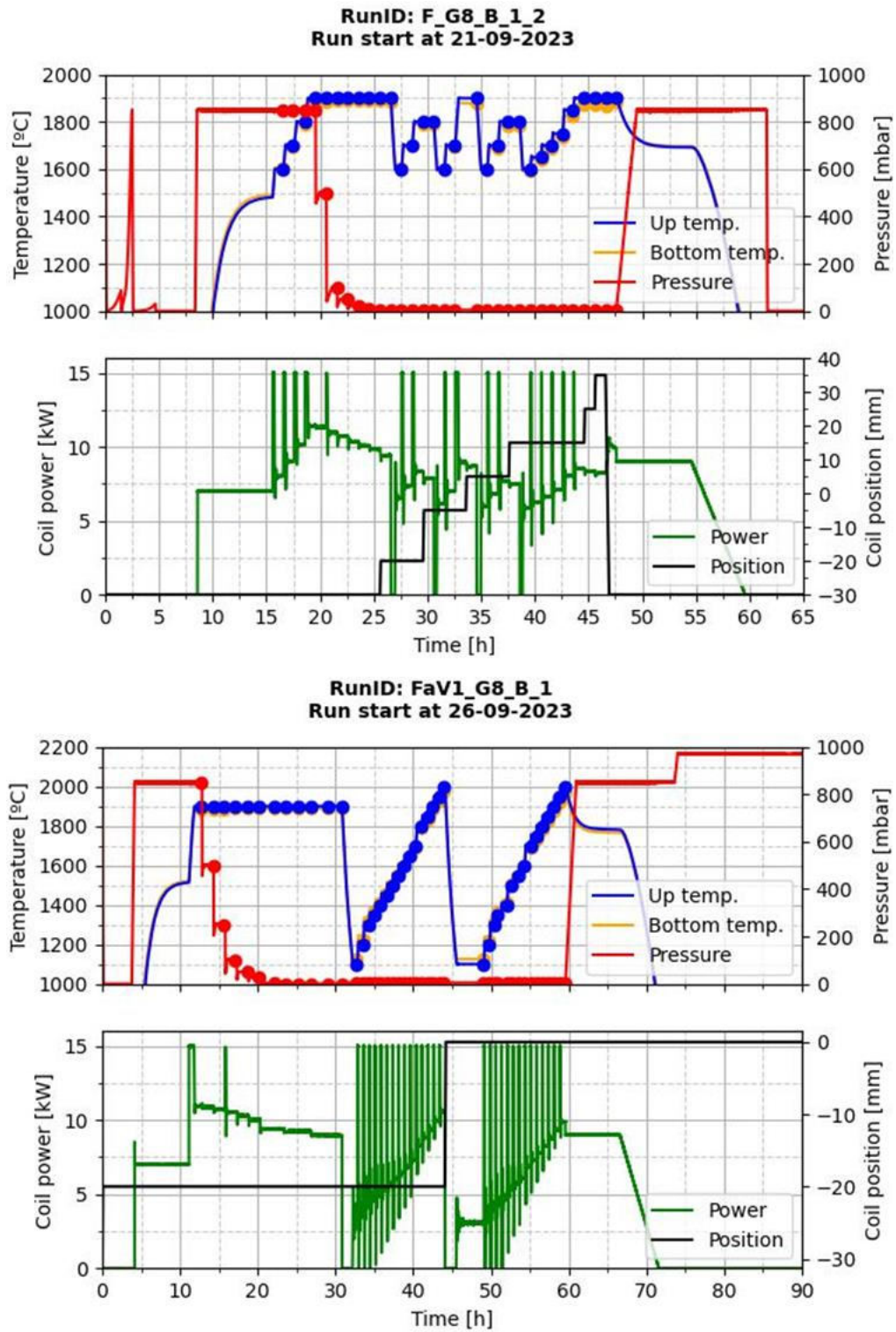
Figure 56. Experimental tests in the actual B-geometry crucible.

Table 20. Selected states for validation from the run F_G8_B1_2.

	F_G8_B_1_2				
	Power [kW]	Position [mm]	Pressure [mbar]	Up temp. [degC]	Bottom temp. [degC]
0	8.03	-30.00	849.90	1600.00	1603.84
1	9.05	-30.00	848.80	1699.99	1696.72
2	10.18	-30.00	849.05	1800.00	1790.06
3	11.43	-30.00	849.38	1899.99	1883.50
4	11.35	-30.00	500.02	1900.00	1883.46
5	10.97	-30.00	100.00	1900.01	1890.59
6	10.73	-30.00	50.00	1900.00	1890.43
7	10.38	-30.00	20.00	1900.00	1890.19
8	10.10	-30.00	10.00	1900.00	1889.96
9	9.84	-30.00	5.00	1900.01	1889.86
10	9.45	-20.00	5.00	1900.00	1885.91
11	6.51	-20.00	5.00	1600.01	1603.24
12	7.36	-20.00	5.00	1700.00	1697.68
13	8.33	-20.00	5.00	1799.99	1791.95
14	7.90	-5.00	5.00	1799.99	1787.18
15	6.17	-5.00	5.00	1600.00	1600.00
16	7.00	-5.00	5.00	1700.00	1693.07
17	8.98	-5.00	5.00	1900.00	1879.93
18	8.72	5.00	5.00	1899.99	1876.68
19	5.99	5.00	5.00	1599.99	1597.88
20	6.81	5.00	5.00	1700.01	1690.43
21	7.71	5.00	5.00	1799.99	1783.33
22	7.52	15.00	5.00	1799.99	1780.84
23	5.85	15.00	5.00	1599.99	1595.58
24	6.26	15.00	5.00	1650.00	1641.70
25	6.66	15.00	5.00	1700.01	1687.74
26	7.09	15.00	5.00	1750.00	1733.90
27	8.02	15.00	5.00	1850.00	1826.40
28	8.53	15.00	5.00	1900.00	1872.53
29	8.36	25.00	5.00	1900.00	1869.85
30	8.25	35.00	5.00	1900.00	1867.05
31	9.94	-30.00	5.00	1900.05	1886.31

Table 21. Selected states for validation from the run FaV1_G8_B1.

	FaV1_G8_B_1				
	Power [kW]	Position [mm]	Pressure [mbar]	Up temp. [degC]	Bottom temp. [degC]
0	10.96	-20.00	849.30	1899.99	1880.36
1	10.86	-20.00	499.98	1900.01	1880.52
2	10.71	-20.00	250.01	1900.00	1880.43
3	10.54	-20.00	99.98	1900.00	1887.77
4	10.29	-20.00	50.00	1900.00	1887.57
5	10.03	-20.00	25.00	1900.00	1887.30
6	9.40	-20.00	4.11	1900.00	1887.28
7	9.42	-20.00	4.16	1900.00	1887.14
8	9.25	-20.00	0.55	1900.01	1887.23
9	9.26	-20.00	0.50	1900.00	1887.23
10	8.98	-20.00	0.04	1900.00	1887.89
11	8.96	-20.00	0.03	1900.00	1887.78
12	3.36	-20.00	5.00	1100.02	1128.56
13	3.76	-20.00	5.00	1200.06	1224.25
14	4.32	-20.00	5.00	1300.02	1319.20
15	4.64	-20.00	5.00	1349.99	1366.10
16	4.97	-20.00	4.99	1400.00	1413.28
17	5.31	-20.00	4.99	1450.01	1460.04
18	5.67	-20.00	4.99	1500.00	1507.39
19	6.05	-20.00	5.00	1549.99	1553.87
20	6.45	-20.00	4.99	1600.00	1600.55
21	6.86	-20.00	5.00	1650.00	1647.13
22	7.31	-20.00	4.99	1700.00	1693.56
23	8.27	-20.00	5.01	1799.99	1787.22
24	8.80	-20.00	5.00	1850.00	1833.77
25	9.35	-20.00	5.01	1900.01	1880.36
26	9.94	-20.00	4.99	1950.02	1927.43
27	10.56	-20.00	5.00	2000.00	1974.26
28	3.06	0.00	5.00	1100.00	1124.99
29	3.55	0.00	5.00	1199.98	1219.56
30	4.08	0.00	5.01	1300.00	1314.42
31	4.38	0.00	5.01	1349.99	1361.51
32	4.68	0.00	4.99	1400.00	1408.66
33	5.34	0.00	4.99	1499.99	1502.48
34	5.68	0.00	5.00	1549.99	1548.98
35	6.06	0.00	4.99	1600.00	1595.33
36	6.87	0.00	5.00	1700.01	1687.63
37	7.30	0.00	5.00	1750.00	1734.56
38	7.76	0.00	5.00	1799.99	1780.88
39	8.26	0.00	4.99	1849.99	1827.07
40	8.78	0.00	5.01	1900.01	1873.16
41	9.32	0.00	5.00	1950.01	1919.57
42	9.90	0.00	5.00	2000.00	1965.78

The states 28-42 from the run FaV1_G8_B_1 are used for the validation. A *Parametric Sweep* replicates the coil power, coil position and pressure conditions and using a 2D axisymmetric geometry identical as in *Figure 55*. The temperature profiles at the points measured by the pyrometers are evaluated and compared to experimental measurements as in *Figure 57*, together with the temperature difference between the pyrometers and the radiation model deviation from experimental data.
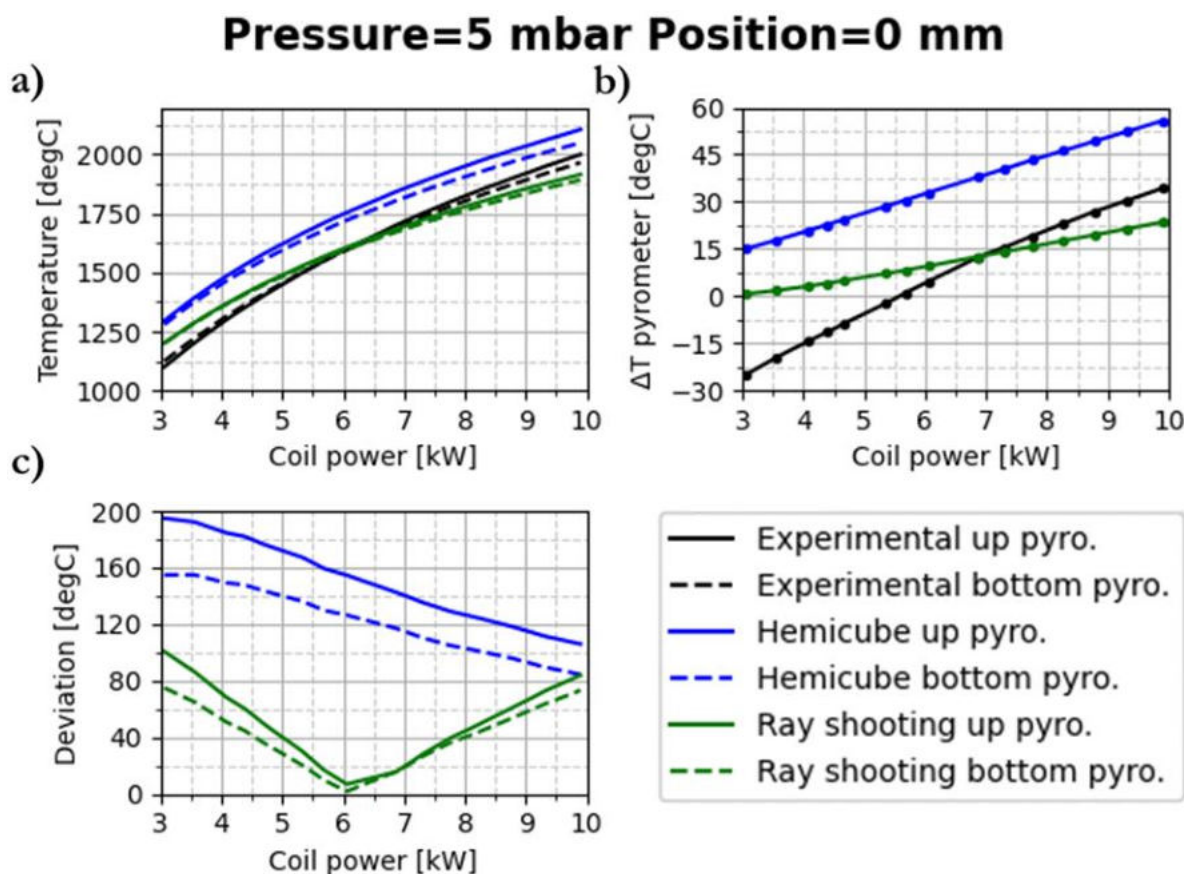
Figure 57. a) Temperature profile of both radiation models and experimental measurements. b) Temperature difference between pyrometers for radiation models and experimental measurements. c) Temperature deviation of both radiation models.

The whole profile and the temperature difference between the two pyrometers for different coil powers, ray shooting is always closer to the experimental values. For lower powers, the simulated result has higher values than the experimental data, while for higher power the simulation has lower values. On the other hand, hemicube has always noticeable much higher values than the experimental data. This can be better visualized by the deviation. Ray shooting gets closer to experiment for intermediate coil powers and differs more for both lower and higher power values.

Regarding hemicube, its deviation is significantly higher compared to ray shooting and it approaches the experiment results as the coil power increases.

States 0-11 from *Table 20* and *Table 21* demonstrate that as pressure reduces, less power is required to maintain the same temperature. This comes from the dependency of the insulator thermal conductivity on the pressure. In *Figure 58*, the experimental data of the states 4-9 from *Table 20* are used also for validation and check whether the pressure dependency is well considered in the radiation models.
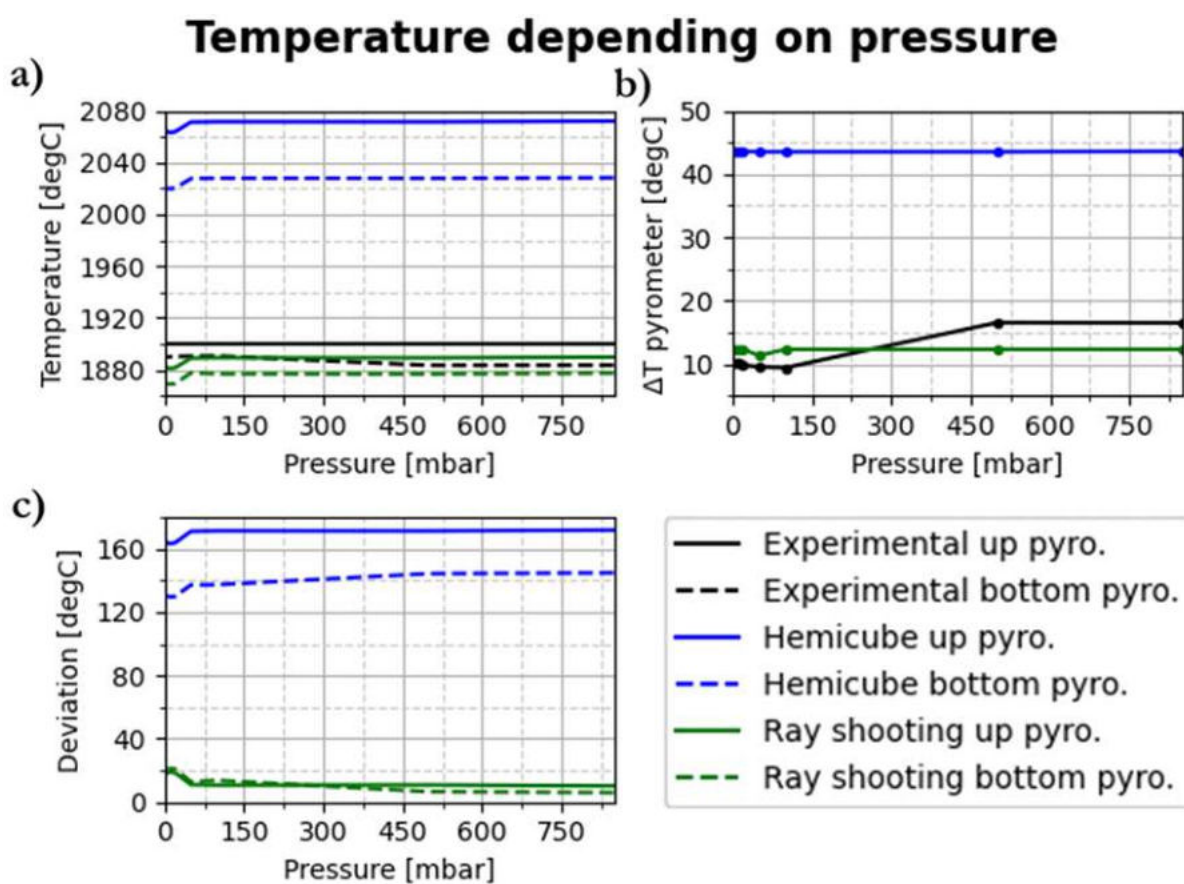
Figure 58. a) Temperature profile of both radiation models and experimental measurements depending on pressure. b) Temperature difference between pyrometers for radiation models and experimental measurements. c) Temperature deviation of both radiation models.

In this case, the difference between radiation models becomes more evident. Ray shooting is close to experimental values, having a deviation of around 10 °C. On the contrary, although hemicube follows the same tendency as ray shooting, its values are noticeably different from experimental data, having a deviation of 170 °C approximately.

To have a better quantitative idea of the similarity between experiment and simulation, the mean absolute value (MAE) is provided. This parameter is calculated according to *Eq. (21)*:

$$MAE = \frac{\sum_i^n |y_i - x_i|}{n}$$

(21)

whereby *n* is the number of measurements, y_i the simulation values and x_i the experimental value.

This is done for each pyrometer individually and also considering both pyrometers, the results are shown in *Table 22*. It is clearly demonstrated numerically that hemicube deviation is about one order of magnitude higher than ray shooting.

Table 22. MAE of radiation models to experimental measurements.

Temperature depending on coil power at constant pressure (*Figure 57*)	
	MAE [degC]
Hemicube: Up pyrometer	151.86
Hemicube: Bottom pyrometer	123.05
Ray shooting: Up pyrometer	51.35
Ray shooting: Bottom pyrometer	41.17
Hemicube: Both pyrometers	137.46
Ray shooting: Both pyrometers	46.26
Temperature depending on pressure (*Figure 58*)	
	MAE [degC]
Hemicube: Up pyrometer	168.03
Hemicube: Bottom pyrometer	136.21
Ray shooting: Up pyrometer	14.10
Ray shooting: Bottom pyrometer	14.54
Hemicube: Both pyrometers	152.12
Ray shooting: Both pyrometers	14.32

Nonetheless, some important unconsidered factors could certainly affect simulation results: inaccuracies in coil position, power measurement or pressure measurement, insufficient stabilization time when considering steady states or deficient material property considerations. All these aspects with the simplicity of the model might be the reasons why ray shooting still differs a bit from experimental data.

Overall, the difference between hemicube and ray shooting is very significant. Ray shooting has similar values to experimental data in both comparisons (*Figure 57* and *Figure 58*), having a deviation in the range of 14-51 ºC. Hemicube deviation is 123-168 ºC, an order of magnitude higher than ray shooting. This demonstrates hemicube is not able to resolve radiation and leads to higher temperature values for complex geometries, while ray shooting is more accurate and a better option specially for systems with complex geometries. Therefore, the ray shooting model is used for the next chapter

4.3 Coil properties effect

To have a complete control of the temperature profile, it is necessary to know how the coil position influences the induction heating process. As demonstrated previously (*Chapter 4.2*), ray shooting is more accurate, thus, this model will be used to check the effect of coil height, radius, and the filament/wire spacing. The simulations are done considering the presence of SiC powder and SiC seed. For each feature, a coil power of 12 kW is used and different values are checked such as temperature values at upper and lower pyrometer positions, temperature difference between powder and seed and temperature difference in the seed surface.

Firstly, coil height is investigated in different positions: -50, -40, -30, -20, -10, 0, 10, 20, 30, 40 and 50 mm. Up to now only 0 position was considered (*Figure 12*). The images below present the results for the following quantities: temperature at pyrometer positions (*Figure 59a*), temperature difference between hottest point in SiC powder and coldest point on SiC seed surface (*Figure 59b*) and temperature difference between hottest and coldest point on SiC seed surface (*Figure 59c*).
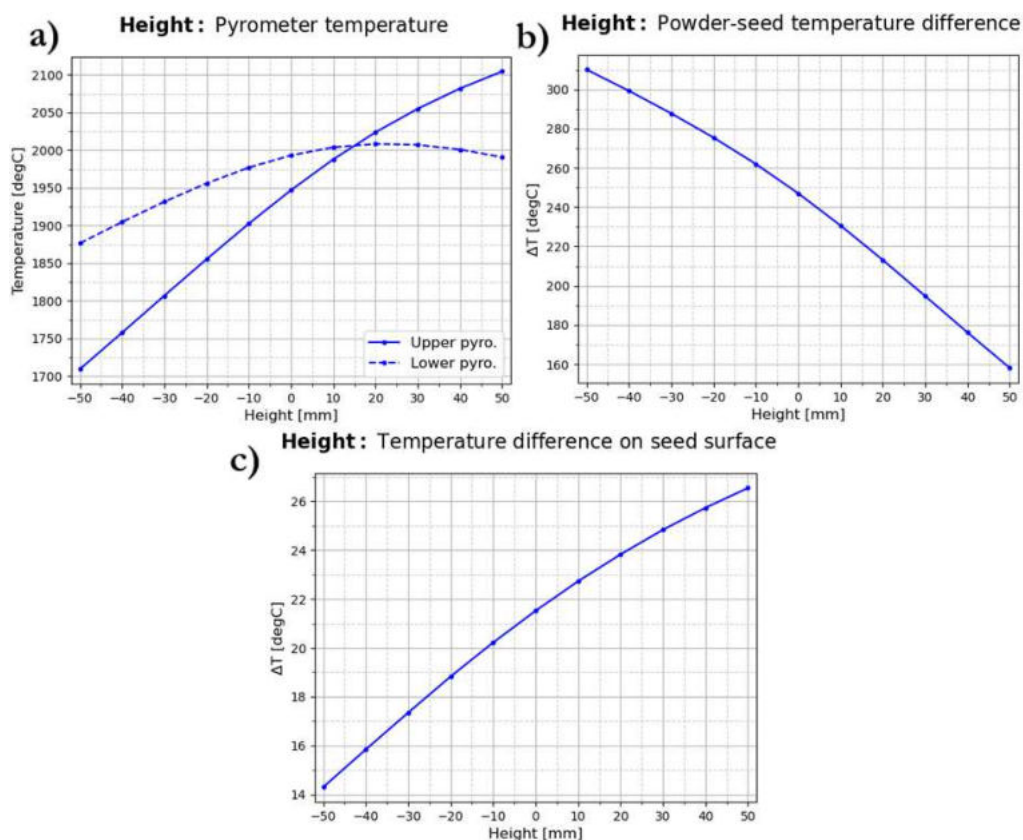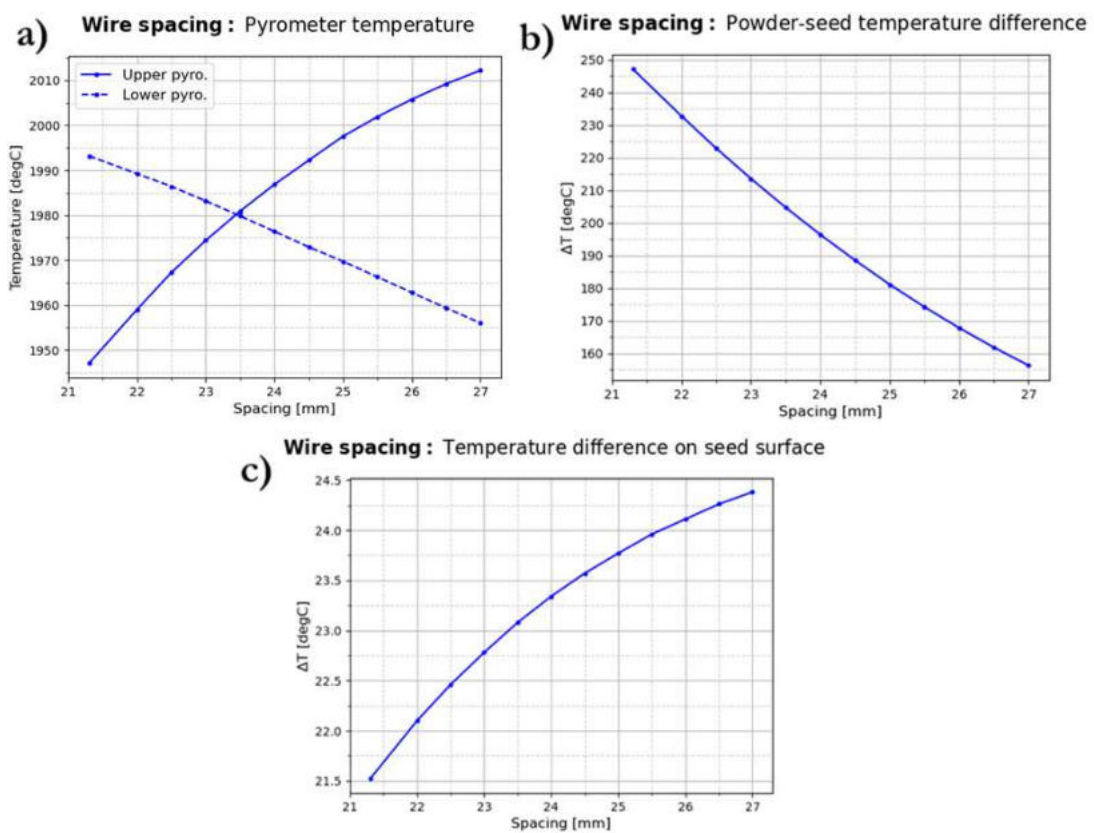

Figure 59. Temperature results depending on coil height. a) Temperature at pyrometer points. b) Temperature difference between SiC powder and SiC seed. c) Temperature difference at SiC seed surface.

All these measurements are strongly affected by the height position, although they have different behaviours. The temperature at pyrometer positions and temperature difference on the seed surface increases as the coil moves towards higher positions, but the temperature difference between powder and seed decreases. The main reason is the magnetic field strength, whose distribution is displayed in *Figure 60*. As the coil is in lower positions, the magnetic field is stronger at the lower parts of the crucible, being more efficient to generate eddy currents in those areas. Therefore, the lower part will be heated up more than the upper crucible part. In contrast, when the coil is moved to upper positions, the upper parts of the crucible are more heated by the eddy currents.

This explains the relation between the upper pyrometer temperature value and the height position. Nevertheless, the lower pyrometer temperature value seems to be not affected as strongly as the upper one and further height positions should be tested to investigate strong effects in both measurement positions. Regarding the temperature differences, the SiC powder occupies most of the growth part area and is barely affected by changes on the coil height. As mentioned, when the coil is at lower positions, eddy current generation is more efficient at lower positions (far from the seed) and the seed is much colder compared to the coil being at upper positions. For this reason, powder temperature is higher than seed temperature when coil is at the bottom, showing a decreasing powder-seed temperature difference as the coil moves upwards. In reference to the temperature difference on seed surface, it is caused by the radial distribution of the magnetic field strength. When the coil is at the bottom, the seed area is barely affected and the magnetic field strength is radially constant. Nonetheless, as the coil moves to the top, the radial distribution changes, inducing a strong magnetic field in the seed extreme and increasing the temperature in this zone. Consequently, the seed extreme (hot point) heats up to higher temperatures than the seed center (cold point) as the coil approaches its zone.
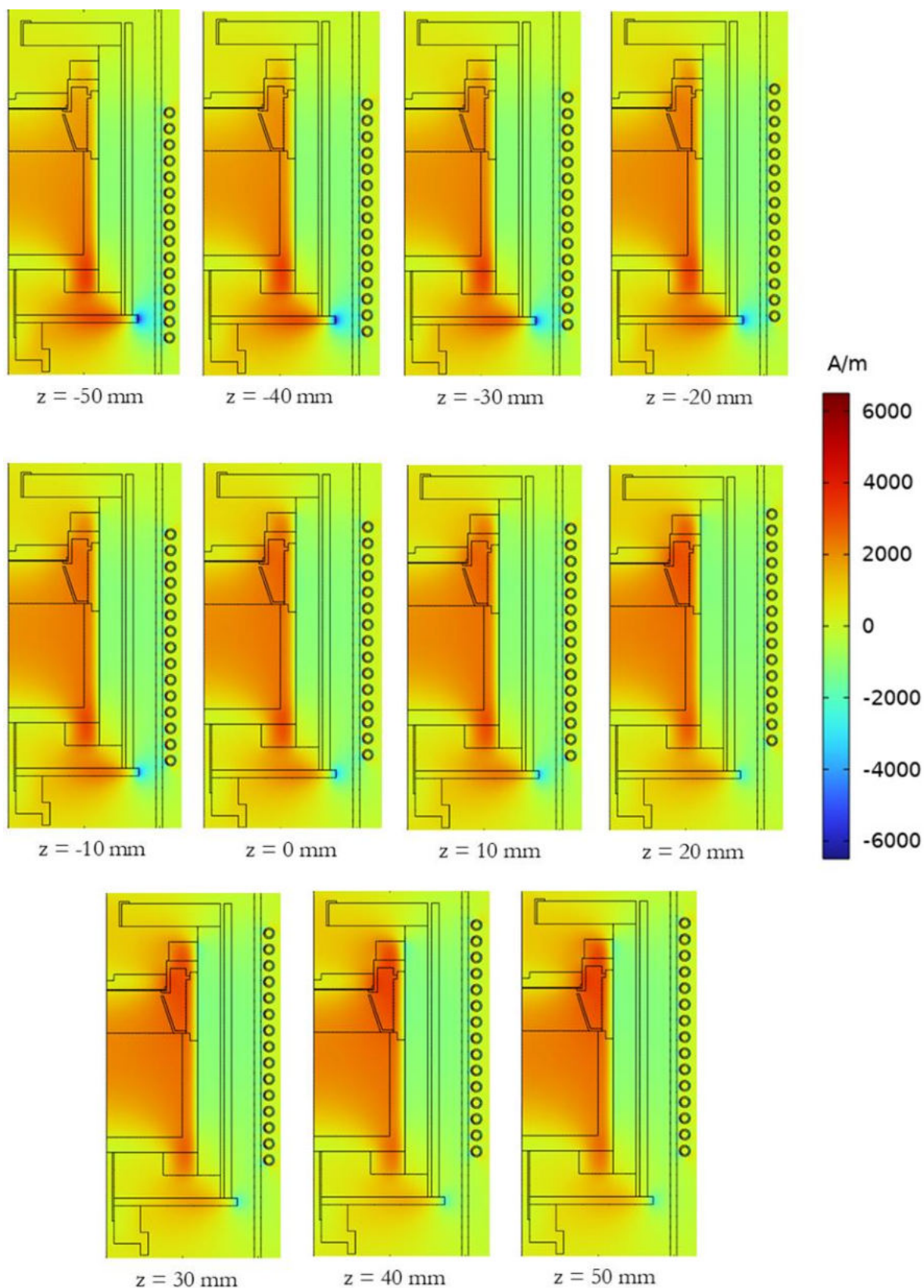
Figure 60. Magnetic field strength distribution for the different coil height values.

Hereafter, the effect of the coil radius on the temperature profile is investigated. The used values are: 214, 220, 230, 240, 250, 260, 270, 280, 290 and 300 mm. The results are displayed in the images below. In this case, all the measurements have the same tendency: all temperatures and temperature differences decrease when the radius increases.

The cause again lies in the distribution of the magnetic field. In this case, the magnetic field strength is decreasing uniformly as the coil radius increases, this is demonstrated in *Figure 62*. When the coil is close to the crucible, the induced magnetic field is strong and the generation of eddy currents is more efficient, having more localised hotter parts. This translates to higher temperatures and temperature differences. Conversely, as the coil moves away from the crucible, the magnetic strength reduces uniformly and the eddy current generation disperses. Owing to this spreading, the generated heat is more uniform within the crucible, reducing temperatures and temperature differences.
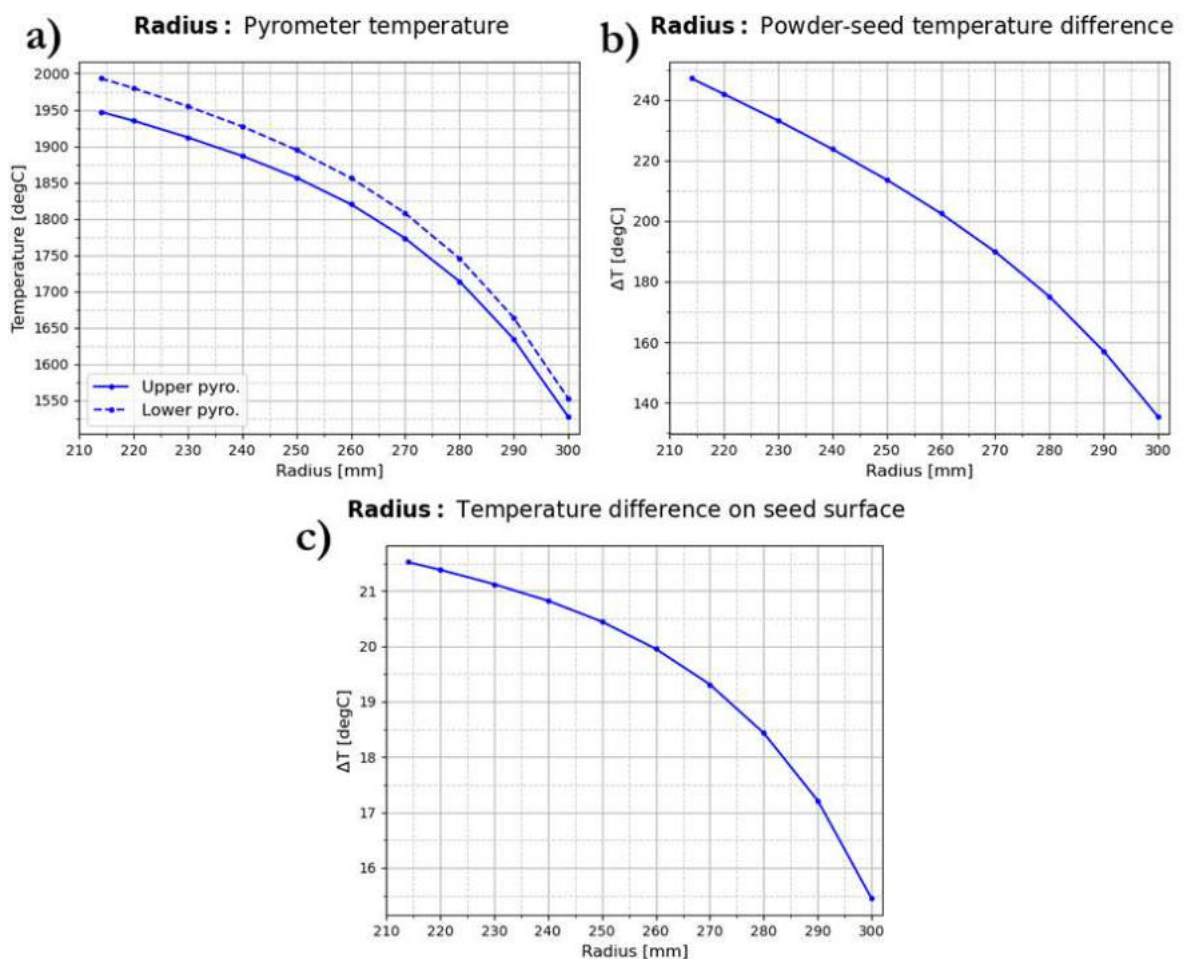
Figure 61. Temperature results depending on coil radius. a) Temperature at pyrometer points. b) Temperature difference between SiC powder and SiC seed. c) Temperature difference at SiC seed surface.
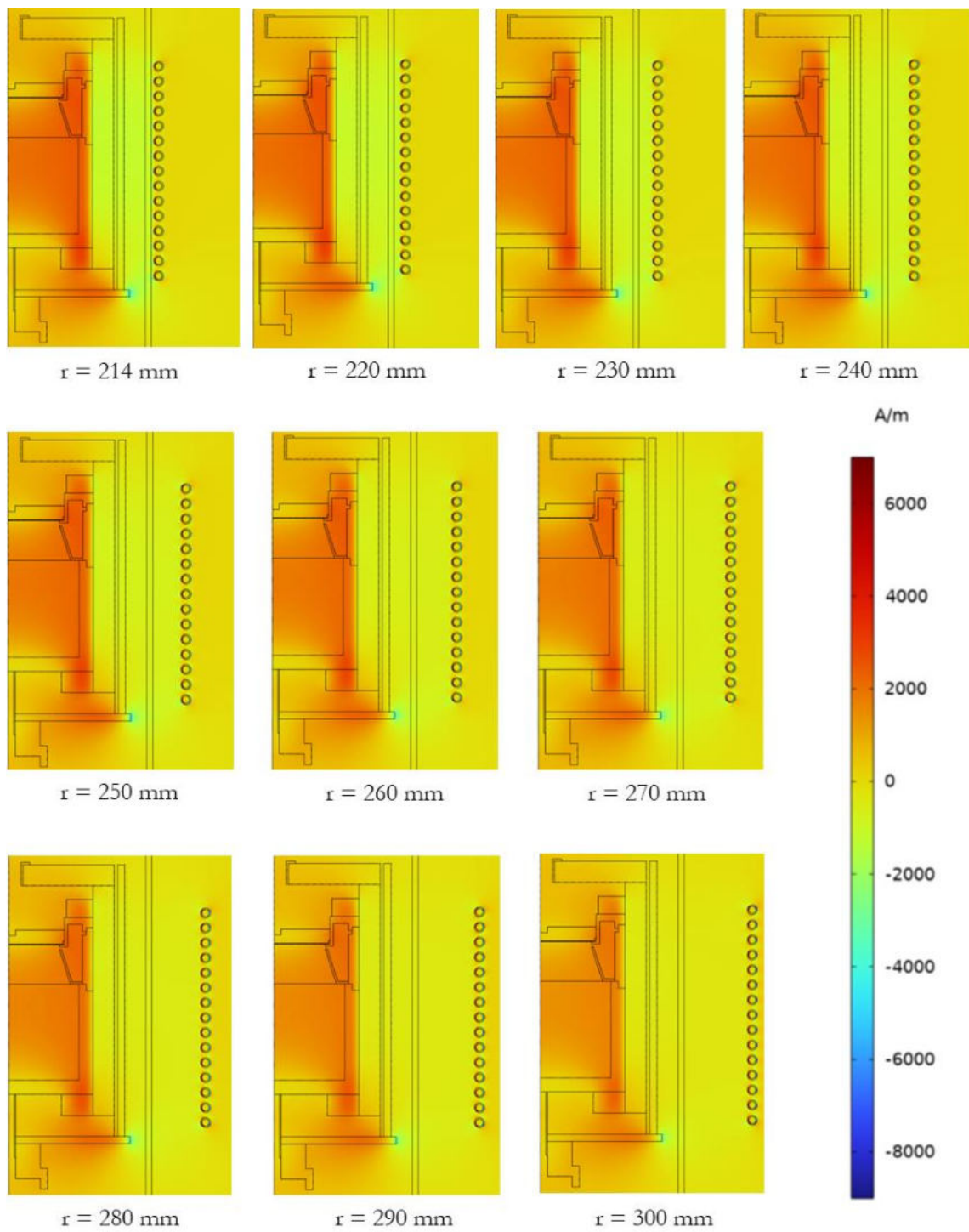
Figure 62. Magnetic field strength distribution for the different coil radius values.

Lastly, the wire spacing effect is inspected. The selected values are: 21.3, 22, 22.5, 23, 23.5, 24, 24.5, 25, 25.5, 26, 26.5 and 27 mm. As in the previous cases, the images below expose the different results. Their behaviour is comparable to the coil height modification, except for the temperature at the lower pyrometer point. As previously, it is originated by variations on the eddy current generation due to modifications in the induced magnetic field distribution.

Shown in *Figure 64*, when the wires are at the closest to each other, the magnetic field has a slightly stronger distribution at the crucible lower part. This causes the higher temperature at the lower pyrometer point and the highest powder-seed temperature difference. The seed is barely affected, therefore the powder is much hotter. Also, for this reason, the temperature difference at the seed surface is lower. Furthermore, when wires have the largest spacing, the strong localised point of the magnetic field is in the upper part of the crucible. This produces an increment of the upper pyrometer temperature and reduces the temperature of the lower pyrometer point. The seed is more affected in this condition, reaching the powder temperature and reducing their temperature difference. As the strongest magnetic field point is on top of the crucible, the seed is affected radially, which increases the temperature difference on its surface.

Figure 63. Temperature results depending on wire spacing. a) Temperature at pyrometer points. b) Temperature difference between SiC powder and SiC seed. c) Temperature difference at SiC seed surface.
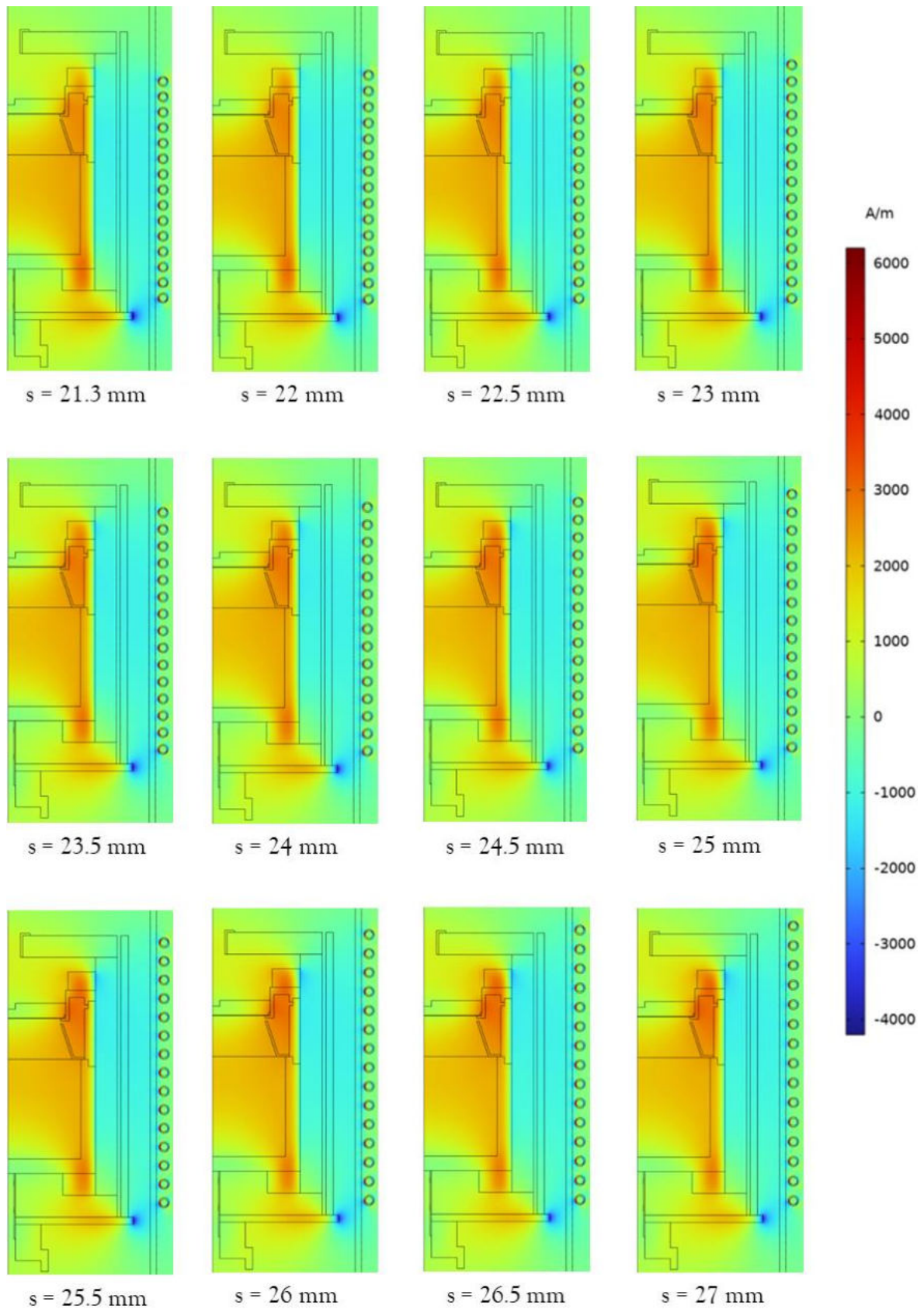
Figure 64. Magnetic field strength distribution for the different wire spacing values.

Thus, it is clear the coil positioning affects greatly the temperature profile and temperature gradients in the crucible. These might be one of the most important parameters when conducting PVT growth process, as temperature affects the process efficiency and the quality of the resulting SiC boule.

While height position and wire spacing have a similar effect, radius impact is completely different. The first parameters (height and wire spacing) affect the crucible axially and the remaining one (radius) affects it radially. Between height and wire spacing, the influence of the height is larger. Since the coil position varies drastically in the axial direction in relation to the crucible, it generates more localised spots with stronger induced magnetic fields. This asymmetric distribution allows to modify the temperature gradients decisively. This ability to strongly vary temperature gradients makes the height of the coil the most important factor for process optimization.

5 Summary

In this work, it is clarified that modelling is essential for the PVT growth process owing to the unavailability of checking the state of the procedure in real time. During the course of this study, several FEM simulations were conducted to verify the viability of setting up a first model, in which it is analysed which parameters are best to describe the temperature profiles during the growth process. No chemical reactions, mass transport, powder porosity or participating media are considered, only induction heating, heat conduction and surface-to-surface radiation. All the simulations were conducted using the FEM software COMSOL Multiphysics.

As shown in *Chapter 4.1*, the different radiation models are tested in different systems. The direct area integration model is directly discarded since it is an extremely simple model and just used for very specific conditions. Regarding the remaining radiation models, hemicube and ray shooting, are shown to provide same results for simple geometries. An important feature is the smoothness of the results using ray shooting, provided that the mesh is dense enough. Moreover, this model allows higher accuracy thanks to its additional convergence parameters. Nonetheless, as geometry becomes more complex and shadowing effects more important, the results between the models differ. As depicted in *Chapter 4.1.3*, this difference between models can be higher than 200 ºC.

Thus, a validation process was performed to assure which model is more accurate. To do so, experimental temperature profiles were compared to both models results. The experimental data were recorded by two pyrometers recording temperature values at the top and bottom of the crucible for different values of coil power, pressure and/or coil position. Demonstrated in *Chapter 4.2*, ray shooting gives much better results than hemicube, which leads to higher temperatures. This may be caused by an oversimplification of the radiating surfaces by the hemicube model, while ray shooting considers geometry complexities by means of ray tracing. Accordingly, ray shooting provides more accurate results at expenses of higher computational times.

Finally, in *Chapter 4.3*, the importance of the coil positioning to control the temperature profiles and gradients within the crucible is exposed. Parameters such as height, radius and wire spacing were checked. All of them have an impact on the temperature values due to variation of the induced magnetic field, but the parameter with the strongest effect is coil height.

Subsequently, it can be stated that the suitable model for describing radiation phenomenon is ray shooting. Additionally, a first idea of the coil positioning effect is provided and could help to optimise the temperature distribution within the crucible to achieve an efficient growth process and low defect density. Therefore, this simple model could be used as a basis for developing a more complex and realistic one with more features: participating media, graphitization, mass transport or powder porosity, among others.

6 References

[1]   R. Madar, "Materials science: silicon carbide in contention," *Nature*, vol. 430, no. 7003, pp. 974–975, 2004, doi: 10.1038/430974a.

[2]   J. Taillon, "Characterization of 4H-SiC MOSFETs," *Joshua Taillon*, 01 Aug., 2016. https://www.joshuataillon.com/project/silicon-carbide/ (accessed: Sep. 6 2023).

[3]   B. B. Zvyagin, "Polytypism of crystal structures," *Computers & Mathematics with Applications*, vol. 16, 5-8, pp. 569–591, 1988, doi: 10.1016/0898-1221(88)90247-7.

[4]   Savas Mitridis, *Physics of Advanced Materials Winter School 2008 Determination of lattice site location of impurities in compound semiconductors, by transmission electron microscopy*, 2011. [Online]. Available: https://www.researchgate.net/publication/274719826_Physics_of_Advanced_Materials_Winter_School_2008_Determination_of_lattice_site_location_of_impurities_in_compound_semiconductors_by_transmission_electron_microscopy

[5]   A. Elasser and T. P. Chow, "Silicon carbide benefits and advantages for power electronics circuits and systems," *Proceedings of the IEEE*, vol. 90, no. 6, pp. 969–986, 2002, doi: 10.1109/JPROC.2002.1021562.

[6]   P. J. Wellmann, "Review of SiC crystal growth technology," *Semicond. Sci. Technol.*, vol. 33, no. 10, p. 103001, 2018, doi: 10.1088/1361-6641/aad831.

[7]   P. J. Wellmann, "Power Electronic Semiconductor Materials for Automotive and Energy Saving Applications - SiC, GaN, Ga2O3, and Diamond," *Zeitschrift fur anorganische und allgemeine Chemie*, vol. 643, no. 21, pp. 1312–1322, 2017, doi: 10.1002/zaac.201700270.

[8]   N. Ohtani, T. Fujimoto, M. Katsuno, T. Aigo, and H. Yashiro, "Growth of large high-quality SiC single crystals," *Journal of Crystal Growth*, 237-239, pp. 1180–1186, 2002, doi: 10.1016/S0022-0248(01)02153-4.

[9]   F. C. Frank, "Capillary equilibria of dislocated crystals," *Acta Cryst*, vol. 4, no. 6, pp. 497–501, 1951, doi: 10.1107/S0365110X51001690.

[10]   D. L. Logan, *A First Course in the Finite Element Method CL Engineering- 6th ed.* [Online]. Available: https://www.academia.edu/90368744/_1_Logan_A_First_Course_in_the_Finite_Element_Method_CL_Engineering_6th_ed

[11]   *Detailed Explanation of the Finite Element Method (FEM)*. [Online]. Available: https://www.comsol.com/multiphysics/finite-element-method (accessed: Sep. 14 2023).

[12] T. L. Bergman, *Fundamentals of heat and mass transfer,* 7th ed. Hoboken: J. Wiley & Sons, op. 2011. [Online]. Available: https://books.google.at/books?id=vvyIoXEywMoC

[13] Y. A. Çengel, A. J. Ghajar, and M. Kanoglu, *Heat and mass transfer: Fundamentals and applications,* 4th ed. New York, México: McGraw-Hill, 2011.

[14] D. Ting, "Chapter 17 - Thermal radiation," in *Thermofluids: From Nature to Engineering*, D. Ting, Ed., San Diego: Elsevier Science & Technology, 2022, pp. 357–372. [Online]. Available: https://www.sciencedirect.com/science/article/pii/B9780323906265000124

[15] J. Meseguer, I. Pérez-Grande, and A. Sanz-Andrés, *Spacecraft thermal control.* Cambridge: Woodhead Pub, 2012. [Online]. Available: https://www.sciencedirect.com/science/book/9781845699963

[16] Ruba Amarin, *Hurricane wind speed and rain rate retrieval algorithm for the stepped frequency microwave radiometer.* [Online]. Available: https://www.researchgate.net/publication/47714393_HURRICANE_WIND_SPEED_AND_RAIN_RATE_RETRIEVAL_ALGORITHM_FOR_THE_STEPPED_FREQUENCY_MICROWAVE_RADIOMETER

[17] COMSOL, *Understanding Classical Gray Body Radiation Theory.* [Online]. Available: https://www.comsol.com/blogs/understanding-classical-gray-body-radiation-theory/ (accessed: Sep. 17 2023).

[18] *View factor calculation.* [Online]. Available: https://abaqus-docs.mit.edu/2017/English/SIMACAETHERefMap/simathe-c-viewfactor.htm (accessed: Sep. 17 2023).

[19] COMSOL, *Introduction to Computing Radiative Heat Exchange.* [Online]. Available: https://www.comsol.com/blogs/introduction-to-computing-radiative-heat-exchange/ (accessed: Sep. 25 2023).

[20] M. F. Cohen and J. R. Wallace, *Radiosity and realistic image synthesis,* 3rd ed. San Francisco, Calif.: Morgan Kaufmann, 2002.

[21] P. E. King-Smith, T. F. Mauger, C. G. Begley, and P. Tankam, "Optical Analysis and Reappraisal of the Peripheral Light Focusing Theory of Nasal Pterygia Formation," *Investigative ophthalmology & visual science*, vol. 61, no. 2, p. 42, 2020, doi: 10.1167/iovs.61.2.42.

[22] *Chapter 4 - Radiosity Principles.* [Online]. Available: https://tralvex.com/pub/rover/thesis/688374x.htm (accessed: Jan. 28 2024).

[23] T. Akenine-Möller, E. Haines, N. Hoffman, and D. C. Abbey, *Real-Time Rendering, Fourth Edition,* 4th ed. Milton: CRC Press LLC, 2018. [Online]. Available: https://ebookcentral.proquest.com/lib/kxp/detail.action?docID=5754532

[24] T. R. Steiner, "High temperature steady-state experiment for computational radiative heat transfer validation using COMSOL and ANSYS," *Results in Engineering,* vol. 13, p. 100354, 2022, doi: 10.1016/j.rineng.2022.100354.

[25] *Settings for the Surface-to-Surface Radiation Interface.* [Online]. Available: https://doc.comsol.com/6.0/doc/com.comsol.help.heat/heat_ug_interfaces.08.38.html (accessed: Oct. 6 2023).

[26] *2D Axisymmetric Structure Model Type.* [Online]. Available: https://support.ptc.com/help/creo/creo_pma/r9.0/usascii/index.html#page/simulate/simulate/int_struc2daxi_modl.html (accessed: Nov. 11 2023).

[27] "Zaher Ramadan. Private communication."

[28] *The Magnetic Fields Interface.* [Online]. Available: https://doc.comsol.com/5.5/doc/com.comsol.help.comsol/comsol_ref_acdc.17.67.html (accessed: Nov. 12 2023).

[29] *COMSOL Documentation.* [Online]. Available: http://localhost/docserver/#!/com.comsol.help.heat/heat_ug_interfaces.08.31.html?type=ext (accessed: Nov. 12 2023).

[30] *COMSOL Documentation.* [Online]. Available: http://localhost/docserver/#!/com.comsol.help.heat/heat_ug_interfaces.08.49.html?type=ext (accessed: Nov. 12 2023).

[31] P. Deuflhard, "A modified Newton method for the solution of ill-conditioned systems of nonlinear equations with application to multiple shooting," (in En;en), *Numer. Math.,* vol. 22, no. 4, pp. 289–315, 1974, doi: 10.1007/BF01406969.

[32] S. Hanzely, D. Kamzolov, D. Pasechnyuk, A. Gasnikov, P. Richtárik, and M. Takáč, "A Damped Newton Method Achieves Global O(1/k^2) and Local Quadratic Convergence Rate," Oct. 2022. [Online]. Available: https://arxiv.org/pdf/2211.00140.pdf

[33] *COMSOL Documentation.* [Online]. Available: http://localhost/docserver/#!/com.comsol.help.comsol/comsol_ref_solver.35.112.html%231029999 (accessed: Nov. 15 2023).

[34] *COMSOL Documentation.* [Online]. Available: http://localhost/docserver/#!/com.comsol.help.comsol/comsol_ref_solver.35.111.html%231072889 (accessed: Nov. 15 2023).

[35] *COMSOL Documentation.* [Online]. Available: http://localhost/docserver/ #!/com.comsol.help.comsol/comsol_ref_solver.35.171.html?type=ext (accessed: Nov. 15 2023).

[36] *COMSOL Documentation.* [Online]. Available: http://localhost/docserver/ #!/com.comsol.help.comsol/comsol_ref_solver.35.189.html?type=ext (accessed: Nov. 15 2023).

[37] J. Su, X. Chen, and Y. Li, "Numerical design of induction heating in the PVT growth of SiC crystal," *Journal of Crystal Growth*, vol. 401, pp. 128–132, 2014, doi: 10.1016/j.jcrysgro.2014.02.030.

Abbreviations

List of figures

List of tables